Nanomechanics and Nanoscale Adhesion in Biomaterials and Biocomposites: Elucidation of the Underlying Mechanism

by

Sina Youssefian

A Dissertation

Submitted to the Faculty

of the

WORCESTER POLYTECHNIC INSTITUTE

in partial fulfillment of the requirements for the

Degree of Doctor of Philosophy

in

Mechanical Engineering

by

_____

December 2015

APPROVED:

Dr. Nima Rahbar, Dissertation Advisor _____

Dr. Mark Richman, Dissertation Committee _____

Dr. Pratap Rao, Dissertation Committee _____

Dr. Leonard Albano, Dissertation Committee _____

Dr. Aaron Deskins, Dissertation Committee _____

Professor Jamal S. Yaoobi, Department Head _____

Abstract

Cellulose nanocrystals, one of the most abundant materials in nature, have attracted great attention in the biomedical community due to qualities such as supreme mechanical properties, biodegradability, biocompatibility and low density. In this research, we are interested in developing a bio-inspired material-by-design approach for cellulose-based composites with tailored interfaces and programmed microstructures that could provide an outstanding strength-to-weight ratio. After a preliminary study on some of the existing biomaterials, we have focused our research on studying the nanostructure and nanomechanics of the bamboo fiber, a cellulose-based biocomposite, designed by nature with remarkable strength-to-weight ratio (higher than steel and concrete). We have utilized atomistic simulations to investigate the mechanical properties and mechanisms of interactions between cellulose nanofibrils and the bamboo fiber matrix which is an intertwined hemicellulose and lignin called lignin-carbohydrate complex (LCC). Our results suggest that the molecular origin of the rigidity of bamboo fibers comes from the carbon-carbon or carbon-oxygen covalent bonds in the main chain of cellulose. In the matrix of bamboo fiber, hemicellulose exhibits larger elastic modulus and glass transition temperature than lignin whereas lignin shows greater tendency to adhere to cellulose nanofibrils. Consequently, the role of hemicellulose is found to enhance the thermodynamic properties and transverse rigidity of the matrix by forming dense hydrogen bond networks, and lignin is found to provide the strength of bamboo fibers by creating strong van der Waals forces between nanofibrils and the matrix. Our results show that the amorphous region of cellulose nanofibrils is the weakest interface in bamboo microfibrils. We also found out that water molecules enhance the mechanical

properties of lignin (up to 10%) by filling voids in the system and creating hydrogen bond bridges between polymer chains. For hemicellulose, however, the effect is always regressive due to the destructive effect of water molecules on the hydrogen bond in hemicellulose dense structure. Therefore, the porous structure of lignin supports the matrix to have higher rigidity in the presence of water molecules.

Acknowledgements

First and foremost, I would like to thank my advisor, Dr. Nima Rahbar who not only led me through my PhD to be a professional in my field but also allowed me to practice my leadership skills by leading other students, participating in conferences and joining student organizations.

I would also like to thank Dr. Jie Song for co-advising me on our project regarding orthopedic materials. I also benefitted from the aid of a number of graduate students: Sina Askarinejad and Gawain Thomas.

I would like to thank my friends who have been my inspiration in this path. Finally, I would like to thank my family who believed in me and encouraged me through my PhD, especially my father, Mohammad, mother, Shahrzad and sister Sepanta.

Contents

List of Figures

List of Tables

1 Introduction

Although using synthetic materials such as carbon nanotubes for biomedical applications provides an immediate solution for many patients, their long term outcomes are not satisfactory. Recently, cellulose nanocrystals (CNCs), one of the most abundant materials in nature, have attracted great attention in scientific community. This material not only has supreme mechanical properties that can surpass synthetic candidates such as functionalized graphene but also is biodegradable and biocompatible with low density. These qualities have rendered CNC as a unique material for many applications such as biomedical devices. With the increasing need and applications of the cellulose-based composite materials in biotechnology, a microscopic understanding of the mechanisms of molecular interactions and adhesion between layers of biomaterials has become of importance.

Adhesion, a ubiquitous phenomenon that presents in many devices such as micro electro mechanical system (MEMS) [1, 2] microelectronic devices [3 - 5] and biomedical devices [6], is the state in which two surfaces are held together by interfacial forces which may consist of valence forces or interlocking forces or both (ASTM, 1970). Strong adhesion between layers of biomaterials plays a significant role in providing high toughness and strength in the biomedical devices. Having high strength-to-weight ratio that would warranty the ability of the composite to withstand physiological loadings without exhibiting brittle fractures is an imperative key factor in designing medical devices such as drug delivery and synthetic orthopedic materials.

Most drug delivery devices are built from hard materials such as stainless steel because of its mechanical strength [7]. Since phenomena like corrosion result in the undesirable release of transition metal ions, devices need to be coated with an inert and biocompatible

material. The reliability and robustness of this device depend on the adhesion between the layers of the device because if they don't attach together, corrosion occurs and release of ions may lead not only to mechanical failure of implant but also to local pain and swelling in the near implant region. Moreover, the presence of metal ions in the organism causes the histopathological changes in detoxication organs (liver, kidney, spleen) and even induction of tumors [8].

Current clinically used synthetic orthopedic materials tend to consist of single bioinert metals, ceramics or polymers, or of a relatively coarse combination of these components. Researchers in this field are interested in the design of synthetic composite bone substitutes with well-defined structural integration of organic and inorganic components that recapitulate the integration of organic and inorganic building blocks of the natural extracellular matrix of bone. In these biomaterials, if the interaction between the matrix and filler is not sufficient, undesirable agglomeration of filler particles may lead to phase separation. Under mechanical loads, weak interfaces decreases strain at failure and could be the place where crack initiates. This could result in low T_g, strength and fracture toughness of the material.

In spite of the importance of interfacial interaction between materials in composites, well-established design methodologies to optimize engineering of composite polymers are not available. Here, we are interested in the biomimetic design of cellulose-based composite polymers for biomedical devices with outstanding strength-to-weight ratio. Therefore, in an effort to establish a material-by-design approach for biomaterials with tailored interfaces and programmed microstructures, we have investigated the structure of

the bamboo fiber, a biocomposite material designed by nature with remarkable strength-to-weight ratio.

1.1 Outline

In this research, in an effort to the biomimetic design of cellulose-based composite polymers for biomedical devices with outstanding strength-to-weight ratio, we investigated the mechanical properties and mechanisms of interactions between cellulose nanofibrils and the bamboo fiber matrix which is an intertwined hemicellulose and lignin called lignin-carbohydrate complex. With this aim, in chapter 2, different methods which are used in this research are presented. In chapter 3, we present a comprehensive review on bamboo structure and mechanical properties. In chapter 4, we have conducted a preliminary study on the adhesion energies between Drug Eluting Stent layers and orthopedic hydrogel-hydroxyapatite materials, using a combination of the AFM experiment, contact theory and atomistic simulation. In chapter 5, in an attempt to reveal the underlying mechanisms of molecular interactions in bamboo fibers, we have utilized atomistic simulations to investigate the mechanical properties and adhesion between the bamboo fiber constituents. In the chapter 6, we present the conclusion.

2 Theory

2.1 Molecular Dynamics Simulation

Molecular Dynamics simulation is a computer numerical technique, in which the classical Newtonian equations of motion are solved for a system of atoms given by,

$$\boldsymbol{f_i = m_i \ddot{r}_i} \quad \textbf{(1)}$$

For this purpose we need to be able to calculate the forces f_i acting on the atoms, and they are usually derived from a potential energy *U(r)* in Equation (2), where *r* is a displacement vector from the reference atom, *i*, with a mass m_i, to all the other surrounding atoms.

$$\boldsymbol{f_i = -\frac{\partial U}{\partial r_i}} \quad \textbf{(2)}$$

The key to the MD simulation is to define a realistic potential energy that can predict the materials behavior correctly. The potential energy comprises three parts, bonded, non-bonded and cross-term energies:

$$\boldsymbol{U(r) = U_{Bonded} + U_{Cross-Term} + U_{Non-Bonded}} \quad \textbf{(3)}$$

Bonded energies correspond to those when two or a group of atoms form bonds. This term mainly includes stretch, angle and dihedral angle (Torsion angle) energies as they appear in the Equation (4), respectively. Figure 1 shows three measures of spatial configuration in bonded energy.

$$\boldsymbol{U_{Bonded} = U_{Stretch} + U_{Angle} + U_{Torsion}} \quad \textbf{(4)}$$

The cross-term accounts for the energy changes induced by the change in the bond length and the angle changes in the surrounding atoms, as illustrated in the following equation:

$$\boldsymbol{U_{cross-term} = U_{bond-bond} + U_{angle-angle} + U_{bond-angle} + U_{endbond-torsion} + U_{middlebond-torsion} + U_{angle-torsion} + U_{angle-angle-torsion}} \quad \textbf{(5)}$$

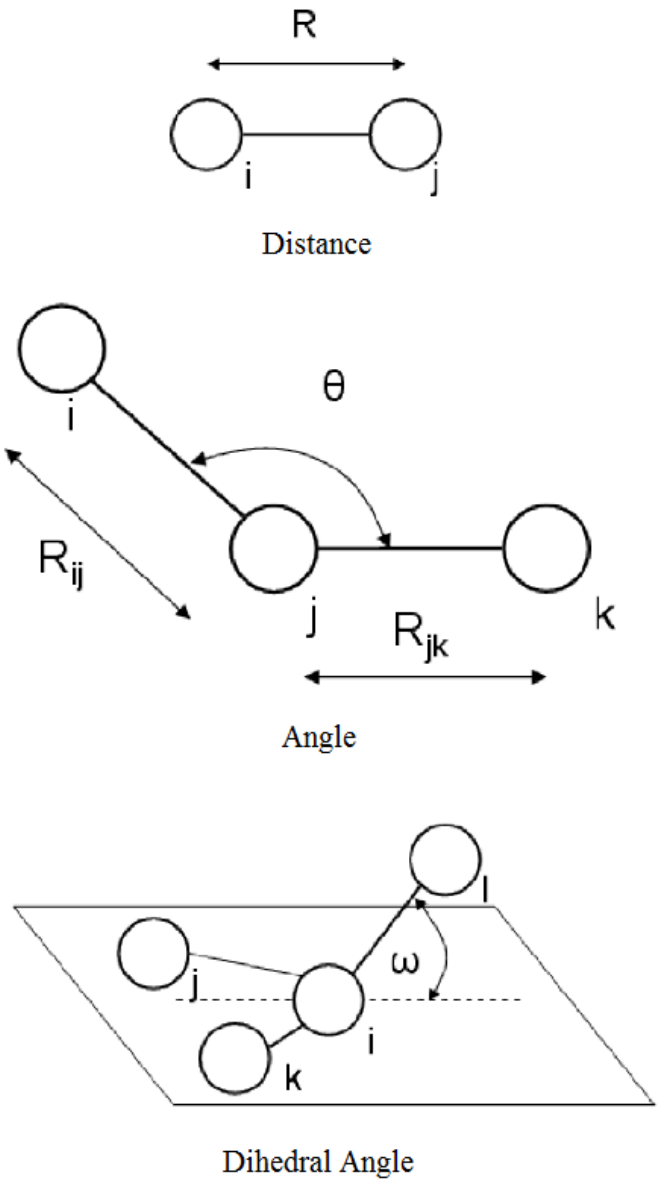

Figure 1. Three basic measures of spatial configuration of interacting particles used in functional forms to describe interactions. Distance is defined between two particles, angle between three and dihedral (torsion) angle between four.

The non-bonded energies mainly correspond to those interactions between atoms due to van der Waals (Figure 2), electrostatic and hydrogen bonds. Van der Waals energies are given by a Lennard-Jones potential shown in Equation (6) and electrostatic energies are

due to Columbic potential shown in Equation (7). Hydrogen bonds are natural consequences of these two potentials.

$$\boldsymbol{U_{LJ} = \sum_{i>j} \varepsilon[2(\frac{R_{min}}{r_{ij}})^{12} - 3(\frac{R_{min}}{r_{ij}})^{6}]} \quad (6)$$

$$\boldsymbol{U_{Col} = \sum_{i>j} \frac{C q_i q_j}{\epsilon r_{ij}}} \quad (7)$$

where ε is equilibrium well depth, R_{min} Equilibrium distance, C = 332.0647 (kcal/mol)Å, ϵ is Relative dielectric and q_i, q_j being charges on atoms i and j.

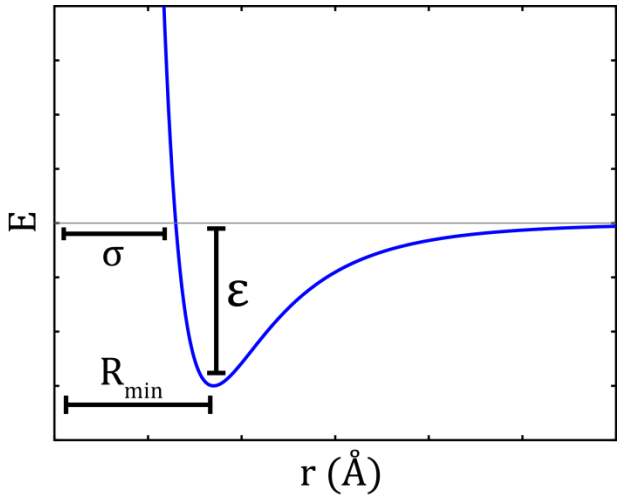

Figure 2. Lennard-Jones potential energy. This energy includes repulsive and attraction part presented by positive and negative terms of correlation, respectively.

In this project condensed-phased optimized molecular potential COMPASS (cff91 ver. 2.6 [9]) was chosen as a proper force field for defining the potential energy in atomistic simulations. This force field is one of the first ab-initio based force field that can capture the structural, thermal and mechanical properties of different types of materials such as carbohydrates [10-13]. In COMPASS, the non-bonded energies include van der Waals and electrostatic energies, with hydrogen bonds being a natural consequence of electrostatic energies. It is well parameterized for non-bonded interactions, which makes it a good fit for long-chain molecules like biomaterials or polymers and other systems

where the van der Waals interaction is the governing interaction. The COMPASS force field uses the following expressions for various components of the potential energy:

$$\boldsymbol{U_{Stretch}} = \sum_b \boldsymbol{K_2}(\boldsymbol{b}-\boldsymbol{b_0})^2 + \boldsymbol{K_3}(\boldsymbol{b}-\boldsymbol{b_0})^3 + \boldsymbol{K_4}(\boldsymbol{b}-\boldsymbol{b_0})^4 \quad (8)$$

$$\boldsymbol{U_{Angle}} = \sum_b \boldsymbol{H_2}\,(\boldsymbol{\theta}-\boldsymbol{\theta_0})^2 + \boldsymbol{H_3}(\boldsymbol{\theta}-\boldsymbol{\theta_0})^3 + \boldsymbol{H_4}(\boldsymbol{\theta}-\boldsymbol{\theta_0})^4 \quad (9)$$

$$\boldsymbol{U_{Torsion}} = \sum_{\varphi}\{\boldsymbol{V_1}\,[\boldsymbol{1}-\boldsymbol{cos}(\boldsymbol{\varphi}-\boldsymbol{\varphi_1})] + \boldsymbol{V_2}\,[\boldsymbol{1}-\boldsymbol{cos}(\boldsymbol{\varphi}-\boldsymbol{\varphi_2})] + \boldsymbol{V_3}\,[\boldsymbol{1}-\boldsymbol{co\,s}(\boldsymbol{\varphi}-\boldsymbol{\varphi_3})]\} \quad (10)$$

$$\boldsymbol{U_{out-plane}} = \sum_i \boldsymbol{K_i}\boldsymbol{\chi}^2 \quad (11)$$

$$\boldsymbol{U_{bond-bond}} = \sum_b \sum_{b'} \boldsymbol{F_{bb'}}(\boldsymbol{b}-\boldsymbol{b_0})(\boldsymbol{b'}-\boldsymbol{b'_0}) \quad (12)$$

$$\boldsymbol{U_{angle-angle}} = \sum_{\theta} \sum_{\theta'} \boldsymbol{F_{\theta\theta'}}\,(\boldsymbol{\theta}-\boldsymbol{\theta_0})(\boldsymbol{\theta'}-\boldsymbol{\theta'_0}) \quad (13)$$

$$\boldsymbol{U_{bond-angle}} = \sum_b \sum_{\theta} \boldsymbol{F_{b\theta}}\,(\boldsymbol{b}-\boldsymbol{b_0})(\boldsymbol{\theta}\,-\boldsymbol{\theta_0}) \quad (14)$$

$$\boldsymbol{U_{endbond-torsion}} = \sum_b \sum_{\varphi} \boldsymbol{F_{b\varphi}}(\boldsymbol{b}-\boldsymbol{b_0})[\boldsymbol{V_1 cos}(\boldsymbol{\varphi}) + \boldsymbol{V_2 cos}(\boldsymbol{2\varphi}) + \boldsymbol{V_3 cos}(\boldsymbol{3\varphi})] \quad (15)$$

$$\boldsymbol{U_{middlebond-torsion}} = \sum_{b'} \sum_{\varphi} \boldsymbol{F_{b'\varphi}}(\boldsymbol{b}-\boldsymbol{\varphi_0})[\boldsymbol{F_1}\,\boldsymbol{\cos}(\boldsymbol{\varphi}) + \boldsymbol{F_2}\,\boldsymbol{\cos}(\boldsymbol{2\varphi}) + \boldsymbol{F_3}\boldsymbol{\cos}(\boldsymbol{3\varphi})] \quad (16)$$

$$\boldsymbol{U_{angle-torsion}} = \sum_{\theta} \sum_{\varphi} \boldsymbol{F_{\theta\varphi}}(\boldsymbol{\theta}-\boldsymbol{\theta_0})[\boldsymbol{V_1 cos}(\boldsymbol{\varphi}) + \boldsymbol{V_2 cos}(\boldsymbol{2\varphi}) + \boldsymbol{V_3 cos}(\boldsymbol{3\varphi})] \quad (17)$$

$$\boldsymbol{U_{anle-angle-torsion}} = \sum_{\varphi} \sum_{\theta} \sum_{\theta'} \boldsymbol{K_{\varphi\theta\theta'}}\,\boldsymbol{cos\varphi}(\boldsymbol{\theta}-\boldsymbol{\theta_0})(\boldsymbol{\theta'}-\boldsymbol{\theta'_0}) \quad (18)$$

where b, θ, ϕ, and χ are the bond length, bond angle, dihedral torsion angle, and the inversion or out-of-plane angle, respectively; q is the atomic charge, ε is the dielectric constant; $r_{ij} = r_j - r_i$ is the vector between i and j; b_0, K_i (I = 2 to 4), θ_0, H_i (i= 2 – 4), ϕ_i (i=1 – 3), V_i (i=1 – 3), and $F_{bb'}$, b_0 , $F_{\theta\theta'}$, θ_0 , $F_{b\theta}$, $\boldsymbol{F_{b\varphi}}$, $\boldsymbol{F_{b'\varphi}}$, $\boldsymbol{F_{\theta\varphi}}$ and $\boldsymbol{K_{\varphi\theta\theta'}}$ are the system-dependent parameters implemented in the COMPASS force field. The single-point change (SPC) model is implemented in COMPASS for modeling the water molecules.

The molecular dynamics simulation begins with modeling the molecular structure of each material. The models are optimized using a Smart algorithm, which is a cascade of the steepest descent, adjusted basis set Newton-Raphson (ABNR), and quasi-Newton method. To make sure that the system is in a stable condition and to release the artificial energy due to artificial cubic structure, a sequence of MD simulations is performed to relax the protein structure. The relaxation process initially starts with Canonical ensemble (NVT) simulation for 50 ps for 5 x 10^4 steps at 298 K, followed by 130 ps Isothermal–isobaric ensemble (NPT) simulation at 310 K and 1 atm. The system cools down to 298 K at the same pressure in NPT simulation for 50 ps to reach the stability in which the density fluctuations near a preset value are negligible. The outcomes of molecular dynamics simulation are positions, velocities and forces between atoms. Using these results, energies, structures, mechanical and thermodynamic properties of the materials can be studied.

2.1.1 Hydrogen bond energy

Studies on hydrogen bonds were conducted on the final structures with the following criteria:

1 The maximum distance between the hydrogen and the acceptor atom for which hydrogen bonding is possible is 2.5 Å.

2 The minimum angle between the donor, hydrogen and acceptor atoms in degrees for which hydrogen bonding is possible was chosen as 120°.

For calculating the hydrogen bond energy, we have used a CHARMM-like hydrogen bonding potential such as Equation (19),

$$\boldsymbol{E_{hb} = D_{hb}[5(\frac{R_{hb}}{R_{DA}})^{12} - 6\left(\frac{R_{hb}}{R_{DA}}\right)^{10}]cos^4(\theta_{DHA})} \quad (19)$$

where θ_{DHA} is the bond angle between hydrogen donor (D) and the hydrogen (H) and the hydrogen acceptor (A). R_{DA} is the distance between the donor and acceptor. The values of D_{hb} and R_{hb} were adopted from the literature

2.1.2 Structure

To study the nanostructures of these models, a Radial Distribution Function (RDF) was used. RDF is a structural characterization parameter of amorphous molecules that provides the basic information about short range order and the nature of atomic interactions. RDF gives the possibility of finding a particle at a certain distance from the reference particle. The observed variations in dihedral conformation and internal structural variables are the results of the dynamics of non-bonded interactions like hydrogen bonding, electrostatic and van der Waal interactions. Hansen and McDonald define the resulting function, g(r), as [14]:

$$\boldsymbol{g(r) = \frac{1}{\rho}\frac{1}{N}\sum_{j=1}^{N_\alpha}\sum_{i=1}^{N_\beta}\delta(r - r_i + r_j)} \quad \textbf{(20)}$$

where N is the total number of atoms, ρ is the overall number density Nα and Nβ are the number of atoms of type α and β, respectively.

2.1.3 Mechanical Properties

In order to get the mechanical properties, the periodic structure is expanded along each direction to the maximum strain amplitude of 0.01 in 10 steps. In each step the stresses were obtained from virial stress expression, Equation (21), which is commonly used to relate the computed stress in molecular dynamics to continuum stresses.

$$\boldsymbol{\sigma = -\frac{1}{V_0}\left[\left(\sum_{i=1}^{N} m_i\left(v_i v_i^T\right)\right) + \left(\sum_{i<j} r_{ij} f_{ij}^T\right)\right]} \quad \textbf{(21)}$$

where index i runs over all particles 1 through N. m_i, v_i and f_i denote the mass, velocity and force acting on particle i, and V_0 denotes the (undeformed) system volume.

2.1.4 Glass transition temperature

The glass transition temperature can be obtained from the change in the slope of specific volume-temperature curve [15, 16]. To achieve this aim, the temperature of each system s increased to 700K and slowly bright down to 100K at the rate of 0.5 K/ps while the temperature and pressure are controlled by the Nose thermostat and Berendsen barostat, respectively. In 48 random steps, the system is equilibrated with NPT dynamics for 25 ps and the results are recorded to create the specific volume-temperature curves. These curves are used to compute the glass transition temperatures of hemicellulose, LCC and lignin.

2.1.5 Adhesion

To investigate the interaction energies at the interfaces between material A and B, a layer of A is placed on B. The B layer is fixed in all directions whereas the A layer is free to move during the simulations. The size of the moving layers determines the simulation time span, given by the time required for the atoms to travel towards the substrate and to reach the steady state. The size of the moving layers determines the simulation time span, given by the time required for the atoms to travel towards the substrate and to reach the steady state. Hence, the simulation time is regulated by diffusion properties of moving layers and can be consequently calculated by using the Strokes-Einstein equation. This equation estimates the diffusion constant of a small particle with a radius of 5 nm to be in the order of 10^{-10} m^2 /s. Since the average traveling distance of moving layer is about 0.5 nm, simulation time is estimated to be about 1.2 ns ($t \sim \frac{x^2}{2D}$). In this time period, the NVT dynamic simulations at 300K with 1 fs time step are performed for three different conformations of these materials to minimize the effect of initial conformation on the final results. The magnitude of the adhesion energy between two bodies can be

determined from the energies needed to overcome the intermolecular forces between two surfaces and to create two new surfaces. Surface energy is a parameter that quantifies this breaking energy of intermolecular forces that occur when a surface is created.

Therefore, to quantify the adhesion energy, thermodynamic quantity, work of adhesion, is defined from surface energies of the system. The work of adhesion between two different materials A and B is the work needed to be done on a unit area of AB to form a unit area of two surface of A and B reversibly. This parameter in equilibrium in vacuum can be defined as [17, 18]:

$$\Delta\boldsymbol{\gamma} = \boldsymbol{\gamma_A} + \boldsymbol{\gamma_B} - \boldsymbol{\gamma_{AB}} \quad \textbf{(22)}$$

where $\Delta\gamma$ is the work of adhesion, $\boldsymbol{\gamma}_{\mathrm{A}}$ and $\boldsymbol{\gamma}_{\mathrm{B}}$ are surface energies of the two separate phases in equilibrium in vacuum, and $\boldsymbol{\gamma}_{\mathrm{AB}}$ is the interface energy of the two phases in contact in equilibrium.

2.2 Atomic Force Microscopic Experiments

In the AFM experiments, the tips are coated with the desired material and brought into contact with the desired coupon. Figure 3 presents a schematic of a typical force-displacement curve associated with the AFM adhesion experiments in which contact mode of AFM test is used to bring AFM tip to contact with the coupon (Extending curve) and pulled off (Retracting curve). In this process, the pull-off forces can be obtained from maximum deflection of the tip during the retracting time. It is possible to convert these adhesion forces into interfacial adhesion energies, using contact mechanics that consider the radii and deformation characteristics of the mating surfaces [6, 19].

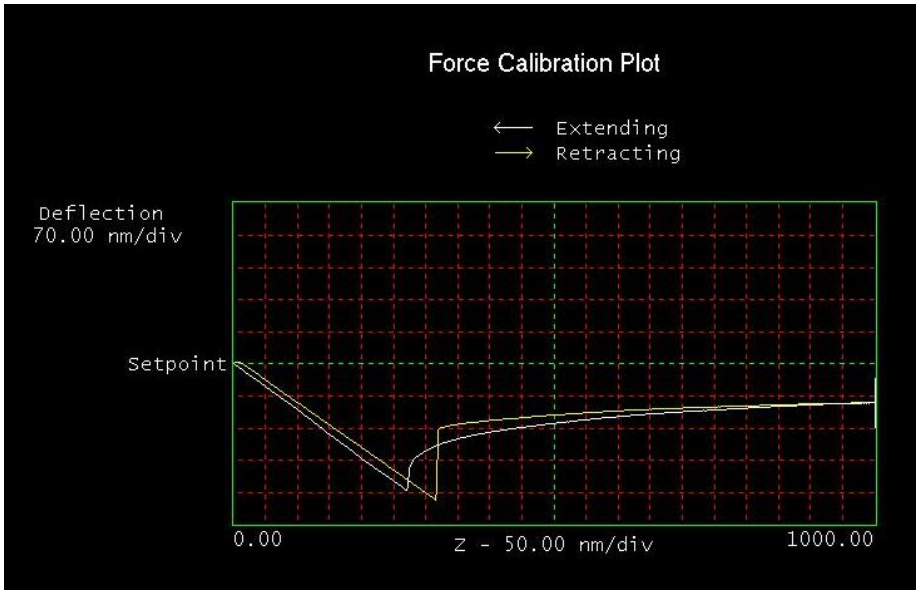

Figure 3. Typical force-displacement curve obtained from interaction between polymer and minerals. The maximum deflection of the tip is on retracting curve.

Since the source of adhesion is primarily due to intermolecular forces between two surfaces, most of the mechanical adhesion tests provide a largely overestimated work of adhesion. The measured work of adhesion is usually orders of magnitude higher than real work of adhesion because the mechanical properties of materials get involve in measurement and effect on the accurate estimation of the thermodynamic quantity. Several possible contact theories are available for calculating the adhesion energies from interaction forces obtained from AFM experiment. These theories are discussed in the following section.

2.3 Contact Mechanics Theories

One of the pioneers in the contact mechanics theory was Hertz who had considered geometry effects on local elastic deformation properties in 1880 with the Hertzian Theory [20]. In this theory the elastic deformation of bodies incorporated in the surface deformation and the surface interactions, such as van der Waals interactions or contact

adhesive interactions are neglected (A comprehensive study on the elastic contact of two bodies is presented in the Appendix).

Johnson, Kendall and Roberts (JKR) improved the Hertzian theory by adding the adhesive forces to the contact area [21]. The adhesion force (F_{JKR}) between two rigid spheres can be expressed as Equation (23).

$$\boldsymbol{F_{JKR} = -\frac{3}{2}\pi R^{*}\Delta\gamma} \quad \textbf{(23)}$$

where, R^{*} is the combined reduced radius of the two spheres in contact with the radius of R_1 and R_2, which is calculated as $R^{*}=R_1R_2 / (R_1+R_2)$.

JKR theory cannot accurately predict the contact between stiff materials because it is only applicable for contact between compliant materials and accounts only for short range surface forces. Derjaugin, Mullet and Toporov (DMT) theory is a more involved theory in which the van der Waals interactions outside the elastic contact are considered [22]. DMT theory calculates the work of adhesion for stiff materials in contact and accounts only for long range surface interactions by,

$$\boldsymbol{F_{DMT} = -2\pi R^{*}\Delta\gamma} \quad \textbf{(24)}$$

These two supposedly contrary theories were recognized as the limiting cases of the contact problems by Tabor [23]. He pointed out that both models are correct as they are just two extreme cases. He showed these two cases by introducing the Tabor's parameter, μ, as follows [24]:

$$\boldsymbol{\mu = \left(\frac{16R\,\Delta\gamma^{2}}{9K^{2}z_0^{3}}\right)^{1/3}} \quad \textbf{(25)}$$

where, z_0 is the equilibrium separation of the surfaces and K is the reduced modulus of elasticity of the tip and sample given by $K = \frac{4}{3}\left(\frac{1-\nu_1^{2}}{E_1} + \frac{1-\nu_2^{2}}{E_2}\right)^{-1}$.

For μ << 1 DMT theory is applied and for μ >> 1 JKR theory is valid. To approximate an actual interaction potential which is the intermediate situation between JKR and MDT (Figure 4), Maugis considers a Dugdale potential to describe attractive forces between contacting spheres as MD theory [25-27].

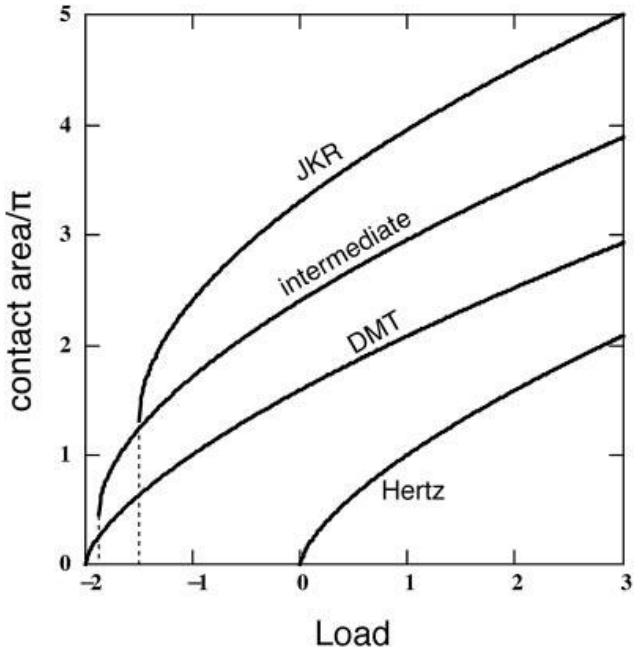

Figure 4. Plot of contact area vs. load for Hertz, JKR, DMT and MD intermediate Theory. The minus values show pull-off forces due to adhesion energies which are considers in all models except Hertz [68].

In the MD theory the transition parameter, λ is defined from Tabor's parameter such that λ=1.1570 μ. The adhesion forces, then, defined from Equation (27).

$$\boldsymbol{F_{MD} = -\bar{F}\pi R^{*}\Delta\gamma} \qquad \textbf{(26)}$$

where, $\bar{F}$ is defined from λ. For λ < 0.1, $\bar{F}$ is 2 as the DMT model is valid and for λ > 5, $\bar{F}$ is $\frac{3}{2}$ as the JKR model is valid (Figure 5). More details on MD theory are presented in chapter 4.

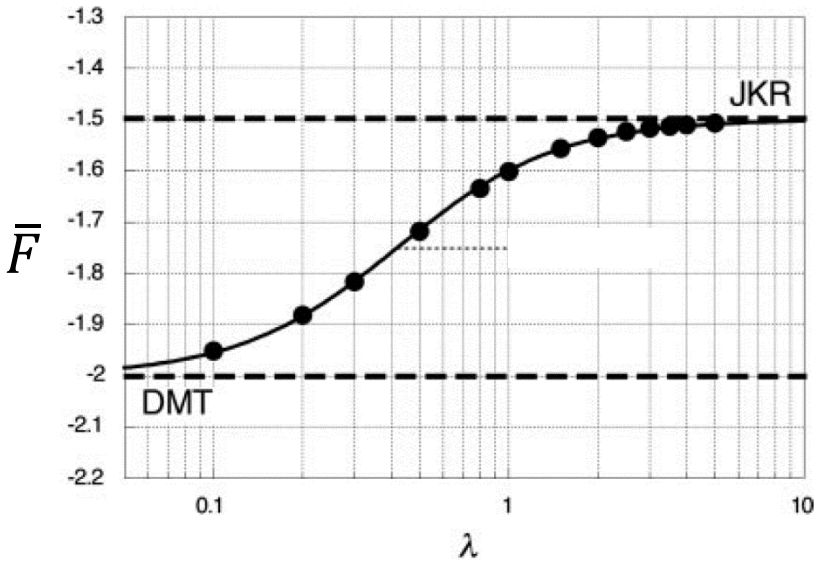

Figure 5. Diagram of $\overline{F}$ vs. λ determined from the MD solution. Small λ indicates DMT model is valid and large λ shows JKR model is valid [24].

All these theories enable us to calculate the work of adhesion between two surfaces, knowing the pull-off forces which can be obtained from the experiments. Among of all the tests with which the work of adhesion can be measured [28], AFM experiment enables us to calculate the pull-off forces in nanoscale.

3 Literature Review

3.1 Bamboo: Functionally Graded Hieratical Material

Bamboo is the common term for large grass family that include 1250 species within 75 types, most of which are relatively fast-growing, attaining stand maturity within five years. Dwarf bamboos may be as little as 10 cm in height, but tall species may reach 15 to 20 m, and the largest known grows up to 40 m in height and 30 cm in culm diameter [29, 30]. Some of the bamboo species are considered to be effective structural materials for many construction applications such as structural members in low-rise houses, short span foot bridges, long span roofs and construction platforms in countries with plentiful bamboo resources such as China.

The structure of Bamboo is a typical example of plants with highly developed architectures. It has a hierarchical structure that makes a typical natural functionally graded bio-composite [31]. In this structure, there are no tree rings in the culm's cross-section. Instead, Bamboo comprises three fundamental tissues named epidermis, parenchyma tissue and vascular bundles [32].

The epidermis is the outermost layers of bamboo which protects the internal components from invaders. The attractive green color of bamboo culm is due to the chlorophyll of epidermis. Smooth surface of the bamboo, also, exists because of silica (SiO2), a wax layer, and other substances of epidermis. The silica also facilitates CO_2 uptake of plants and strengthens the outer epidermis for prevention of external attacks [33, 34].

Parenchyma tissue is the non-wood structure of bamboo. The ground parenchyma tissues of crop species such as rice and maize have only one type. Bamboo, however, has two types of parenchyma cells named short and long parenchyma cells that have differences in lignification and the hemicellulose distribution. These differences reflect the

differences in function of the two types of parenchyma cells [35]. Parenchyma ground tissue forms a matrix in which vascular bundles are placed.

The vascular bundles mainly consisting of xylem, phloem and fiber caps which is playing a decisive role in bamboo physiological growth and biomechanical function. The vascular bundle inhomogeneous distribution is dense in the outer region and sparse in the inner region [36]. This special dissemination is a perfect structural adaptation towards a high bending stiffness and strength of the bamboo culm. The conducting elements (vessels and phloem) provide a channel for the transport of water and nutrients. The fibers, which are accounting for approximately 40 percent of a culm by volume, primarily carry out the function of mechanical support.

The fibers around the phloem do not have the same thickness. The immature fibers close to the vessels and the phloem complete their wall thickening first, whereas those at the periphery of the fiber caps are in a transition state. Therefore, a distinct density gradient can be observed from the fibers adjacent to the vessels towards the fibers connected to the surrounding parenchymatic tissue [37]. The six different fiber wall types could be distinguished in the bundle fibers close to phloem that all have mainly hemicellulose-lignin matrix surrounding the cellulose microfibrils, in their secondary walls. The degree of lignification varies remarkably across the fiber wall, with a higher lignin content present in the narrow layers [38, 39].

The development of fiber and parenchyma that occur during internode elongation in the temperate bamboo has three stages. The first stage involves cell divisions in both cell types. During the second stage, as the elongation of the internode proceeds, parenchyma

cells continue to divide whereas fibers begin to elongate. Finally, in the third stage, both cell types elongate [40].

3.2 Multiscale Structure and Mechanical Properties of Bamboo

Bamboo resembles a long cylinder, reinforced by strong fibers, with a hollow core that reduces its weight. The geometry of bamboo's longitudinal profile has a macroscopically functionally graded structure whose compositions and mechanical properties vary continuously from the outer to the inner. The fiber density of sclerenchyma tissues within the bamboo is a good indicator of the strength capacity of bamboo. Three-point flexural test shows that the elastic modulus in the outer surface region of bamboo culm is higher than that in the inner region, which shows the graded distribution of the mechanical properties of bamboo [41]. Amada et al. outline the structure and mechanical properties of bamboo [42]. The bamboo used in the experimental investigation is a two-year old 'Mouso' bamboo (Phyllostachys edulis Riv.) 16 ~ 20m in height and a maximum diameter of 12 ~ 13cm. Applying a mixture principle to bamboo, the tensile strength and other properties of the fiber and the matrix are obtained. The strength in the inner region is about 80GPa and increases parabolically with radial distance, reaching its maximum value in the outer region. The Tensile strength of the matrix and fiber found to be 50 MPa and 610 MPa respectively, While the Young's modulus for them found to be 2 GPa and 46 GPa [42]. The tensile tests were also performed on bamboo nodes without any additional machining of their surfaces. They obtained 29.4± 4.5 MPa for the strength and 2.22 ± 0.3GPa for the Young's modulus, which were almost the same at the different positions. Finally, it is noted in this paper that bamboo has a smart material with a hierarchical structure. Nogata and Takahashi performed tension tests within 48 h after

Moso bamboo species was taken from the field, to prevent any change in the mechanical properties due to moisture loss [43]. The specimens were taken from nine areas arranged from the inner layer to the outer layer. Since the extreme inside specimen was made of pure ground tissue, its strength was correspondingly about 25 MPa. Thus, the strength of pure fiber was estimated to be about 810MPa which is equivalent to that of steel (600-1000 MPa). Furthermore, Young's modulus of pure fiber was 55 GPa. This value is about one quarter of the value of steel, which is 200 GPa [43]. Dixon and Gibson investigated the properties of natural Moso bamboo to further enable the processing and design of sustainable structural bamboo products. They found that the sclerenchyma fibers dominate axial elasticity [44]. On the nano- and microscales, nanoindentation techniques were used by Tan et al. to study the local variations in the Young's moduli of moso culm bamboo cross-sections. These are then incorporated into finite element models in which the actual variations in Young's moduli are used to model the deformation and fracture of bamboo during fracture toughness experiments [45]. Bamboo slices were first obtained along the longitudinal direction. Then they were separated with equal space in the cross-section. Finally, dog bone shaped specimens used for tensile experiment were machined from these bamboo slices. The nanoindentation results for Young's moduli distributions along the radial direction of the bamboo cross-sections shows that the outer layer with a modulus of elasticity of 13.5 GPa is more rigid than the inner layer with 7 GPa. The outer layer has a tensile strength of 700 MPa whereas the inner layer's strength is around 200 MPa. It is shown in this research that In the case of crack growth in the outside and inside crack orientations cellulose bridging fibers are associated with the toughening mechanism. Lower cellulose bridging fiber density was observed within the interlaminar

cracks in the outside crack orientation. In contrast, the higher cellulose bridge densities in the inside crack orientation were associated with strong resistance curve behavior [46].

The fiber bridging was also observed by Habibi et al [46]. They used multi-scale mechanical characterizations assisted with advanced environmental scanning electron microscopy (ESEM) to investigate the asymmetric flexural responses of natural bamboo strips under different loading configurations, during elastic bending and fracture failure stages, with their respective deformation mechanisms at microstructural level. They found fibers' bridging and crack deflection are also partly responsible for the gradient and remarkable flexural strength and toughness of bamboo strips. Hence, as the overall volume fraction of fiber decreased (thickness of the strips approached the entire thickness of bamboo culm), the contribution of triggered toughening mechanisms, due to the presence of fibers, also diminished which resulted in minimizing the flexural strength and toughness of bamboo strips. They performed the flexural tests in mode A and B. In the mode A the load was exerted on the higher fiber density side and the mode B on the lower fiber density side of bending configurations. For Mode A fracture, the crack bridging, due to the fibers' bridging, alongside its resultant fibers' debonding is the most significant toughening mechanism. Accordingly, the layers with very large volume fraction of fibers result in very low extent of crack bridging and fibers' debonding in Mode B, because delamination occurred more often. This considerably reduces the flexural strength.

Keogh et al. performed fatigue tests on bamboo culm [47]. Bamboo culm samples display fatigue failure when loaded in compression across their diameters, simulating a type of deformation which commonly occurs as a result of culm bending. However, they

observed no fatigue behavior when samples are loaded in axial compression. Failure in the first cycle (i.e. static failure) is associated with a tensile stress of 10.4 MPa on the outer surface and 19.1 MPa on the inner surface. High cycle failure at 100,000 cycles requires a stress range of 4.5 MPa on the outer surface and 11 MPa on the inner surface.

The fracture toughness of bamboo culms was studied by Amada et al [48]. A specimen with a notch with a thickness of 0.4mm was used for tensile tests to evaluate fracture toughness. The average value obtained was 56.8 MPa.m1/2. This value is higher than Al-Alloys.

The fracture property of bamboo as a natural composite material depends on where the crack initiates. For bamboo, the crack either starts from the matrix region or fiber region. In order to elucidate this behavior in bamboo, Amada et al used Equation (27). In this condition is satisfied, the material is characterized as first matrix-cracking type.

$$\boldsymbol{\sigma_m} < \left(\frac{\boldsymbol{E_m}}{\boldsymbol{E_f}}\right)\boldsymbol{\sigma_f} \qquad \textbf{(27)}$$

where, σ_m and σ_f are the strength of matrix and fiber, and E_mand E_f are their Young's modulus, respectively. For bamboo σ_m=50, MPa σ_f=610 MPa, E_f=46 GPa and E_m=2 GPa. Using these numbers in the Equation (43), the fracture characteristic of bamboo must be first fiber-cracking [27]. This kind of material often has fiber pull-out features on its fracture surface.

Using multi-scale mechanical characterizations coupled with advanced environmental electron microscopy (ESEM), Habibi et al. unambiguously showed that fibers' interfacial areas along with parenchyma cells' boundaries were preferred routes for crack growth in both radial and longitudinal directions [47]. The occurrence of interfacial fractures within the cellular parenchyma matrix along with honeycomb structure of fibers in both radial

and longitudinal directions is mainly responsible for the remarkable fracture toughness of bamboo by reducing the overall effective stress intensity factor.

By performing micro and nanomechanical characterizations on bamboo's individual constituents, they confirmed that fibers are indeed the strongest phase whereas parenchyma cells are comparatively weaker [48]. In this research elastic modulus of fibers found to be Ef = 22.8 ± 2.8 GPa by Nanoindentation and Ef = 30.1 ± 3.0 GPa by micro-tensile testing and the tensile strength of fibers found to be $\sigma f = 1000 \pm 300$ MPa. Elastic modulus of parenchyma ground obtained to be Ep = 3.7 ± 0.4 GPa by nanoindentation [48].

3.3 Mechanical Properties of Bamboo Fibers

Fibers are a fundamental structural component of the bamboo culm as they provide mechanical support. To gain better understanding of the principles of mechanical optimization in bamboo fibers, a single-fiber tensile test at four different span lengths for fibers of the bamboo species was performed by Osorio et al [49]. Table 1 summarizes the obtained mechanical properties for different gage lengths. The average strength values of 800 MPa and Young's modulus of 43 GPa were obtained.

Table 1. Tensile mechanical properties for untreated bamboo fibers after mechine compliance at different span lengths

Gage Length	Strength (MPa)	Young's Modulus (GPa)	Strain to Failure (%)	Average Fiber Diameter (μm)
5	860±119	46±1.2	1.9±0.3	152±29.5
10	811±136.5	43±0.9	1.9±0.3	156±35.9
25	778±121.9	43±1.4	1.8±0.2	141±22.2
40	775±103.3	42±1.1	1.7±0.2	147±30.8

Rao et al. showed that the quality of bamboo fibers which are extracted mechanically is excellent compared to bamboo fibers that are extracted chemically [50]. They found that

the mechanically extracted fibers (Bamboo (M)) have less percentage of tensile strain, higher tensile strength and higher tensile modulus compare to chemically extracted fibers (Bamboo (C)) (Table 2).

Table 2. Tensile properties of various natural fibers

Name of the Fiber	Tensile Strain (%)	Average Strength (MPa)	Average Modulus (GPa)	Specific Tensile Strength (MPa/kgm^{-3})
Vakka	3.46	549	15.85	0.6778
Date	2.73	309	11.32	0.3121
Bamboo (M)	1.40	459	35.91	0.5527
Bamboo (C)	1.73	503	19.67	0.3831
Coconut	20.00	500	2.5	0.4348
Banana	5.45	600	17.85	0.4444

The strength and elastic modulus of bamboo fibers was reported to be around 610 MPa and 46 GPa, respectively [41, 47]. Nogata and Takahashi compared the strength and elastic modulus of bamboo fibers with different steel alloys, aluminum alloys and ceramics. They showed that the bamboo fiber has a specific elastic modulus and strength of 52.3 (GPa.m3/kg) and 770 (MPa.m3/kg) which are much higher than that of steel (25.6 (GPa.m3/kg) and 102-154 (MPa.m3/kg)), Al alloys (26 (GPa.m3/kg) and 140-550 (MPa.m3/kg)) and Ceramics (81-100 (GPa.m3/kg) and 43-128 (MPa.m3/kg)), respectively [42].

Microstructures of bamboo fibers were determined by using scanning electron microscope [51]. The results showed the single fibers were longitudinally aligned in the flat-wise direction. They were together bonded by hemicelluloses and lignin with different bonding levels. Mechanical properties of fiber bundle and their interfacial shear strength (IFSS) with typical resins such as unsaturated polyester and polypropylene are related to lignin and hemicelluloses content in chemical composition. The experimental

results also proved that the IFSS of alkaline treated fibers were better than that of steam-exploded and untreated fibers. Moisture absorptions of bamboo fibers at 50, 60, 70, 80 and 90% relative humidity at 200^{C} was also determined. The results showed that the difference of moisture content of the alkaline-treated and the steam-exploded fibers was much lower than that of the untreated fibers at all relative humidity levels.

3.4 Chemical Composition of Bamboo Fibers

The chemical composition of bamboo fiber constitutes mainly cellulose, hemicelluloses and lignin. These components are actually same high-glycans, and make about 90% of total weight of bamboo fiber. The other constituents are protein, fat, pectin, tannins, pigments and ash. These constituents play important role in physiological activity of bamboo and they are found in cell cavity or special organelles [52]. The lignin is considered to provide stiffness and yellow color to bamboo fibers. Different treatments cannot remove all the lignin content of the bamboo fibers, as lignin has been found quite resistant to various alkalis. Non cellulosic components have enough contribution to fiber properties such as strength, flexibility, moisture, and even density [53]. The unidirectional arrangement of bamboo fibers in tissues and cell wall structure of bamboo is one of unique property of bamboo.

Bamboo fiber is different from the other cellulose fibers in morphology, crystalline structure and molecular structure. In SEM images, the cross section of the bamboo fiber is round with a small lumen and there is no node in the longitudinal surface [54]. Most of the bamboo fibers have multilamellate cell walls with various layers. By means of viscometry, Yueping et al showed that the bamboo fiber has a small molecular mass and degree of polymerization [54]. Wegst et al reported that bamboo cellulose microfibrils

imbedded in a lignin–hemicellulose matrix shaped into hollow prismatic cells of varying wall thickness [55].

The percentage of cellulose in bamboo fiber is about 73%, while about 10% lignin and about 12% hemicellulose still remain in the fiber [54]. All lingo-cellulosic based natural fibers consist of cellulose microfibrils in an amorphous matrix of lignin and hemicellulose. These fibers consist of several fibrils which run along the length of the fiber. Each fibril exhibits a complex layered structure made up of thin primary wall encircling a thicker secondary layer. In the secondary layer, parallel cellulose microfibrils are wound helically around the fibrils. The angle between the fiber axis and the microfibrils is termed the microfibril angle. Natural fibers themselves are cellulose fiber-reinforced materials and the microfibril angle and cellulose content determine the mechanical behavior of the fiber [56]. The bamboo fiber has a larger moisture regain capability than cotton, ramie and flax fibers because of its loose structure and existence of disordered non-cellulose substances [57].

3.5 Lignin in Cell Wall

The existence of lignin is the main reason for fiber stiffness among the mechanical properties [57]. Confocal Raman microscopy with a spatial resolution of less than 1 μm was used by Wang et al. to study the local distribution of lignin and cellulose in the present cell types and the different regions across the fiber cap [58]. They found that the fiber cell walls were found to show almost axially oriented cellulose fibrils, and the stiffness and hardness of the central part of the cell wall remained basically consistent for the fibers at different regions across the fiber cap. The almost axially oriented cellulose fibrils in the fiber walls maximize the longitudinal elastic modulus of the fibers and their

lignification increases the transverse rigidity. Unlike hardwood and softwood trees, bamboos develop only a primary shoot without secondary thickening growth which impedes geometrical adaptations and increases the necessity of structural optimization at the material level. The secondary wall of the fibers showed the highest level of lignification, followed by the parenchyma cells and the metaxylem vessel. Low lignin content in vessel walls was also reported for the bamboo P. viridiglaucescens based on a UV microspectrophotometry study [59]. This is contrary to the situation found in most deciduous trees in which the vessel walls are highly lignified to rigidify the wall [60], which is a necessity to cope with the large radial tensile forces resulting from the water transpiration stream. Raman spectra revealed that cellulose fibrils of the secondary walls of fibers were oriented basically in fiber direction.

By means of nanoindentation tests, Wang et al. showed that the degree of lignification seems to have a minor influence on the cell wall stiffness of bamboo fibers, which can be explained by the almost longitudinal orientation of the cellulose fibrils [58]. This is contradictory with the previous researches that shown the indentation modulus and hardness are highly dependent on both cellulose microfibril angle and lignin level of plant cell walls [61, 62].

The fiber cell walls of moso bamboo have almost axially oriented cellulose fibrils (between 2° to 13° [63 - 65]) which impede a regulation of axial tensile stiffness by the degree of lignification. Therefore, in the examined bamboo culm, a stiffness gradient across the fiber cap is mainly developed by differential cell wall thickening, which affects tissue density and thereby axial tissue stiffness of the different regions of the cap [66].

The lignin distribution within the cell walls of Gigantochloa levis was studied topochemically by means of TEM and cellular UV microspectrophotometry. The distribution of lignin structural units in different anatomical regions is described and lignification of the tropical bamboo species Gigantochloa levis is compared with that of the temperate bamboo species Phyllostachys viridiglaucescens [67]. The secondary layer fiber wall in general has a lamellar structure with increasing lignin content from the center towards the compound middle lamella. The vessel walls have lower lignin content. The mechanical properties of cellulose, lignin and hemicellulose were measured by previous researchers and a summary is presented in Table 3 [67].

Table 3. Tensile properties of various natural fibers

Material	Density (g/cc)	Young's modulus (GPa)	Tensile Strength (MPa)
Cellulose	1.45-1.59	120-167	750 - 1080
Lignin	1.2-1.25	2.5 – 3.7	25 – 75
Hemicellulose	1.55	5 - 8	N/A

3.6 NanoStructure of Bamboo Fiber

The bulk properties of materials are dictated not only by their elemental composition and molecular connectivity, but also by their macromolecular architecture. A principal example of this is observed in plant cell walls, which are composite materials consisting of biopolymers designed to serve multiple functions including structural support, microbial defense, and transport of water and nutrients throughout the organism.

Ciesielski et al. introduced computational methodology to extract nanoscale geometry of cellulose microfibrils within thermochemically treated biomass directly from electron tomographic data sets. Computational analysis of the tomographic data is used to extract

mathematical descriptions for longitudinal axes of cellulose microfibrils from which we calculate their nanoscale curvature [68]. They have extracted mathematical representations for the nanoscale geometry of cellulose microfibrils in pretreated biomass from tomographic data sets. The resulting parametric equations were used to calculate the curvature of plant cellulose microfibrils for the first time. They also found that orienting microfibril models to bend about the 100 crystal plane reduced the formation of kink defects after energy minimization [68].

The structure of the cellulose microfibrils of spruce wood was investigated by Fernandes et al., using a range of spectroscopic methods coupled to small-angle neutron and wide-angle X-ray scattering [69]. Disorder in chain packing and hydrogen bonding was shown to increase outwards from the microfibril center. The extent of disorder blurred the distinction between the Iα and Iβ allomorphs. Chains at the surface were distinct in conformation, with high levels of conformational disorder at C-6, less intramolecular hydrogen bonding and more outward-directed hydrogen bonding.

Fernandes et al. suggest that cellulose microfibrils with about 24 chains, possibly twisted and with considerable disorder increasing towards the surfaces. Less extensive disordered regions probably exist within the core of each microfibril. Tight lateral binding is facilitated by the hydrogen-bonding pattern of the surface chains, at only a small cost in tensile stiffness due to the loss of intramolecular hydrogen bonding between O2 and O6. The surface location of these disordered chains means that a parallel mechanical model with tight lateral bonding to the ordered core is more appropriate than a series model, consistent with FTIR observations. The twisting of adjacent cellulose microfibrils may explain why they do not come into crystallographic register with one another over

enough of their length to merge [69]. A rectangular model is favored for spruce microfibrils, differing from more crystalline celluloses in having one hydrophobic and one hydrophilic face exposed. It is not clear how other polymers restrict access of celluloses to the hydrophobic surfaces, but impacts of the structure and aggregation of microfibrils on the recalcitrance of woody biomass are to be expected.

Kulasinski et al. investigate the influence of adsorbed water on amorphous cellulose structure and properties, within the full range of moisture content from the dry state to saturation, by molecular dynamics simulation [70]. They found out that the properties of amorphous cellulose undergo a significant change about 10% of moisture content.

4 Preliminary Study on Biomedical Devices

4.1 Drug Eluting Stent

Drug-eluting stents (DESs) is a device on which anti-proliferative drugs that reduce smooth muscle cell growth and migration are placed, to release in the body gradually. This treatment is one of the effective methods for preventing restenosis after stenting operations [71, 72]. Stainless steel 316L has been used in DESs implant material because of its mechanical strength and the capability to bend and shape to create a custom fit in the operating room as well as low cost in comparison with other metallic implant materials [73,74]. However, 316L corrosion occurs in contact with biological environments and causes the release of metal ions, such as chromium, iron and nickel [75]. Therefore, DES is coated with a chemically inert and highly biocompatible polymer such as Poly (o-chloro-p-xylylene) (parylene C) [76-78]. O-chloro-p-xylylene is a benzene ring with two methylene groups on both ends and one chlorine side group. 316L is coated with parylene C through a vapor deposition process in which the substrate is exposed to di-radical monomer of o-chloro-p-xylylene. These monomers immediately polymerize on the surface via non-terminating free radical process. Although this polymer improves the thermal stability and chemical/moisture resistance of the metal, it shows very poor tendency for adhering to stainless steel [79, 73]. In order to promote the adhesion, pre-treatment with the γ-methacryloxypropyltrimethoxysilane (γ-MPS) (Gelest, Morrisville, PA) is recommended for the surface of steel [80]. γ-MPS (Silane) consists of a hydrolyzable alkoxy group bonded to the silicon atom and allows formation of a covalent metalosiloxane bond by hydrolyzing the metal surface (Figure 6). The o-

chloro-p-xylene di-radical, which is generated in the vapor deposition process, reacts with the acrylate group of the siloxane side chain to form a covalent bond [81].

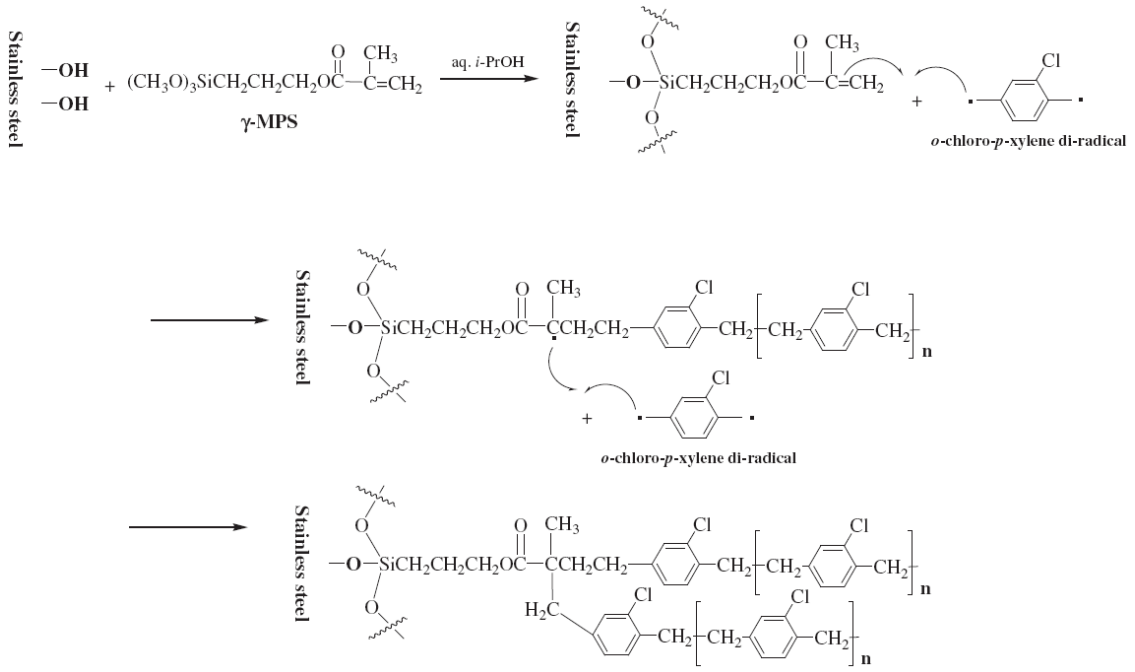

Figure 6. The process of polymerization of parylene C and silane on stainless steel [77].

There have been some efforts for measuring the adhesion energy between stainless steel 316L and parylene C with and without silane [6, 70, 81]. However, the adhesion mechanisms of these materials are not fully understood because of the nature of the adhesion phenomenon that happens in Nanoscale, in a very short amount of time as well as the interference of many other parameters, such as mechanical properties of the materials, with the experimental measurement. Therefore, using new technique such as atomistic simulations can provide insightful information of the mechanism of adhesion, to achieve a better understanding of interfacial properties of these materials.

In this research, we present a combination of atomic force microscopy (AFM) experiment and Maugis–Dugdale contact theory to compute the adhesion energy between parylene C / 316L and silane added Parylene C / 316L. We also have used atomistic simulations to

quantify work of adhesion (a thermodynamic parameter) at room temperature to provide more intuitions to the mechanism of adhesion. The atomistic simulation also has been used to investigate the effect of the body temperature and the aqueous environment inside the body on the adhesion between parylene C / 316L with and without silane to impart useful information for better design.

4.1.1 Experimental Method

In the experiment, the AFM has been used to measure the pull-off forces obtained for DES surface pairs. Figure 7 presents a schematic of a typical force-displacement curve associated with the AFM adhesion experiments in which contact mode is used to bring a desired coated tip into contact with the desired coupon. In this process, the pull off forces can be obtained from maximum deflection of the tip during retract phase. It is possible to convert these adhesion forces into interfacial adhesion energies, using contact mechanics that consider the radii and deformation characteristics of the mating surfaces [6, 70].

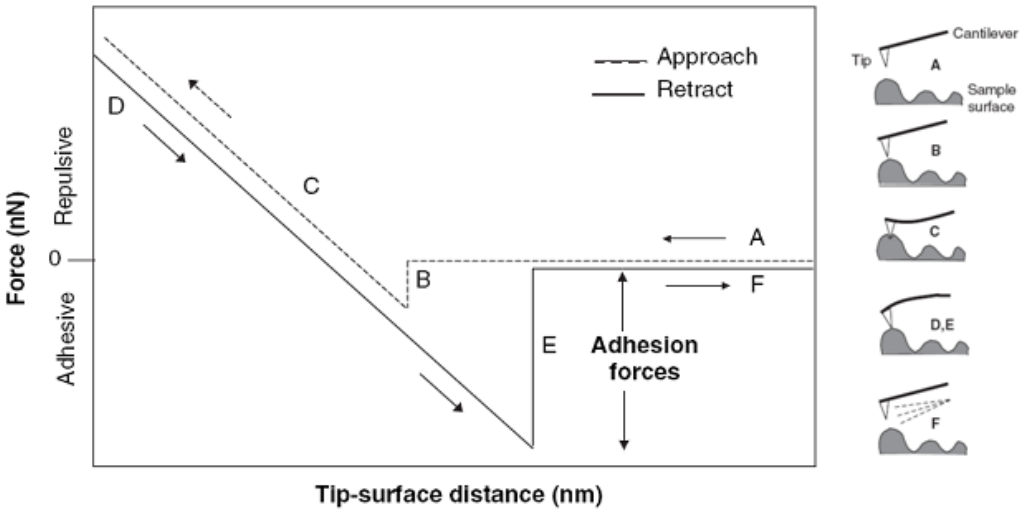

Figure 7. Schematic of the contact mode of AFM [82]. The attraction forces can be obtained from stage E which is the moment of the separation of the tip from the coupon.

The experiment measures the interaction forces between parylene C / bare 316L and silane added parylene C / bare 316L. In the coating process of the tips, silane is first

deposited and cured on the metallic substrates, and parylene C is applied by pyrolysis of dichloro-(2,2)-paracyclophane and vapor deposition of the resulting diradical [76]. Therefore, since there is no covalent bond between pair surfaces, all the forces are due to non-bonded energies which are the results of van der Waals and electrostatic energies.

Several possible contact theories are available for calculating the adhesion energies from interaction forces (Figure 7).

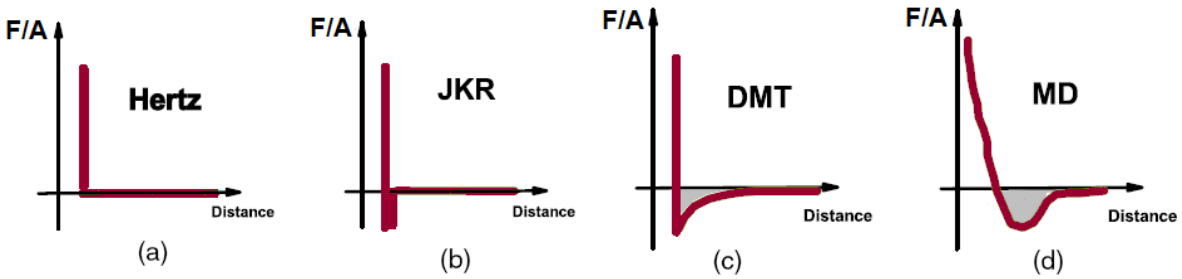

Figure 8. Typical force per unit area displacement curve for (a) Hertz, (b) JKR, (c) DMT, and (d) actual MD adhesion models regarding contact theory of spheres.

In this work, the general case of MD model, which is an idealized model and consistent with the measured AFM adhesive forces, has been chosen. This model considers a constant maximum force, predicted by Lennard-Jones potential for estimation of the van der Waals interactions, all over the contact region, until a separation h_0 is reached. h_0 is given by Equation (28) such that the maximum attraction force, σ_0, and the work of adhesion, γ, matches those of Lennard-Jones potential.

$$\gamma = h_0\sigma_0 \tag{28}$$

Maugis defied a transition parameter, λ that is used to decide on which models are applicable. This is given by,

$$\lambda = 2\sigma_0\left(\frac{R}{\pi K^2\gamma}\right)^{\frac{1}{3}} \tag{29}$$

where, R is the combined reduced radius of the radii of the coated AFM tip, $R_{1,}$ and the average asperity on the 316L substrate, R_2, given by Equation (29) and K is the reduced modulus of elasticity of the tip and sample given by equation (30).

$$\boldsymbol{R = \frac{R1R2}{(R1+R2)}} \quad \textbf{(30)}$$

$$\mathbf{K = \frac{4}{3}\left(\frac{1-\nu_1^2}{E_1} + \frac{1-\nu_2^2}{E_2}\right)^{-1}} \quad \textbf{(31)}$$

For $\lambda < 0.1$, the DMT model is valid and for $\lambda > 5$, JKR model. Value between 0.1 and 5 correspond to the intermediate model [66].

Parameter,α, is defined by conversion Equation (32) such that α = 0 and α = 1 correspond to the DMT and JKR respectively, and the intermediate cases are when 0.07 < α < 0.98. [66].

$$\boldsymbol{\lambda = -0.924.\ln(1 - 1.02\alpha)} \quad \textbf{(32)}$$

With the definition of α, nondimensional parameter $\bar{F}$, known as the reduced load or the net compressive load on the contact, is computed given by [66],

$$\boldsymbol{\bar{F} = 0.267\alpha^2 - 0.767\alpha + 2.000} \quad \textbf{(33)}$$

The pull-off forces measured from AFM, F_{adh}, along with $\bar{F}$ are used to calculate the work of adhesion from Equation (33).

$$\boldsymbol{\gamma = \frac{F_{adh}}{\pi R\bar{F}}} \quad \textbf{(34)}$$

The Equations (28) to (34) are used to calculate the work of adhesion from AFM measured forces.

4.1.2 Computational Method

Stainless steel 316L is a metal consists mainly of iron (%60 - %70), chromium (%16-%18) and nickel (%10-%14). Surface x-ray diffraction of this metal shows that the surface has a thin layer of oxide and this layer has a structure similar to chromite,

$FeCr_2O_4$ [83, 84]. Hence, since the structure of stainless steel 316L is complicated, in this study the structure of chromite crystal cell is considered as a simplified model for 316L in all atomistic simulations. Figure 9 shows the layers of DESs.

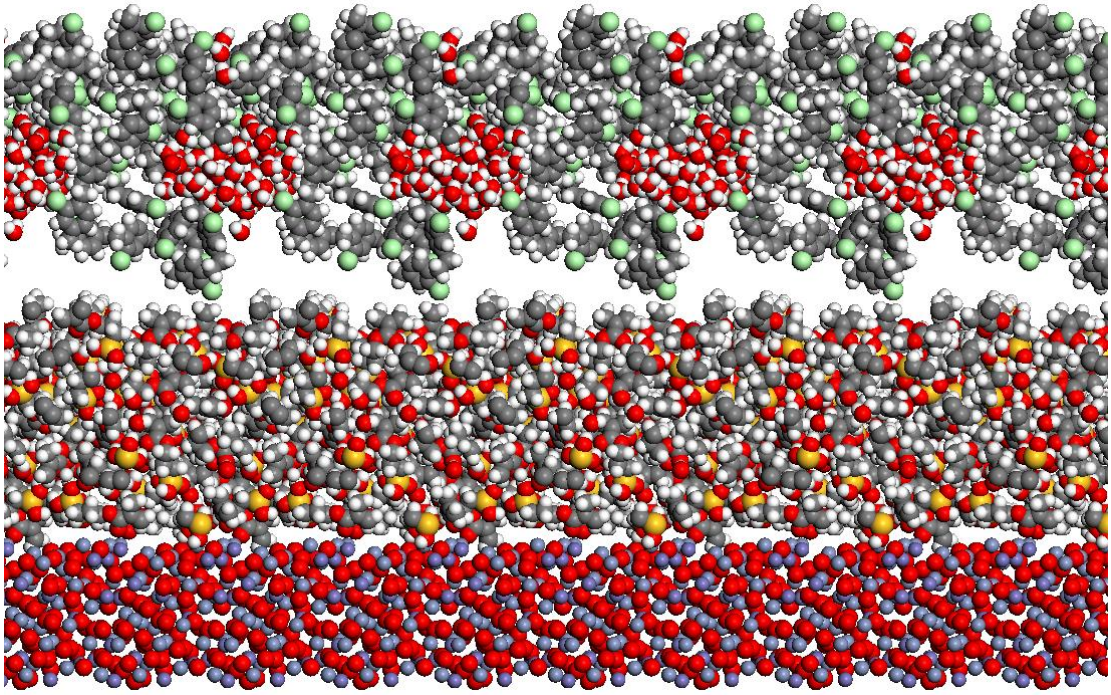

Figure 9. Schematic illustration of the layers in the structure of drug eluting stent. The top layer is mixture of parylene C and water on top of the silane layer. The bottom layer is chromite which represents a layer of oxide on the 316L steel.

The process of simulation starts with creating the optimum configurations of parylene C and silane layer along with chromite surfaces, by finding their minimum energies. The layers are placed on top of each other and equilibrated followed by dynamic simulations which are carried out in 300ps with the 1fs time steps. This time period was enough for the system to reach the stability in which there are no significant changes in non-bonded energy and the fluctuations of kinetic energy are negligible around a preset value of $3k_bTN/2$, where k_b is Boltzmann constant, T is temperature and N is total number of molecules. In order to investigate the effect of temperature on the adhesion, the

simulations are performed in 295K and 310K, referring to room and body temperature, respectively.

Material Studio (MS) software (Accelrys, San Dieg, USA), is used for all molecular calculations. The forcefield used in the calculations is COMPASS (condensed-phase optimized molecular potentials for atomistic simulation studies) [85]. COMPASS is a powerful forcefield, which is used for atomistic simulation of condensed material. It is one of the first ab initio forcefield, which is parameterized and validated with the experiment results, using condensed-phase properties [86]. Therefore, it is an accurate and reliable forcefield for predicting mechanical, structural and thermo-dynamical properties of vast range of molecules and atoms.

In COMPASS, the non-bonded energies include van der Waals and electrostatic energies, with hydrogen bonds being a natural consequence of these energies. Therefore, the non-bond interactions are described by the Lennard-Jones function of van der Waals energies and Coulombic representation of electrostatic energies (Equation 35).

$$\boldsymbol{E_{non-bonded} = E_{vdW} + E_{Elect}} \quad \textbf{(35)}$$

4.1.2.1 Modeling of Chromite

Chromite is an iron chromium oxide, $FeCr_2O_4$ with the crystal structure of FCC (Face Centered Cubic), symmetry group FD-3M and the cell dimensions of a = b = c = 8.85 Å and the angles of $\alpha = \beta = \gamma = 90^{o}$. This crystal cell is optimized using Smart algorithm which is a cascade of the steepest descent, ABNR, and quasi-Newton method. The non-bonded summation methods are calculated using Ewald for electrostatic with 0.001 kcal/mol accuracy and atom-based for van der Waals with truncation of atoms, further than cut-off distance of 12.5 Å. The parameter, u, that defines the fractional coordinates

of oxygen, iron, and chromium, in the form of (u_i, u_j, u_k), are 0.7376, 0.8750 and 0.5, respectively. COMPASS forcefield estimates the density of the crystal cell at 4.30 g/cm^3 and it is in good agreement with the experimental data which is 4.40 g/cm^3. The crystal is cleaved on the close-pack plane (1 1 1) and the four top most atoms were equilibrated while all other atoms are fixed. Vacuum slab with the dimensions of 37.534 x 37.534 x 16.161 Å^3 is created from equilibrated system.

4.1.2.2 Modeling Parylene C and γ-MPS

Initially, the polymer chain is generated with 100 monomers units from the parylene C monomer that is shown in Figure 10a. The number of monomers in the chain is not representative of the real polymer as the real chain has more than 10,000 repeating units. However, it is enough to model the chain ends, close to the surface. Many monomers on the real chain do not participate in the adhesion process due to non-bonded cut-off distance.

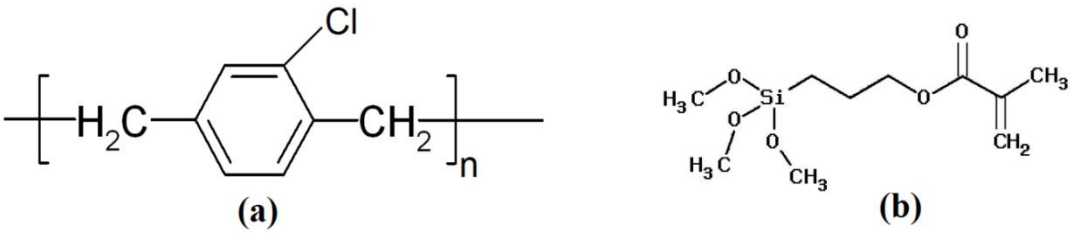

Figure 10. (a) Parylene C monomer (b) **γ**-methacryloxypropyltrimethoxysilane (**γ**-MPS) molecule.

Amorphous Cell module with COMPASS forcefield has been used to create four minimized layers of this oligomer chain with a desired density of 1.289 g/cm^3 [87] at 300K. The first layer consists of just the oligomer and the other three oligomer chains fill with water for the amount of %20, %40 and %60 of the total system weight, respectively.

Each configuration then subjected to molecular dynamics simulation to let the atoms relax the high energy in the structure [88]. Initially, the NVT dynamics is carried out for 80ps for $8x10^4$ steps at 300K, followed by $8x10^4$ steps NPT dynamics at the temperature of 400K and pressure of 1atm. Finally, the system cools down to the desired temperature in an NPT dynamics for $8x10^4$ steps at the pressure of 1atm. Table 4 shows the dimensions and density of each layer, after relaxation process.

Table 4. The properties of polymer layers.

Amount of water (% of weight)	**Dimensions ($Å^3$)**	**Density (g/cc)**
0	26.68 x 26.68 x 26.68	1.22
20	23.41 x 23.41 x 23.41	1.11
40	26.12 x 26.12 x 26.12	1.05
60	30.51 x 30.51x 30.51	1.01

In order to model the silane, forty eight silane molecules (Figure 10b) are packed into a box, using Amorphous Cell module, with COMPASS forcefield, to make a layer with the desired density of 1.045g/cm^3 [89]. The relaxation procedure similar to parylene C modeling is applied to prepare the silane layer for the MD simulation. The outcome of this process is a layer of silane with the dimension of 24.18 x 24.18 x 24.18 $Å^3$ and density of 1.16 g/cm^3.

4.1.2.3 Interface Modeling and Molecular Dynamics Simulation

Two different assemblies are prepared to simulate the conditions of the experiments, parylene C / chromite (P/C) and silane-parylene C/ chromite (S-P/C). Since the parylene C layer is vapor deposited after silane treatment, the outer layer of coated tip is parylene C and touches the 316L coupon during the experiments. Therefore, in the S-P/C simulation, a layer of parylene C is in contact with the chromite and the silane layer is placed on top of the polymer layer. These assemblies are placed in a box with periodic

boundary conditions which are extended 50 Å in Z direction to make the upper layer interact merely with the lower one. These systems are equilibrated followed by NVT dynamics simulations at 295K for 300,000 steps with the time steps of 1fs.

Eight different interaction assemblies are prepared to simulate the conditions inside the body. parylene C with %0, %20, %40 and %60 amount of water on chromite (P0/C, P20/C, P40/C and P60/C) and silane added parylene C with the same amount of water on chromite (P0-S/C, P20-S/C, P40-S/C and P60-S/C). Since the layer of silane in DES is between parylene C and 316L, the layer of silane is in contact with the chromite and parylene C layer is placed on top of the silane.

The energy of interaction ($E_{adhesion}$) is calculated by,

$$\boldsymbol{E_{adhesion} = E_{total} - (E_U + E_L)} \quad \textbf{(36)}$$

The total energy (E_{total}) is the energy of whole system. The energy of upper layer (E_U) is the energy of polymer or silane without the contribution of the lower layer. The lower layer energy (E_L) is calculated by removing the upper layer from the system [90].

The work of adhesion is calculated by,

$$\boldsymbol{W = \frac{E_{adhesion}}{A_c}} \quad \textbf{(37)}$$

where, A_C is the van der Waals contact area between the molecules of the two layers. This area is obtained from the projected area of the upper layer on the top of the surface [90]. Contact area is calculated by using MATLAB image processing codes to obtain ratio of the projected area to the total area.

4.1.3 Results and Discussion

The adhesion forces between parylene C coated AFM tips and 316L steel is measured at 320 ± 48 nN and silane added parylene C coated AFM tips and 316L steel is measured at

257 ± 105 nN (Figure 11) [81]. These results imply that the adhesion forces decreases when the silane is added to the system.

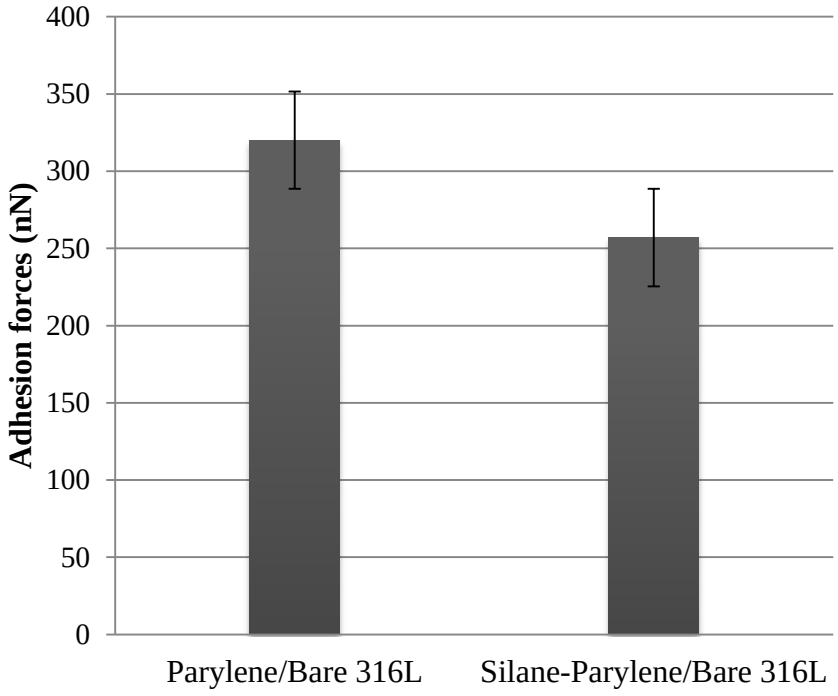

Figure 11. Interaction forces of parylene C and silane added parylene C with 316L stainless steel.

In order to find the work of adhesion from equations (27) to (33), h_0 is considered to be half of the non-bonded cut off distance which is 12.5Å and the curvatures of the AFM tips are obtained from the scanning electron microscopy (SEM) images (Table 5). These data along with the 316L steel coupon grain size which is 12 ± 2 μm are used in the equations to calculate λ and work of adhesion. By carrying out an iterative calculations, the work of adhesions are found to be 0.18 ± 0.0243 J/m^2 with λ = 2.22 for parylene C / 316L and 0.15 ± 0.0609 J/m^2 with λ = 1.94 for silane added parylene C / 316L. Since λ < 0.1 corresponds to DMT model and λ > 5 corresponds to JKR model, MD model is an appropriate model for these materials to calculate the adhesion energies from the Nano-scale AFM experiments. These numbers follow the same trend as those of the adhesion

forces and indicate that the physisorption between parylene C and 316L is affected by silane and decreases as silane is added to the system.

Table 5. AFM tip geometries.

Coating	Average Radius (nm)	Radius STD (nm)
Parylene C	370	31
Silane-parylene C	354	23

The experiment is simulated in atomistic level and the works of adhesion are estimated at 0.078 J/m^2 for P/C and 0.065 J/m^2 for S-P/C. This shows that adding silane to the system slightly decreases the adhesion between parylene C and chromite. The reasons for this downturn are investigated by breaking down the adhesion energy into van der Waals and electrostatic energies. Van der Waals and electrostatic energies between parylene C and chromite decrease from 0.065 J/m^2 to 0.054 J/m^2 and 0.013 J/m^2 to 0.011 J/m^2, respectively, as silane is added to the system. This suggests that the main interactions between parylene C and chromite are due to the van der Waals forces which are almost five times greater than the electrostatic, and adding silane on top of the parylene C changes the conformations and orientations of the polymer chain in such a way that causes a diminution of both energies.

Figure 12 juxtaposes the experimental and simulation results at room temperature. Chromite model can estimate the interfacial characteristic of parylene C / 316L and silane added parylene C / 316L, accurately. Although the adhesion energies of the chromite model are less than the experimental results, the trend is similar.

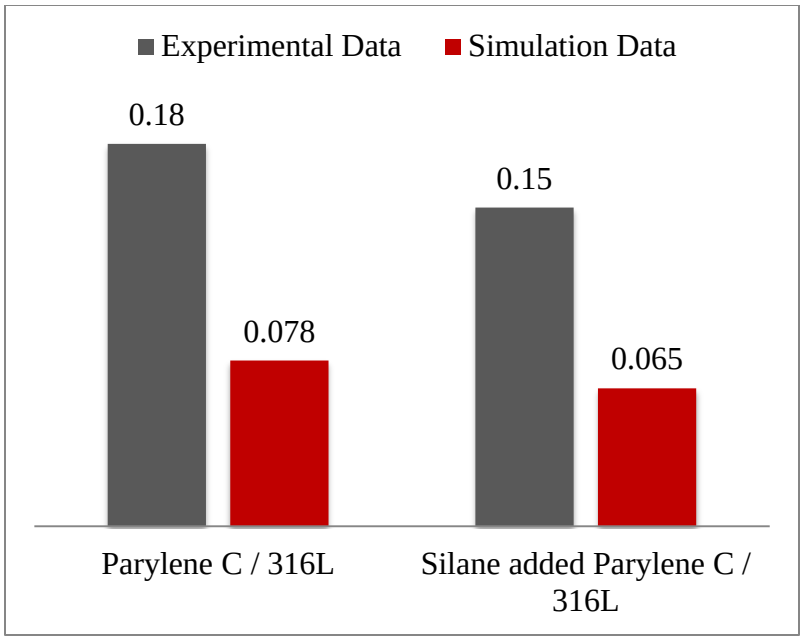

Figure 12. Experimental and simulation results of work of adhesion (J/m^2) between parylene C / 316L steel and silane added parylene C / 316L steel at room temperature.

Knowing the fact that the chromite model results are in good agreement with the experiment, this model has been used to predict the effect of water and body temperature on the adhesion energies between DES layers.

The effect of water (percentage of weight) permeating the parylene C on the work of adhesion between parylene C and chromite is clearly evident from Figure 13. As the water molecules penetrate into the polymer chains, the adhesion energy between polymer and metal substrate decreases. Comparing the results of simulation at 295K and 310K without the presence of water molecule implies that increasing temperature decreases the adhesion energies between these layers.

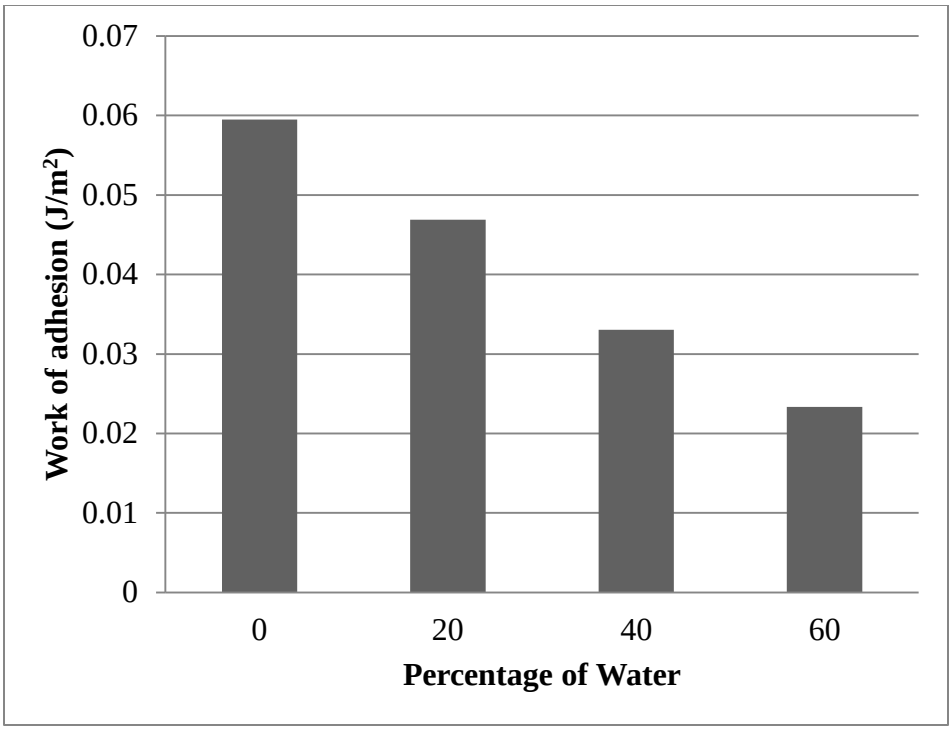

Figure 13. Effect of water molecules permeating parylene C on the work of adhesion between parylene C and chromite.

Looking into the van der Waals and electrostatic energies of these layers reveals that an increase in the amount of water molecules through the parylene C increases the electrostatic energies between parylene C and chromite slightly while it decreases the van der Waals energies significantly (Figure 14). Water molecules are polar molecules due to the difference in electro negativities between the oxygen and hydrogen. These molecules tend to attach to so-called hydrophilic surfaces which are usually predominantly polar [91]. Therefore, water molecules recede from hydrophobic parylene C [92, 93] and approach the metal substrate because of its polarity and create a layer of water between polymer and the substrate. This layer decreases the concentration of the polymer chain close to the surface and, according to Lennard-Jones correlation, decreases the van der Waals interactions.

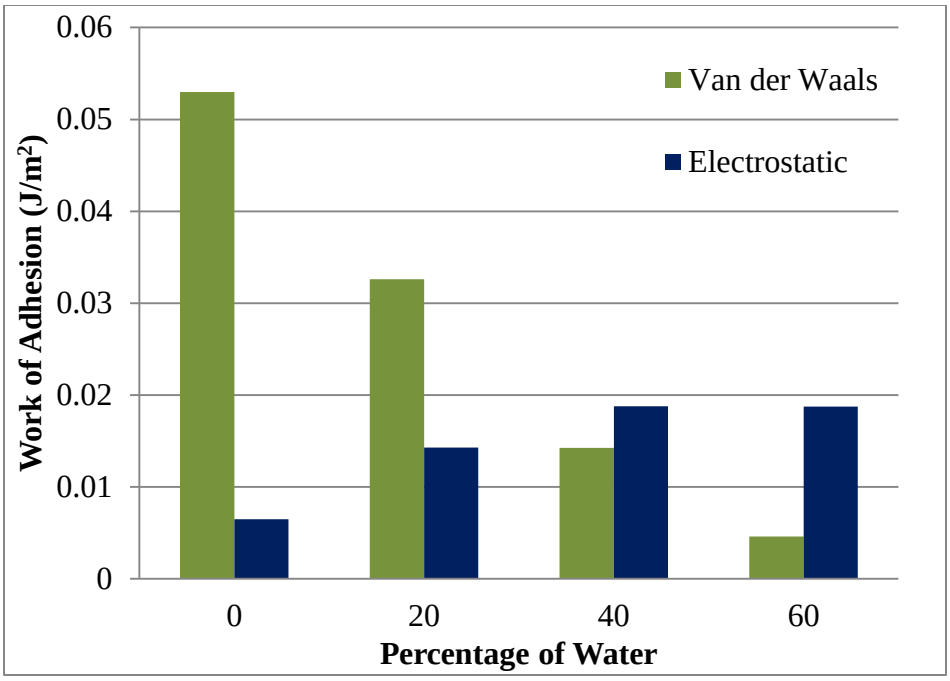

Figure 14. Effect of water molecules permeating parylene C on the van der Waals and electrostatic energies between parylene C and chromite.

Figure 15 elucidates the aggregation of water molecules between the polymer and metal substrate by showing the concentration of parylene C and chromite molecules in Z axis for each simulation. In Figure 15a, when there are no water molecules, the polymer chain penetrates into the metal substrate about 2 Å and rapidly increases to maximum value. This shows that the majority of the polymer molecules align near the metal surface. Figure 15b and c show that the concentrations for 20% and 40% of weight water molecules shift to the right and finally Figure 15d clearly shows the concentration of the polymer accumulates far from the surface.

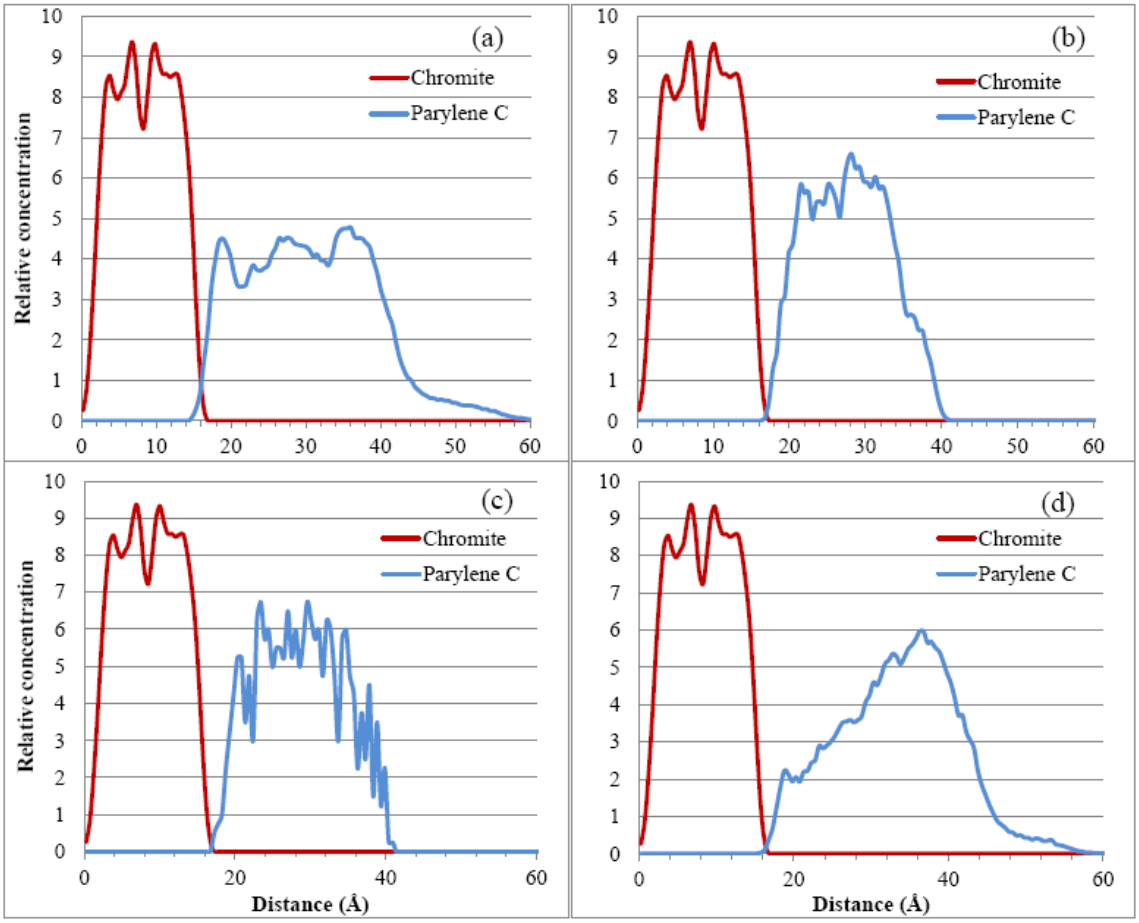

Figure 15. Concentration of parylene C and chromite molecules in Z direction for (a) 0% (b) 20% (c) 40% (d) 60% of weight water molecules.

4.2 Orthopedic Hydrogel-Hydroxyapatite Composite

Design of biomimetic synthetic scaffolds for guided repair and regeneration of skeletal tissues is of significant clinical interest. Natural bone is a composite of collagen, a protein-based hydrogel template, and inorganic dahilite crystals (with hydroxyapatite, HA, being the major inorganic component). The unusual combination of a hard inorganic material and an underlying elastic hydrogel network endows native bone with unique mechanical properties, such as low stiffness, resistance to tensile and compressive forces and high fracture toughness. Photocrosslinked polymethacrylates and their functionalized copolymers, characterized with their high water retention capacity and biocompatibility, are attractive hydrogels for tissue engineering applications. One major challenge for their application as 3-dimensional synthetic bone substitute, however, is to realize high-affinity integration of HA with the hydrogel scaffold.

Song et al. previously showed that poly (2-hydroxyethyl methacrylate), or pHEMA, a well-studied biocompatible synthetic hydrogel polymer could be surface mineralized with nanocrystalline HA with robust interfacial adhesion using a novel heterogeneous mineralization method [94-96]. Furthermore, Song et al. demonstrated that up to 50 wt% HA could also be structurally integrated with the 3-dimensional interior of the pHEMA hydrogel to generate structural composites that can resist high compressive loads without exhibiting brittle fractures [97]. The side chains of pHEMA is terminated with hydroxylated residues, which are richly present in type I collagen [98] and are believed to be responsible for the observed favourable integration of pHEMA with HA. These structural composites have also shown great in vivo performances for scaffold-guided repair of critical long bone defects in rodents [99, 100]. Here we hypothesize that pHEMA derivatives, when functionalized with other appropriate mineral nucleating side

chains [101], may further improved the interfacial adhesion strength in these structural composites. In particular, we hypothesize that the negatively charged carboxylate residue, a common motif found in acidic non-collagenous bone matrix proteins and recognized to play important roles in mediating templated biomineralization [102-104] would be a rational biomimetic element to be incorporated in the side chain of functional pHEMA. To test this hypothesis, a reliable method to quantitatively evaluate the adhesion energies between potential HA-binding ligands and HA crystals on an atomic scale needs to be developed. In this paper, we investigated the interfacial affinity between well-defined surfaces of HA single crystal whiskers [105] and pHEMA vs. pGLYMA which are functionalized with hydroxylated and carboxylated side chains, respectively. A combination of atomistic simulations and Atomic Force Microscopy (AFM) experiments was used to study the pHEMA and pGLYMA pairwise adhesion energies with well-defined HA crystal. Models of crosslinked structures of pHEMA and pGLYMA were used to simulate elastic properties of the two polymers and to predict the adhesion energies at the interfaces of pHEMA/HA and pGLYMA/HA. The simulation results were then verified by a novel AFM experimental method developed earlier by Rahbar et al. [106, 107]. The details of the experimental method and computational process are presented in the following sections.

4.2.1 The Experimental Measurement of Adhesion

The AFM was used to measure the adhesion forces between the HA single crystal whisker surface (100) and the two polymers, pHEMA and pGLYMA. The HA whiskers were prepared by molten salt synthesis. The AFM tips were coated with pHEMA and pGLYMA by a multi-step coating process and validated by SEM. The AFM coated tips, in contact mode, were brought into contact with the coupons of HA whiskers, with the

(100) faces exposed, and pulled off. The adhesion forces between the tips and the substrate cause a bending deflection on the tips during the retraction phase (Figure 16). The deflections were recorded for each experiment and the forces were computed by using the equation of a cantilever beam that correlates the deflections with the forces.

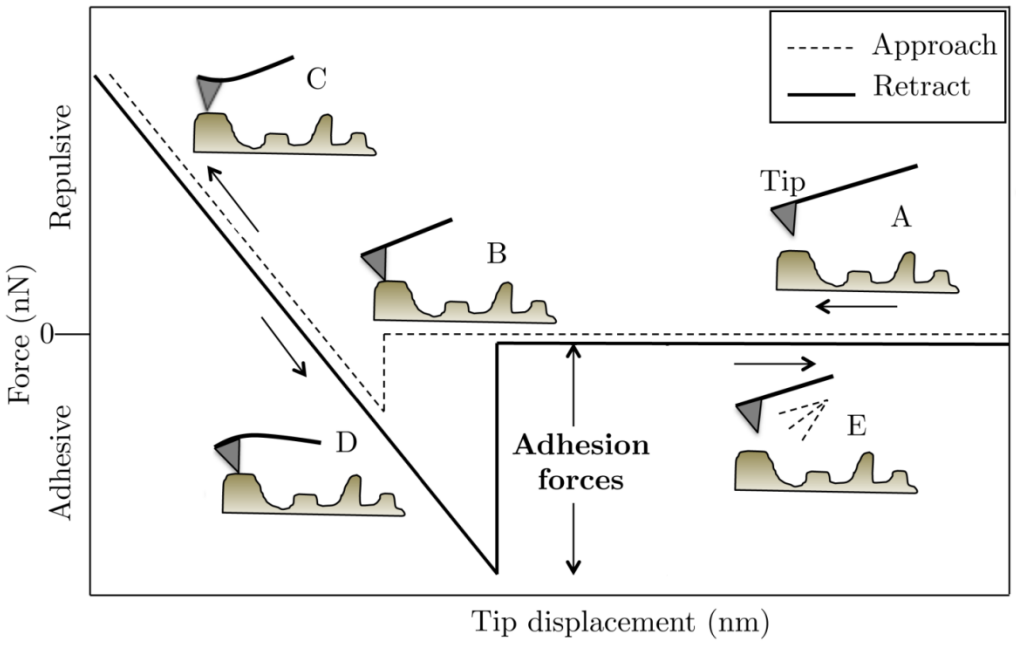

Figure 16. Schematic of the interaction of AFM tips with surfaces in the contact mode.

4.2.1.1 Sample preparations

HA single crystal whiskers were prepared using molten salt synthesis. Briefly, commercial polycrystalline HA powders were dry-mixed with potassium sulfate at a K_2SO_4/HA weight ratio of 1.6. The mixture was placed in a clean crucible and heated in a high-temperature furnace from room temperature to 1190 °C at a rate of 5 °C/min and held at 1190 °C for 3.5 h before it was being cooled to room temperature. The single-crystal HA whiskers were separated from the solid mass by washing with Milli-Q water at 90 °C three times. The whiskers were then air-dried and characterized by optical microscopy to reveal morphologies (Figure 17) consistent with literature [101].

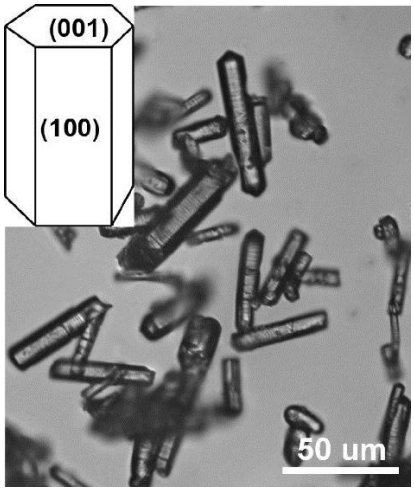

Figure 17. Optical micrograph of the single crystal HA whiskers prepared by molten salt synthesis and the schematic (inset) of the (100) face to be utilized for the AFM study.

Functional monomer GLYMA was prepared and purified as previously reported [100]. Commercially HEMA (Aldrich) was freshly distilled under reduced pressure and EGDMA (Aldrich) was passed through resins to remove radical inhibitors prior to use.

To generate a robust layer of surface coating of pHEMA or pGLYMA on the AFM tip, we first covalently bonded a self-assembled monolayer (SAM) of thiolated methacryalte on gold-coated AFM tips. This SAM layer is designed to not only improve the wetting of the hydrogel cocktail (HEMA/EGDMA or GLYMA/EGDMA along with radical initiators) with the AFM tip, but also to covalently participate in the crosslinking to generate the pHEMA and pGLYMA surface coating. Specifically, the AFM tips were sputter coated with 10 nm chromium-nickel and afterwards a layer of 30 nm gold [108]. A self-assembled monolayer of 2-(methylthio) ethyl methacrylate was then formed on the Au-coated AFM tip before dipping the tip to respective cocktails of hydrogel monomer, crosslinker and initiators in previously published ratios [100], and crosslinked under UV (254 nm) for 1 min. As shown in Figure 18, this strategy successfully led to the uniform coating of the AFM tips with a thin layer of pHEMA or pGLYMA crosslinked by 2 wt%

EGDMA.

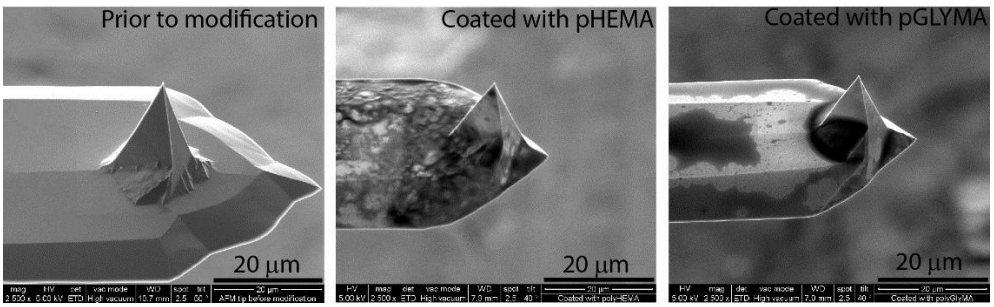

Figure 18. SEM micrographs of the AFM tips before and after coating with a thin layer of pHEMA or pGLYMA crosslinked by 2 wt% EGDMA. The "defective" hydrogel at the base of the coated tips was caused by beam damage during the imaging.

In order to acquire reliable AFM measurement, even distribution of a single layer of HA whiskers is needed to guarantee that the coated tips will touch the HA whiskers rather than the underneath surface. The HA whiskers also need to be stably fixed to the substrate to prevent their movements during the retraction phase. Accordingly, a thermal wax was used to mount the HA whiskers on the glass substrate [109]. Specifically, a piece of wax was placed on the glass substrate and heated up to 70 °C until the wax softened. Immediately upon removing the glass substrate from the heater, the HA whiskers were sprinkled over as the wax starts to solidify. After 15 minutes at the room temperature, the thermal wax becomes solid. The surface of the substrate was brushed carefully to remove large agglomerates of the HA, leaving a layer of scattered HA whiskers predominantly exposing their (100) faces.

In order to merely measure the adhesion forces between the hydrogel-coated AFM tips and the HA whiskers, two samples were prepared; one with only paraffin wax and one with HA whiskers sprinkled over and adhered to the surface of the wax. As a control, measuring the adhesion of the AFM tips with wax only helps us determine whether the tip was in contact with the HA whiskers or with the wax during the measurement.

Multiple points of the samples were tested to determine the adhesion forces between the tips and HA crystals. For each point, ten adhesion force measurements were collected for a proper statistical analysis.

4.2.1.2 Data Analysis

The AFM tips were brought in contact with HA whiskers in the contact mode of AFM. The adhesion forces were computed from the maximum deflection of the tips times a constant, which is the stiffness of the beam. The deflections were obtained from the difference between point E and A on the approaching and retracting curves in Figure 16.

To calculate the adhesion energies from the measured forces, different contact theories developed by Maugis–Dugdale (MD) [67], Derjaguin-Muller-Toporov (DMT) [64] and Johnson-Kendall-Roberts (JKR) were used [63]. JKR model consider the contact as compliant with large radius of curvature. DMT is suitable for stiff contacts with small radius of curvature. The MD model is an intermediate case between JKR and DMT that decides which contact condition is applicable for modelling the adhesion between two surfaces by defining a transition parameter λ.

$$\boldsymbol{\lambda = 2\sigma_0\left(\frac{R}{\pi K^2 \gamma}\right)^{\frac{1}{3}}} \quad \textbf{(38)}$$

where σ_0 is maximum attraction stress. R is the combined reduced radius of the two surfaces in contact (AFM tips and HA particles), and K is the reduced modulus of elasticity of the tip and sample which are given by,

$$\boldsymbol{R = \frac{R_1 R_2}{R_1 + R_2}} \quad \textbf{(39)}$$

$$\boldsymbol{K = \frac{4}{3}\left(\frac{1-\upsilon_1^2}{E_1} + \frac{1-\upsilon_2^2}{E_2}\right)^{-1}} \quad \textbf{(40)}$$

where R_i, E_i and υ_i (i=1, 2) are the radii, Young's moduli and Poisson's ratios of the coated AFM tips and the HA crystals, respectively.

For values of $\lambda < 0.1$, the DMT model is valid while the JKR theory is the relevant model for values of $\lambda > 5.0$. Consequently, values of λ between 0.1 and 5 correspond to the intermediate situation. In this study MD equations were used to calculate the λs and the adhesion energies (Υ) between the polymers and the HA particles. Youssefian et al. discussed the calculation process of adhesion energies from MD equations, in details [107].

4.2.2 Atomistic Simulations of hydrogels

Molecular dynamics techniques were used to simulate the adhesion between polymers and HA particles. COMPASS (Condensed-phase Optimized Molecular Potentials for Atomistic Simulation Studies [110]) force field, a suitable force field for atomistic simulation of condensed matters, was used to simulate the physical and mechanical properties of the polymers. It is one of the first ab initio-based force fields that is parameterized and validated with the experiment results, using condensed-phase properties [110]. Therefore, it is an accurate and reliable force field for predicting mechanical, structural and thermodynamic properties of a vast range of molecules and atoms. Nevertheless, the performance of this force field in atomistic simulations of the HA, pHEMA and pGYMA was verified in this study.

4.2.2.1 Modeling hydroxyapatite surface

In order to model the hydroxyapatite (HA) surface, hexagonal unit cell with symmetry group of P63 and lengths of a = b = 9.421 Å, c = 6.881 Å and the angles of $\alpha = \beta = 90^{\circ}$ and $\gamma = 120^{\circ}$ were modeled and optimized using steepest descent approach followed by conjugate guardian method. The non-bonded summations were calculated using Ewald for electrostatic with accuracy of 0.001 kcal/mol and atom-based for van der Waals with truncation of atoms further than cut-off distance of 12.5 Å. The properties of the model

were obtained to assess the suitability of COMPASS force field for atomistic modeling of HA. The computed density of HA from atomistic simulation was about 3.10 g/cc that was close to the experimental value of 3.14 g/cc. The modulus of elasticity estimated to be 40.30 GPa, 40.30 GPa and 62.15 GPa in X, Y and Z directions, respectively. The experimental values for these properties depend on the volume fraction and porosities, and vary between 7 GPa to 103 GPa [111-114]. The Poisson's ratio of HA is also a function of volume fraction and porosities, and changes from 0.15 to 0.3. The estimated Poisson ratio from atomistic simulation was 0.29.

HA unit cell was cleaved on (100) surface which is the predominant surface of the HA whiskers exposed to AFM tips in the AFM experiments. (0 1 0) surface was also created to be used in the simulations because this plane is the major plane in the morphology of the biological material due to the effect of collagen matrix [115]. Furthermore, the electrostatic characteristic of this plane is not neutral due to negatively charged OH group on one surface and positively charged Ca atoms on the other surface. A super cell with the dimensions of $3.44 \times 3.77 \times 1.57$ nm^3 was created from the equilibrated (0 1 0) and (1 0 0) HA surfaces.

4.2.2.2 Modeling of the polymers

Cross-linking a polymer is widely believed to improve the mechanical properties. Here, ethylene glycol dimethacrylate (EGDMA) was used as the cross-linking agent for pHEMA and pGLYMA. These polymers were crosslinked with 2% (by weight) EGDMA, according to the standard radical polymerization protocol [94, 116]. Therefore, the molecular mass ratio of crosslink agent (EGDMA) to hydrogel monomer (HEMA) was found to be 0.0129. The number of repeating units of EDGM, e, HEMA, h, and GLYMA, g, can be calculated by the following equation,

$$\frac{EGDMA}{HEMA} = \frac{e}{h} = \frac{EGDMA}{GlyMA} = \frac{e}{g} = 0.0129 \quad (41)$$

By choosing 3 EDGMA units, we need 234 HEMA or GLYMA to have a correct ratio of the polymers to the crosslinked agent. These 234 repeating units should create 3 chains of the polymer that are crosslinked by the 3 agents. Hence, there should be 80 repeating units in each polymer chain: 78 repeating units (234/3=78) plus 2 units as the connection site for the agents (Figure 19).

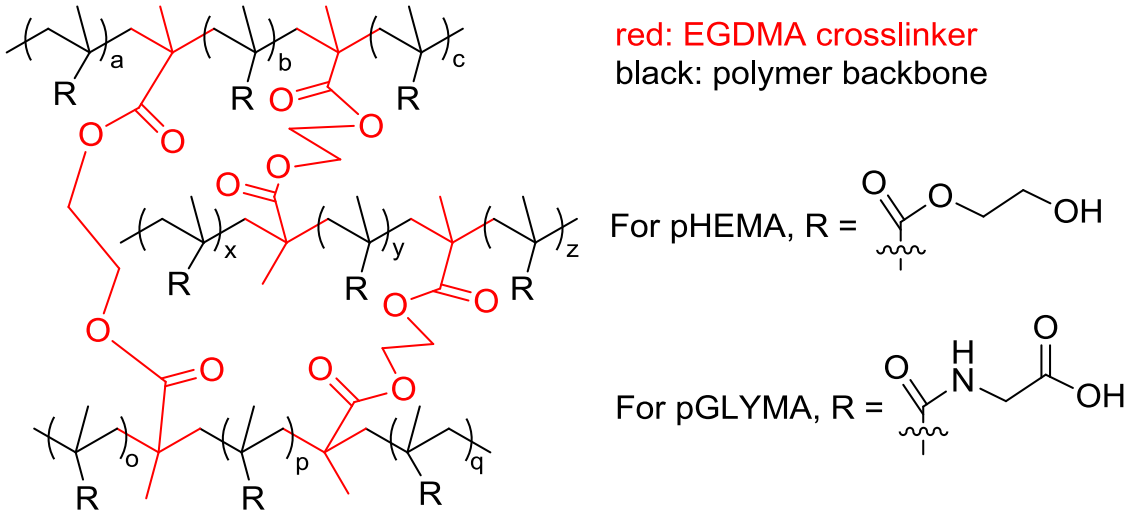

Figure 19. Depiction of the crosslinked hydrogel molecular networks.

Three oligomers of polymer with 80 repeating units along with 3 molecules of EDGMA were constructed in periodic boundaries with the dimensions of 3.2 × 3.2 × 1.7 nm^3. Each cell was filled with 3942 water molecules to simulate the real conditions. The cell was going through a relaxation process [117] which starts with compressing at high pressure (5000 bar) for 80 ps at 300K, followed by NVT dynamics at 600K and 300K, successively, for 10 ps and 20 ps. Subsequently, an NPT dynamics was performed at 1 bar and 300K for 80 ps. If the density was lower than the experimental density, the first two steps were repeated. The final simulation cells had dimensions of 3.4 × 3.4 × 3.4 nm^3 with a density of 1.2 g/cc and 1.27 g/cc for pHEMA and pGLYMA, respectively. These

values are in good agreement with the experimental values.

To compare the mechanical properties of pHEMA and pGLYMA, the Young's moduli of the polymers were calculated. The periodic structures of polymers were expanded along each direction to the maximum strain amplitude of 0.04 in 9 steps. In each step the stresses were obtained from virial stress expression:

$$\boldsymbol{\sigma} = \frac{\mathbf{1}}{\boldsymbol{V}}\left[\sum_{\boldsymbol{i=1}}^{\boldsymbol{N}} \boldsymbol{m_i}\left(\boldsymbol{v_i v_i^T}\right) + \sum_{\boldsymbol{i<j}} \boldsymbol{r_{ij} f_{ij}^T}\right] \quad \textbf{(42)}$$

which is commonly used to relate the computed stress in molecular dynamics to continuum stresses.

To simulate the interaction of the interfaces of the polymers and HA, multiple assemblies of polymer chains on top of the HA substrate were created. Three different configurations of each polymer were chosen to remove the effect of the initial conditions on the results. After optimizing the polymers, NVT dynamic simulations were performed at 300K for 300 ps with time steps of 1 fs. The interaction energy was calculated from the final trajectories of simulations, by using the following equation:

$$\boldsymbol{E_{Interaction}} = \boldsymbol{E_{total}} - \left(\boldsymbol{E_{surface}} + \boldsymbol{E_{polymer}}\right) \quad \textbf{(43)}$$

where E_{total} is the energy of the HA surface and the polymer, $E_{surface}$ is the energy of the HA surface without the polymer and $E_{polymer}$ is the energy of the polymer without the HA surface.

4.2.3 Results and Discussion

4.2.3.1 Experimental measurement of adhesion energies

In order to ensure that the tips merely touch the HA whiskers, first they were tested on the smooth surface of paraffin wax with an average surface roughness of ~ 97 nm as shown in Figure 20. The tips, then, were tested on the surface of paraffin with the HA whiskers (Figure 21) which has a roughness in the micron meter range.

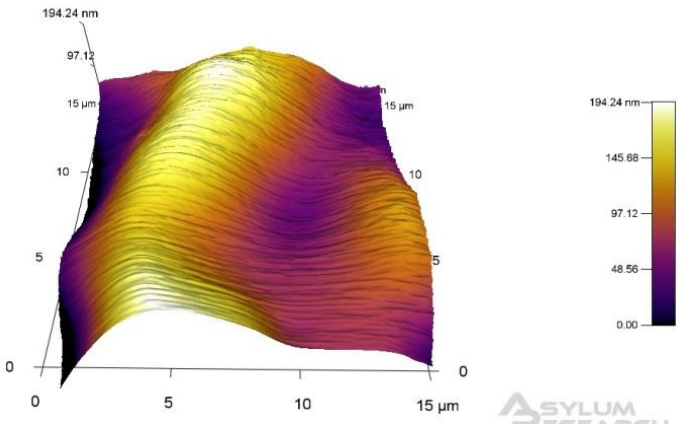

Figure 20. A typical 3D image of the surface of thermal wax samples. The smooth surface of the wax was used to detect the HA particles on the substrate.

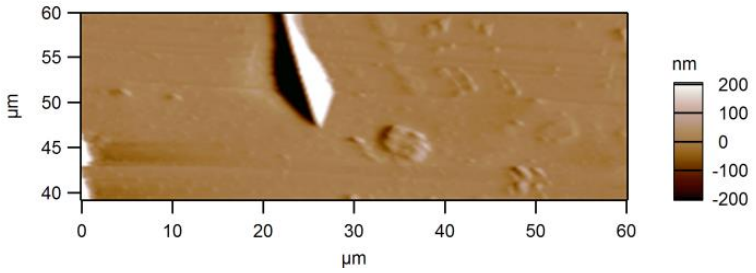

Figure 21. Single layer of HA particles fixed firmly in the thermal wax. This method helps the alignment of the HA crystals in the desired direction.

The adhesion forces between the tips and the paraffin were computed from deflection-displacement curve of the tips and paraffin wax (Figure 22a) to be about 23.72 nN. Figure 22b and c show the deflection-displacement curves of pHEMA and pGlyMA coated tips with HA whiskers which are about 104.4 ± 18 nN and 152.5 ± 22 nN, respectively. The statistical analysis shows higher adhesion forces between HA whiskers and the AFM tips coated with pGLYMA and pHEMA than the adhesion forces between paraffin wax and the tips. This implies that the tips only measured the adhesion between HA and hydrogels.

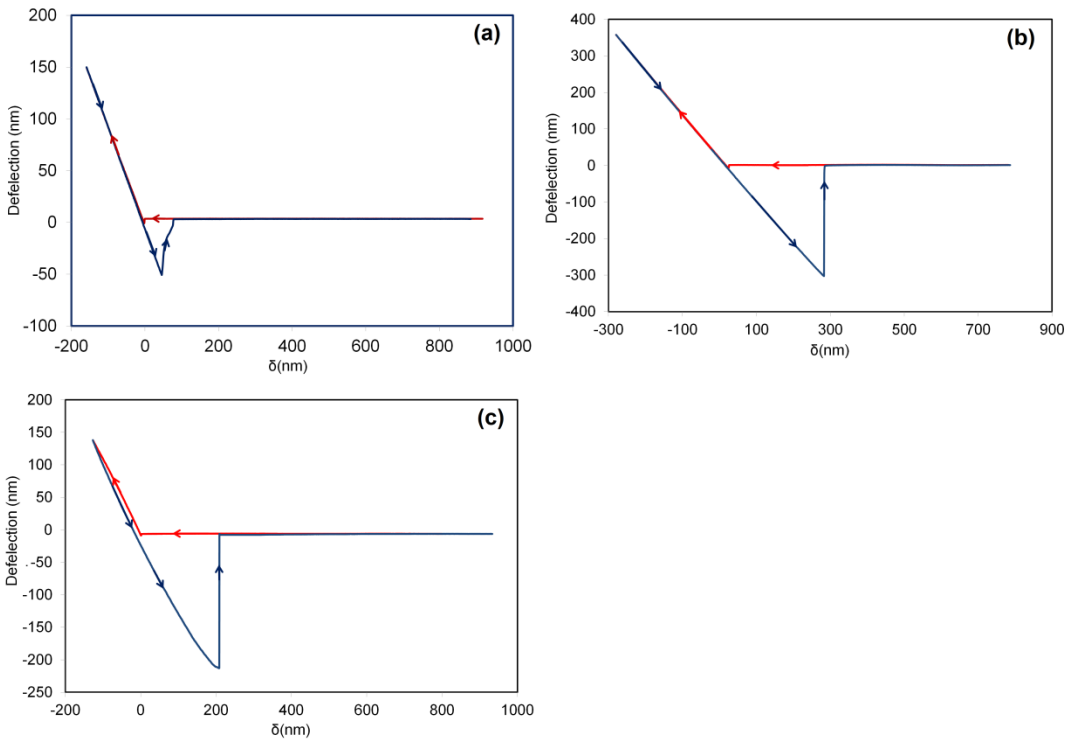

Figure 22. a) Typical deflection-separation curve of AFM tips coated with pHEMA tapping on Paraffin. Typical deflection-separation curve of AFM tips coated with b) pGLYMA and c) pHEMA tapping on HA surface. The stiffness of the tips is very close for different polymers and the analysis shows higher adhesion force between pGLYMA/HA than pHEMA/HA particles.

To find the adhesion energies per unit area from MD model equations, h_0 was considered to be half of the non-bonded cut off distance which is 12.5Å. Since the width of the HA whiskers are in the micron meter range the reduced radius of the adhesion energy is simply the radius of the AFM tips. The radius of coated AFM tips was measured to be around 175 nm using SEM.

By carrying out iterative calculations, the adhesion energies between HA whiskers and pGLYMA and pHEMA were found to be 184.3 mJ/m^2 with λ = 8.45 and 126.2 mJ/m^2 with λ = 8.41, respectively (Table 6). Since $\lambda > 5$ corresponds to JKR, the contact between these hydrogels and HA whiskers, is compliant with large radius of curvature. Hence, these results suggest that pGLYMA, with carboxylated side chains, may present

further advantage than the hydroxylated uncharged pHEMA in achieving better bonding affinity with HA in the design of hydrogel-hydroxyapatite structural composites.

Table 6. Experimental results of Adhesion forces and energies.

	Tip Stiffness (N/m)	Force (nN)	Adhesion (mJ/m^2)
pGlyMA	0.58 ± 0.02	152.5 ± 22	184.3 ± 20
pHEMA	0.61 ± 0.01	104.4 ± 18	126.2 ± 16

4.2.3.2 Atomistic Simulations of adhesion energies

The Young's moduli of the pHEMA and pGLYMA, computed from the stiffness matrices, are presented in Table 7. The average Young's moduli of pHEMA and pGLYMA were estimated to be 6.17 ± 0.81 MPa and 9.67 ± 0.55 MPa, respectively. The pHEMA Young's modulus is in good agreement with the respective experimental measurements that are between 1 to 17 MPa under humidity conditions of 98% and 16% RH, respectively [118]. The results suggest that the pGLYMA exhibits stiffer mechanical behaviour than pHEMA.

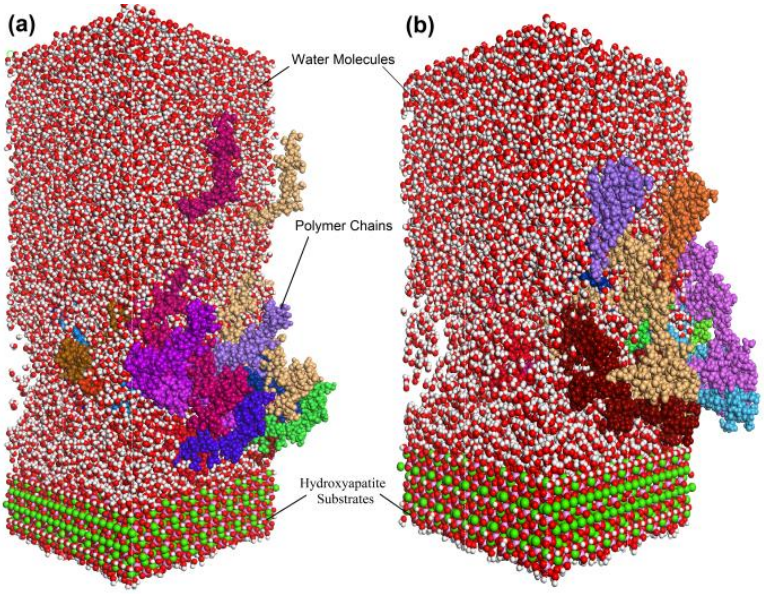

Figure 23. The results of the molecular dynamics simulations of a) pGLYMA b) pHEMA on HA (100) surface.

Table 7. Young's Modulus computed from the simulations

Hydrogel	Young's Modulus (MPa)
pGlyMA	9.67
pHEMA	6.17

The adhesion energy per unit area between the hydrogels and different surfaces of HA were calculated from the trajectories of atomistic simulations (Figure 23) and shown in Figure 24. The adhesion energies between (100) surface and pGLYMA estimated at 77.2 mJ/m^2 while the adhesion between the same surface and pHEMA calculated to be around 32.9 mJ/m^2.

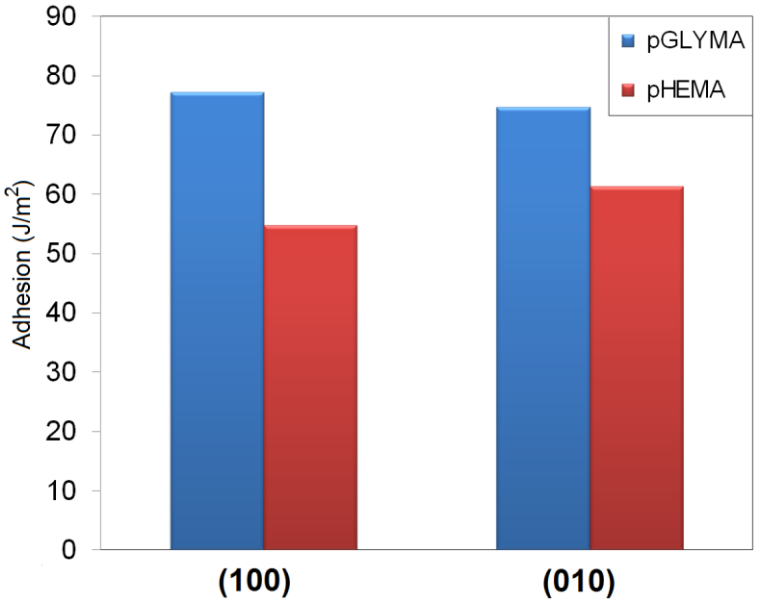

Figure 24. The calculated adhesion energy per unit area of pHEMA and pGLYMA on different surfaces of HA.

The adhesion energies between (010) surface and pGLYMA and pHEMA were estimated to be around 71.9 mJ/m^2 and 32.2 mJ/m^2, respectively. Comparing simulation results with the experiments suggests that the pHEMA and pGLYMA models can properly estimate the interfacial characteristic between these materials and HA. Although the adhesion

energies calculated from the simulation results are less than that of experiments, the trends are quite consistent. This trend implies that the pGLYMA exhibits greater adhesive tendency than pHEMA to HA. The components of adhesion energies, electrostatic and van der Waals, were calculated and are presented in Table 8 and Table 9.

Table 8. The adhesion energy and its components on HA (100)

Hydrogel	Adhesion (mJ/m^2)	Van der Waals (mJ/m^2)	Electrostatics (mJ/m^2)
pGLYMA	77.26	0.52	76.74
pHEMA	54.74	2.23	52.51

Table 9. The adhesion energy and its components on HA (010)

Hydrogel	Adhesion (mJ/m^2)	Van der Waals (mJ/m^2)	Electrostatics (mJ/m^2)
pGLYMA	74.72	1.86	72.86
pHEMA	61.35	0.60	60.74

These results elucidate that the major factor in the interaction between HA and the hydrogel is electrostatic energies which is higher between HA and pGLYMA than between HA and pHEMA. The main difference between pHEMA and pGLYMA molecular structures is the uncharged side chain hydroxyl end groups for pHEMA and the negatively charged side chain carboxylate end groups for pGLYMA. In addition, pHEMA links its side chains to the main chain via an ester linkage whereas pGLYMA via an amide linkage. These two differences cause more electrostatic attraction between the pGLYMA and HA compared to pHEMA and HA which results in higher adhesion energy.

5 Nanomechanics of Bamboo Fibers

5.1 Molecular Origin of Strength and Stiffness in Bamboo Microfibrils

Bamboo is the fastest growing naturally occurring bio-composite material [119] that reaches maturity within months. As one of the well-known materials with high strength-to-weight ratios, bamboo has been used as renewable and sustainable structural material for decades [120, 121]. The structure of bamboo consists of epidermis, parenchyma cells and vascular bundles, which are surrounded by supporting fibers. Researchers attribute the remarkable mechanical properties of bamboo to the presence of these fibers within the bamboo culm [122, 123]. The unique mechanical properties of bamboo fibers come from their composite structure, in which cellulose fibrils are surrounded by a matrix of mainly lignin and hemicellulose [124-126].

Prior researchers have investigated the mechanical properties of cellulose fibers, lignin and hemicellulose and their interactions [127-137]. Among those previous efforts, Besombes and Mazeau [138, 139] performed molecular dynamics simulations on the assembly of a threo guaiacyl β-O-4 dimer of lignin and different surfaces of cellulose Iβ. They showed that the adsorption of lignin onto cellulose is surface-dependent. They also found a major contribution of van der Waals interactions onto (100) face and a major influence of hydrogen bond interactions in the adsorption of lignin onto (110) and ($\bar{1}$10) faces. Linder et al. [140] performed non-equilibrium molecular dynamics simulations of lignin and cellulose. They found that lignin strongly associates with the cellulose nanofibril. Nevertheless, few attempts have been made to use the crosslinked structure of

lignin-hemicellulose to study the mechanical behavior of bamboo microfibrils and the interfaces of its matrix with cellulose nanofibrils.

In this study, we investigate the role of each material in the mechanical properties of bamboo microfibrils as well as the underlying mechanisms of interactions between the matrix and cellulose nanofibrils. With this aim, molecular models of lignin, bamboo hemicellulose and a crosslinked structure of these two materials as representative matrix materials were developed. Molecular dynamics techniques were used to elucidate the structures, mechanical properties of the lignin, hemicellulose and the matrix. It is important to note that the properties of the systems under study are known to be sensitive to the percentage of water molecules [137]. Therefore, no water molecules were added to the simulations to remove this effect from the results.

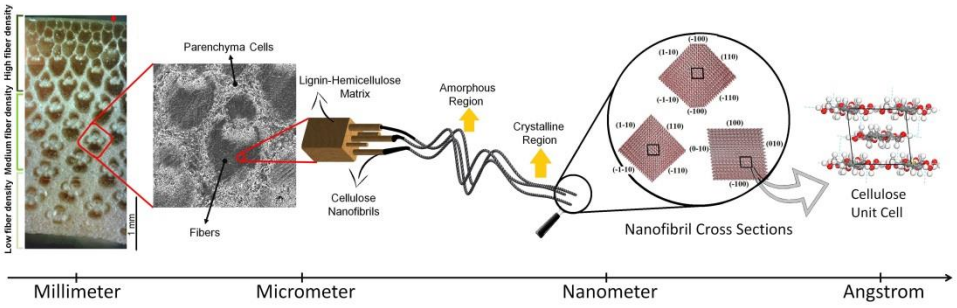

Figure 25. Hierarchical structure of bamboo. The vascular bundles in the parenchyma matrix are surrounded by supporting fibers which are known to be the source of remarkable mechanical properties of bamboo. Bamboo fibers have a hierarchical structure in which cellulose nanofibrils reinforce the intertwined hemicellulose-lignin matrix. Linear chains of glucose with orderly hydrogen bonds form the crystalline regions of nanofibrils while irregular hydrogen bonds create the amorphous regions. The cross section of these nanofibrils is either rectangular or hexagonal.

5.1.1 Molecular Structure of Bamboo Microfibrils

The most abundant carbohydrate in bamboo is cellulose with the volumetric percentage ranging from 40 to 45%. Figure 25 presents the structure of cellulose at different scales down to its building unit cell. Cellulose nanofibrils are formed by assembling linear chains of aldehyde sugars often referred to as glucose molecules, to make either

rectangular or hexagonal cross sections with diameters of 3 to 5 nm [141, 128]. If the hydrogen bonds between the hydroxyl groups form in an order, highly ordered (crystalline) regions are formed. However, if random hydrogen bonds form, disordered (amorphous) regions develop. [128, 142]. The positions of the hydroxyl groups determine the crystal system. These can be either triclinic or monoclinic unit cells (α or β type, respectively) with latter being the building block of plants such as bamboo. In a bamboo fiber, cellulose nanofibrils are surrounded by lignin-carbohydrate complex (LCC) matrices that mainly contain lignin and hemicellulose with volumetric percentages that ranging from 20 to 30% and 15 to 25% of the bamboo structure, respectively.

Lignin is a natural phenolic macromolecule that is mainly present in the plant's secondary cell wall. It is made up of three main phenylpropanoid subunits, namely p-hydroxyphenyl (H-type), guaiacyl (G-type) and syringyl (S- type) units [143]. The biosynthesis of lignin occurs from different polymerizations of these three subunits. Hence, there are many possible bonding patterns between the individual units. Advancements in spectroscopic methods, however, have enabled scientists to elucidate the leading structural features of lignin [144]. They have also enabled scientists to propose different models for the molecular structure of lignin [145-149]. In this study, a structural model with 28 subunits of lignin proposed by Sakakibara (1980) has been used [150]. In this model, the value of the structural units and the number of protons per C_9 structural units are close to that of spruce milled wood lignin reported by other researchers.

In order to be able to provide rigid support and shape to plants, lignin polyphenols are linked together in three-dimensional crosslinked structures by covalently bonding to

hemicellulose [151-153]. Hemicelluloses are a heterogeneous group of polysaccharides that unlike cellulose, frequently have side chain groups. They are essentially amorphous with little strength [154]. The two major categories of hemicelluloses are glucomannans and xylans. Bamboo hemicellulose has been shown to be a xylan and further characterized as a β-(1→4)-linked-xylopyranosyl backbone, with the presence of L-arabinofuranose and 4-O-methyl-D-glucuronic acid as single side chains (4-O-methy1-D-glucurono- arabino-xylan [155]) that are arranged in an irregular manner. Therefore, the positions of the side chains are not fully determined. With the ratio of uronic acid/arabinose/xylose of 1:3:32 reported [156], we consider hemicellulose structure as hybrid chains of two extreme positions of the side chains, one is a hemi- cellulose structure in which two functional groups are attached to the adjacent xylans and are in the closest possible distance (CPD). The other structure has the functional groups in the furthest possible distance (FPD). A preliminary study of the energy of different configurations revealed that the total energies were of the same order of magnitude. Hence, from the energy point of view, they are both acceptable. Hemicellulose molecules bond to lignin by a variety of chemical bonds, however, most of the evidence refers to ether and ester bonds. Jeffries proposed structures for ester and ether linkages for lignin/uronic acid and lignin/arabinoxylan groups, respectively [157]. These linkage models have been used to create the bonds between lignin and hemicellulose in the crosslinked LCC network.

Based on the structures discussed here, molecular models of the typical lignin, hemicellulose, LCC and cellulose nanofibrils were created. Atomistic simulation techniques were used to study the structure, thermodynamic and mechanical properties,

and interactions of the bamboo microfibril materials. The process of simulation (Figure 26) is thoroughly described in the Method section.

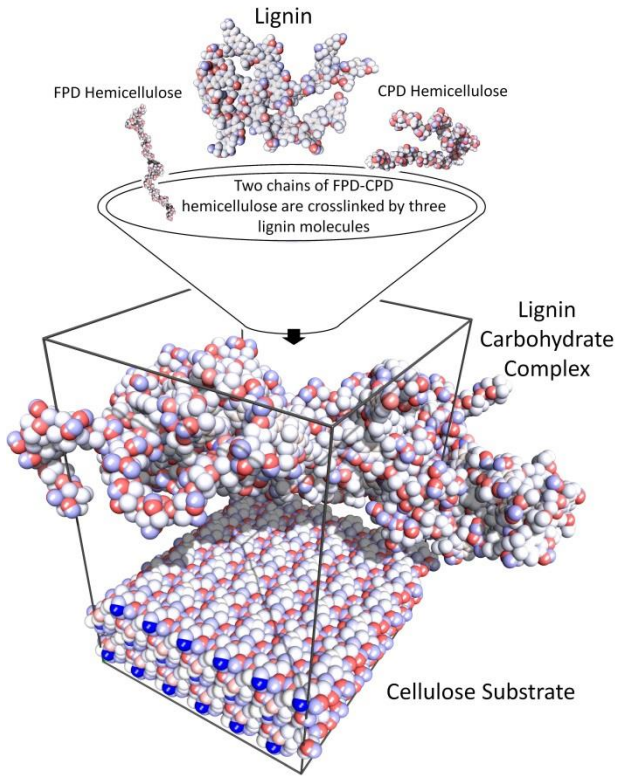

Figure 26. Process of preparing LCC models and atomistic simulation. The hemicellulose chain was created from one chain of CPD and one chain of FPD. Two hemicellulose chains were randomly crosslinked by three lignin molecules to create an LCC structure. Lignin, hemicellulose and LCC models were placed on amorphous cellulose and eight substrates of crystalline cellulose which are representing eight possible faces of nanofibrils. The NVT dynamic simulations at 300K with 1 fs time step were performed for 1.2 ns and the adhesion energies were calculated from the final trajectories.

5.1.2 Results and Discussion

5.1.2.1 Structure

Radial Distribution Functions (RDF) of all atoms in lignin, LCC and hemicellulose structures are presented in Figure 27a. According to this diagram, C−H (second peak, b) is the most abundant covalent bond in these materials. The abundance of the O−H (first peak, a), however, is different. For hemicellulose O−H has almost the same abundance as

C−C, whereas for lignin, C−C is more abundant than O−H. Hence hemicellulose, presumably, is a better candidate than lignin for making hydrogen bonds. This is confirmed by the number of hydroxyl groups in equal volumes of hemicellulose, LCC and lignin which are 1152, 784 and 456, respectively.

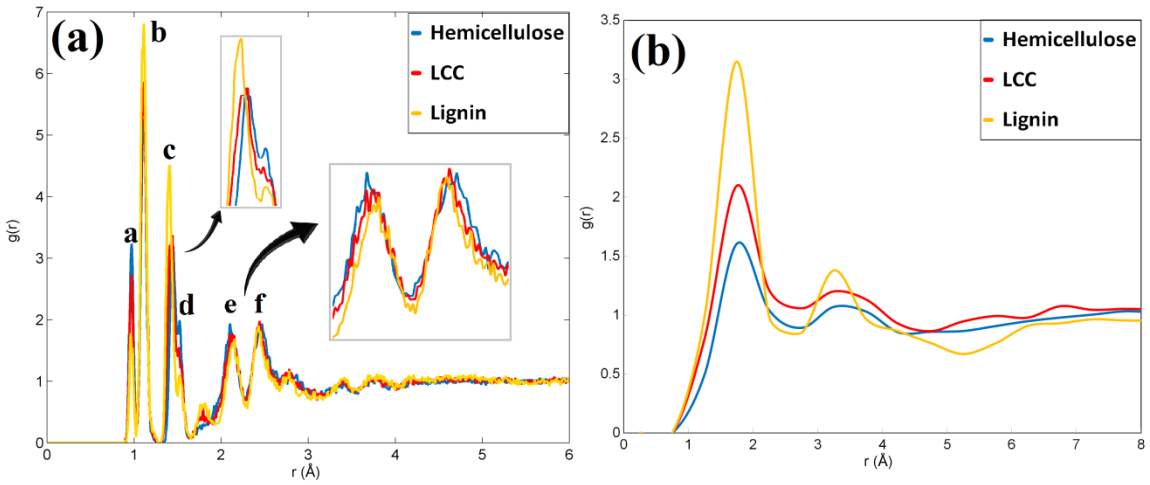

Figure 27. a) Radial distribution functions of all atoms in hemicellulose, LCC and lignin. The first four peaks, a; b; c and d, are related to covalent bonds of O−H, C−H, C−C and C−O, respectively. The fifth and sixth peaks, e and f, exist due to the non-bonded interactions in the systems. b) Radial distribution functions between hydrogen atoms of hydroxyl groups and the oxygen atoms in hemicellulose, LCC and lignin. The first peak at 1.85 Å is related to hydrogen bonds and the second peak at 3.25 Å is attributed to the oxygen-oxygen distance on two hydroxyl groups bonded by hydrogen bonds.

In Figure 27a, the fifth peak is related to the distance between hydrogen and oxygen atoms, connected by hydrogen bonds, and the sixth peak is the distance between two non-bonded carbon atoms on the cyclohexane rings that are connected by a carbon atom (for example, carbon 1 and 3 on the ring). Comparing the abundance of hydrogen bonds (peak e) with the abundance of hydroxyl group (peak a), suggests that in the structure of lignin, most of the hydroxyl group hydrogens participate in hydrogen bonding, whereas in the structure of hemicellulose, the contribution of hydroxyl groups is about 60%.

To further understand the significance of hydrogen bonding, the RDFs between hydrogen atoms of hydroxyl groups and the oxygen atoms were obtained and are presented in

Figure 27b. The first sharp peak at 1.85 Å is related to hydrogen bonding while the secondary broad peak at 3.25 Å is attributed to the oxygen-oxygen distance on two hydroxyl groups bonded by hydrogen bonds. The higher peak of lignin on the diagram confirms that greater numbers of lignin hydroxyl groups participate in hydrogen bonding than those in LCC and hemicellulose. This is because of the geometry of the functional groups, adjacent to these hydroxyl groups. The lignin hydroxyl groups are mostly parts of well-spread hydroxymethyl groups that are extended out from the main chains. The hemicellulose hydroxyl groups, however, are parts of xylose groups, where two hydroxyl groups attach directly to the main chains and are localized on pyranose rings. Hence, lignin hydroxyl groups are more exposed to and more accessible to other hydroxyl groups than those of hemicellulose hydroxyl groups. Therefore, although the hemicellulose structure contains more hydroxyl groups, lignin hydroxyl groups are more efficient in making hydrogen bonds.

The length of hydrogen bonds for all three materials is around 1.85 Å. This is associated with short and strong hydrogen bond interactions. Such strong hydrogen bonds come from the existence of cooperativity. Cooperativity or cooperative effect between hydrogen bonds implies that the hydrogen atom of a hydroxyl group can form a stronger hydrogen bond, if the oxygen creates a hydrogen bond with an adjacent hydroxyl group [40]. This phenomenon is observed in most of the hydrogen bonds in the three materials.

5.1.2.2 Thermodynamic properties

Density and glass transition temperature are good physical properties for evaluating the realism of the conformations. The computed glass transition temperature for LCC, presented in Table 10, falls between the obtained values for hemicellulose and lignin which are in good agreement with the experimental data. The final relaxed conformations

of lignin and hemicellulose have average densities of 1.26 ± 0.02 g/cc and 1.45 ± 0.03 g/cc, respectively. These are comparable with experimental results, in Table 11. Hence the lignin and hemicellulose models estimate the real densities within 5.2% and 4.6%, respectively. These differences are partly attributed to the vacuum condition assumed in the simulation that does not occur in the experiments. The density of LCC relaxed conformation was determined to be 1.34 ± 0.02 g/cc. Implementing the simple rule of mixture density, $(\rho_{LCC} = (m_L + m_H)/(\frac{m_L}{\rho_L} + \frac{m_H}{\rho_H}))$, in which two materials are mixed physically without any changes in mass or volume, the LCC density, ρ_{LCC} , was estimated to be about 1.35 g/cc, using densities obtained from the lignin and hemicellulose simulations. This value is close to the density of the relaxed LCC model. Therefore, the molecular dynamics calculations showed the volume fractions of hemicellulose and lignin do not significantly change in the process of LCC creation. Hence, by using the same equation and the available experimental values for lignin and hemicellulose densities, the true value of LCC density can be estimated at 1.41 g/cc.

Table 10. Glass transition temperature (°C) of lignin, hemicellulose and LCC obtained from the molecular calculations and experiments.

Material	Simulation	Experiment
Lignin	140.26	97-171
Hemicellulose	186.06	140-180
LCC	166.11	N/A

Table 11. Density (g/cc) of lignin, hemicellulose and LCC obtained from the molecular calculations and experiments.

Material	Simulation	Experiment
Lignin	1.26	1.33
Hemicellulose	1.45	1.52
LCC	1.34	N/A

5.1.2.3 Mechanical Properties

The Young's moduli of the hemicellulose, lignin and LCC are presented in Table 12. The average Young's moduli of lignin and hemicellulose were estimated to be 5.90 ± 0.37 GPa and 8.40 ± 0.15 GPa, respectively. These are in good agreement with the respective experimental measurements of 6.7 GPa and 8.0 GPa for nearly dry Pinus radiata lignin and hemicellulose (consisting of arabino-4-O- methylglucuronoxylan which have a close structure to bamboo hemicellulose) [132, 133]. Other studies suggest respective values in the range of 1 to 2 GPa and 3.5 to 7 GPa for different types of lignin and hemicellulose [134, 135]. Hence, the results from the simulations and experiments show that hemicellulose has better mechanical properties than lignin. Performing the same procedure on the LCC model resulted in an average Young's modulus of 6.93 ± 0.31 GPa, which is between the Young's modulus of hemicellulose and lignin.

Table 12. Young's Modulus (GPa) of lignin, hemicellulose and LCC obtained from the molecular calculations and experiments.

Material	Simulation	Experiment
Lignin	5.90	2 - 6.7
Hemicellulose	8.40	3.5 - 8.0
LCC	6.93	N/A

The Young's modulus of a material is defined by its resistance to the tension or compression of bonds. It is affected by factors such as interatomic and intermolecular energies per unit volume. For the amorphous materials, such as LCC, lignin and hemicellulose, applied stresses are mostly used to overcome the non-bonded energies between the molecules. They are also used to unwind the chains rather than directly struggle with the potential energies between atoms or the crosslinking between chains. Therefore, at small strains, non-bonded energies play more important roles in determining the elastic moduli of amorphous materials.

However, the effects of non-bonded energies are not equal. According to the Lennard-Jones function, non-bonded energies with lower equilibrium energies or shorter equilibrium distances exhibit greater resistance to stretching or compressing. Thus, they result in higher Young's moduli. The lower minimum potential energy creates a greater curvature (second derivative) of its energy- distance curve at the point of equilibrium and thus leads to a greater force- distance slope. The same situation holds true for the case where the minimum energies are the same but equilibrium distances are different. In this case, the shorter equilibrium distance results in a greater curvature, which increases the slope of the force-distance curves. Therefore, the strong short-range hydrogen bonds play more important roles in determining the Young's modulus than the other weak long-range non-bonded interactions.

These hydrogen bonds that behave like springs between atoms, distribute differently in the LCC, hemicellulose and lignin structures. The number of atoms connected by the hydrogen bonds is higher for hemicellulose than for LCC which is higher than the number of hydrogen bonds for lignin. The hydrogen bond stiffness can be derived from the potential energy function. The most common expression for Lennard-Jones potential is given by,

$$\boldsymbol{U_{LJ}} = \in [\left(\frac{\boldsymbol{r_m}}{\boldsymbol{r}}\right)^{\mathbf{12}} - \mathbf{2}(\frac{\boldsymbol{r_m}}{\boldsymbol{r}})^{\mathbf{6}}] \quad \textbf{(44)}$$

where r is the distance between the two atoms, ϵ is the depth of the potential well and r_m is the equilibrium distance. The forces between the two atoms can be calculated from the derivative of the potential energy, $= -\frac{dU_{LJ}}{dr}$.

$$\boldsymbol{F(r)} = \frac{\mathbf{12}\in}{\boldsymbol{r_m}}[(\frac{\boldsymbol{r_m}}{\boldsymbol{r}})^{\mathbf{13}} - (\frac{\boldsymbol{r_m}}{\boldsymbol{r}})^{\mathbf{7}}] \quad \textbf{(45)}$$

The stiffness that this force causes around the equilibrium point is obtained from the derivative of the force, $K = -(\frac{dF}{dr})_{r=r_m}$, which results in,

$$\boldsymbol{K = \frac{72\epsilon}{r_m^2}} \quad \textbf{(46)}$$

For hydrogen bond between two hydroxyl groups, the equilibrium distance was calculated to be around 1.85×10^{-10} m, and the potential depth is reported to be 1.2×10^{-20} J [136]. With these values the stiffness of a hydrogen bond in hemicellulose, LCC and lignin was found to be around 25.24 J/m^2. Since these springs bear the stresses in the system, more hydrogen bonds connect more atoms and create a stiffer system. That is why hemicellulose with a 1.08×10^8 J/m^3 hydrogen bond energy density has the highest Young's modulus among the three materials, while LCC with a hydrogen bond energy density of 7.51×10^7 J/m^3 , has a higher Young's modulus than lignin with a 4.46×10^7 J/m^3 hydrogen bond energy density.

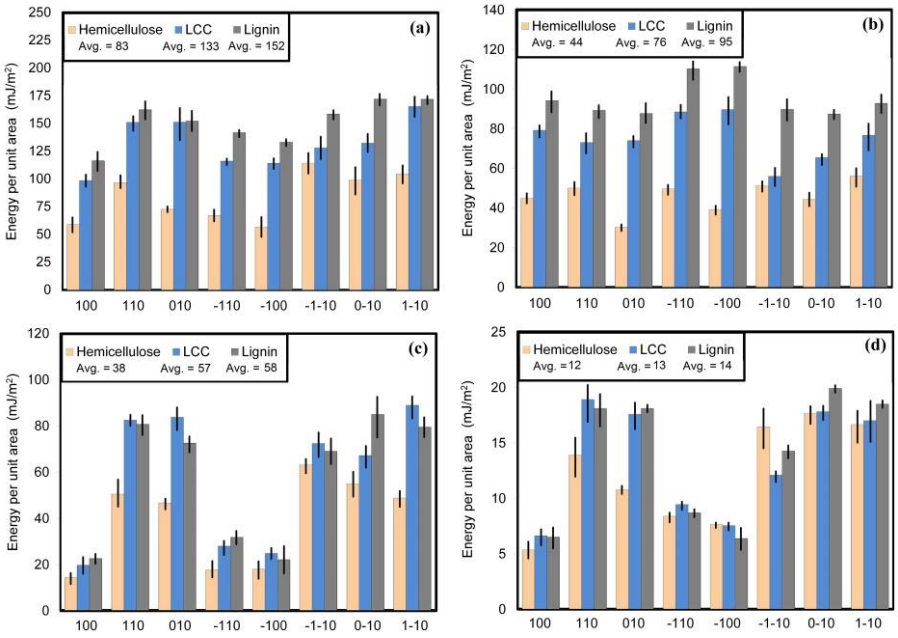

Figure 28. a) The adhesion energy per unit area between different cellulose nanofibril faces and hemicellulose, LCC and lignin. The average energy between lignin molecules and a cellulose nanofibril is higher than the energy between hemicellulose and cellulose nanofibrils. b) The van der Waals energy per

unit area between different cellulose nanofibril faces and hemicellulose, LCC and lignin. Lignin exhibits higher adhesive energy to cellulose nanofibrils than hemicellulose. c) The electrostatic energy per unit area between different cellulose nanofibril faces and hemicellulose, LCC and lignin. The average electrostatic energy between lignin molecules and cellulose nanofibrils exhibit no significant difference from the electrostatic energy between hemicellulose and cellulose nanofibrils d) the hydrogen bond energy per unit area between different cellulose nanofibril faces and hemicellulose, LCC and lignin. The average hydrogen bond energies between cellulose nanofibrils and the three materials are similar.

5.1.2.4 Adhesive Interactions

In the composite structure of a bamboo microfibril, knowledge of adhesive interactions between the different layers determines its strength. Applied stresses on a microfibril are carried either by cellulose nanofibrils, the LCC matrix or the interfaces of these two regions. To investigate the adhesion energies at these interfaces, twenty-four different assemblies of lignin, hemicellulose and LCC on top of cellulose substrates were created, each of which simulates the interaction between one of the materials and one face of the eight possible faces of cellulose nanofibrils. The adhesion energies were computed from final trajectories of the simulations and presented in Figure 28a. Although these results indicate that the overall adhesion energies for these materials are different, their tendencies to adhere to nanofibril faces exhibit almost the same pattern. For each material, the interaction energies of (100) and ($\bar{1}$00) faces are the lowest whereas the energies of other faces vary around an average value. The average adhesion energy between lignin and nanofibril faces was about 152 mJ/m^2. This is higher than adhesion energy between LCC and nanofibril faces which is about 133 mJ/m^2. Hemicellulose with average adhesion energy of around 83 mJ/m^2 shows the lowest adherence to nanofibril among the three materials. This adhesion trend, also, has been shown by Hosoya et al. in the pyrolysis of hemicellulose and lignin with cellulose where lignin-cellulose interactions were significant compare to low hemicellulose-cellulose interactions [137]. Therefore, lignin with greater overall adhesion energy to cellulose is responsible for

providing strong interaction between LCC matrix and cellulose nanofibrils to create strong bamboo microfibrils. To understand the mechanism of interactions between these materials and cellulose, we computed the electrostatic and van der Waals energies, accountable for the adhesion, as shown in Figure 28b and c. These results suggest that the van der Waals energies do not change significantly over the nanofibril faces whereas the electrostatic energies of (100) and ($\bar{1}$00) faces are less than that of other faces. Hence, the electrostatic energy is responsible for reduction of adhesion energy between cellulose (100) or ($\bar{1}$00) faces and hemicellulose, LCC and lignin. The average electrostatic energies between cellulose nanofibril faces and hemicellulose, LCC and lignin are 38 mJ/m^2, 57 mJ/m^2 and 58 mJ/m^2, respectively, and the average van der Waals energies between cellulose nanofibril faces hemicellulose, LCC and lignin are 44 mJ/m^2, 76 mJ/m^2 and 95 mJ/m^2, respectively. It is evident that lignin van der Waals energy is higher around 116% than that of hemicellulose whereas the electrostatic energy are higher just by about 50%. This indicates that the superiority of lignin adhesion energies to cellulose comes from the relatively higher van der Waals energies between cellulose nanofibril and lignin. One of the major components of electrostatic energies at the interface of cellulose nanofibril and hemicellulose, LCC and lignin, is hydrogen bonding which are illustrated in Figure 28d. Regardless of the slightly higher average hydrogen bond energy between lignin and cellulose, all three materials have almost the same hydrogen bond interaction energies with cellulose nanofibrils. The hydrogen bond energies show a similar pattern to the electrostatic energies presented in Figure 28c. In other words, (100) and ($\bar{1}$00) faces have the lowest hydrogen bond energies which are similar to that of the electrostatic interactions. This suggests that different level of hydrogen bond energies at the interface

of nanofibril and hemicellulose, LCC and lignin are the main reason for different electrostatic energies from one face to another, causing the adhesion energies between the matrix and (100) and ($\bar{1}$00) faces of nanofibril to drop.

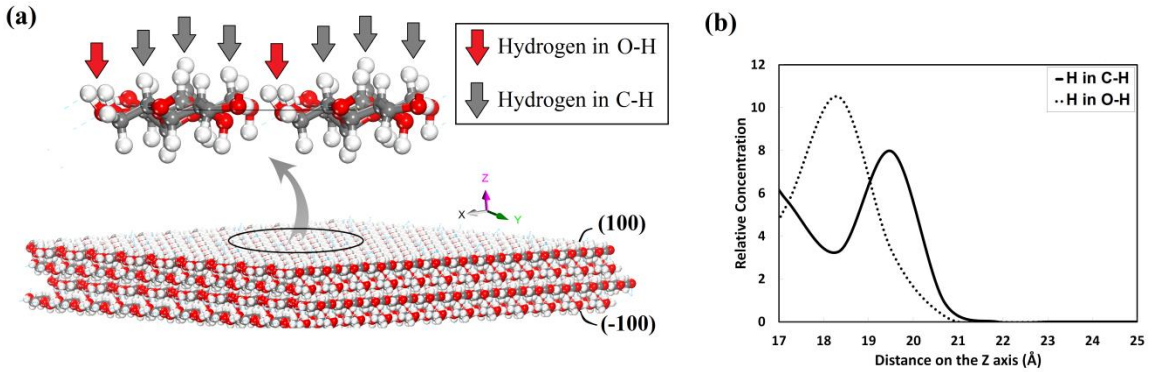

Figure 29. a) Distribution of hydrogen atoms on the (100) and ($\bar{1}$00) surface. These surfaces are covered with hydrogen atoms that are bonded either to oxygen or carbon. The hydrogen atoms that are connected to oxygen are less exposed than the hydrogen atoms connected to carbon because they stay closer to the surface. b) The relative concentration of hydrogen in O−H and C−H along Z axis. Hydrogen in O−H groups accumulates at 18.3 Å, while the hydrogen in C−H groups accumulates at 19.8 Å.

A closer look at the (100) and ($\bar{1}$00) face provides some insights into the weak hydrogen bonds between the faces and the matrix. Figure 29a shows that the surfaces of (100) and ($\bar{1}$00) are covered with hydrogen atoms (white spheres). The hydrogen atoms are bonded either to oxygen or carbon. The hydrogen atoms connected to oxygen are less exposed because they stay closer to the surface while the hydrogen atoms connected to carbon face outwards and are configured for contact with adjacent layers. Therefore, since the accessibility of the hydrogen atoms in O−H groups is less than that in C−H groups, the overall hydrogen bond energy between these two faces and the matrix diminishes. Figure 29b confirms this observation by comparing the relative concentration of hydrogen atoms that are attached to carbon and oxygen. On this diagram, the relative concentration of the top layer of hydrogen on O−H groups and C−H groups are illustrated along the Z axis.

Hydrogen in O−H groups accumulates at 18.3 Å, while the hydrogen in C−H groups accumulates at 19.8 Å. Therefore, the latter group is more exposed to other layers.

This adhesion study proves that the weakest interaction between cellulose nanofibril and LCC occurs at the (100) and ($\bar{1}$00) faces. However, the question of which interface is the weakest link in a microfibril still remains. To answer this question, we need to calculate the other possible locations where defects may occur. Figure 30 shows a schematic of a nanofibril in a matrix of LCC that is woven around both crystalline and amorphous regions. In this structure, the stress can detach either layers of LCC/LCC, interfaces of LCC/crystalline cellulose, LCC/amorphous cellulose, or the stress can fracture the cellulose nanofibril.

The weakest adhesion energy between cellulose nanofibrils and LCC was found to be around 106 ± 8 mJ/m^2. This energy is less than that between the two layers of LCC in the matrix, which was estimated at about 160 ± 29 mJ/m^2. The adhesion energy between LCC and the amorphous region of nanofibrils was close to the adhesion energy of amorphous cellulose/amorphous cellulose interface which were estimated to be 54 ± 10 mJ/m^2 and 44 ± 6 mJ/m^2, respectively. Therefore, the amorphous region of nanofibril has the lowest adhesion energy in the system.

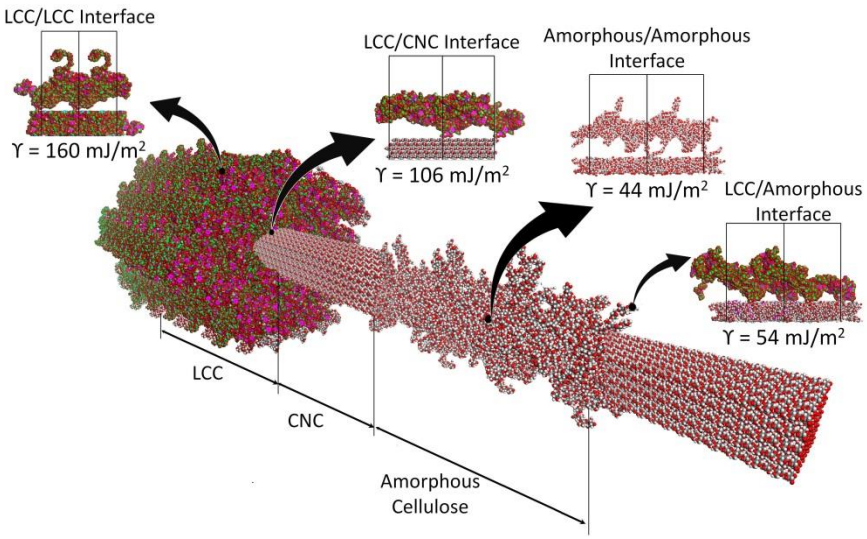

Figure 30. The adhesion energy per unit area between different interfaces, present in a possible nanostructure of bamboo microfiber. The adhesive interaction energy at the interface of LCC layers is the highest among all the regions. The amorphous regions exhibit the lowest adhesive interactions, hence, their interface strength are likely to determine the strength of overall strength of bamboo microfibrils.

5.2 The effect of Water on Mechanical Properties of bamboo fibers

The high number of hydroxyl groups in carbohydrates makes them hydrophilic polymers with reaction sites for hydrogen bond formation with water molecules. Therefore, water molecules permeate through these structures and create hydrogen bonds with the carbohydrate chains. Aggregation of water molecules between the polymer chains significantly changes their mechanical and viscoelastic properties. This effect, however, is not the same for all of these materials due to different hydrogen bond energies and distribution in the materials. Figure 31 illustrates the hydrogen bond distributions of hemicellulose, lignin and the crosslinked structure of these two materials, LCC. Hydrogen bonds behave like springs that connect atoms and constrain their motility. Therefore, they have a determinant impact on the physical properties of these materials. Once water molecules permeate these systems, hydrogen bonds between carbohydrate chains are replaced by the hydrogen bond between the chains and water molecules. The

physical properties changes due to weakening of hydrogen bond network of the polymers and enhancement of molecular motility. Lignin with lower number of hydroxyl groups is hydrophilic compare to other carbohydrate polymers in bamboo fibers [138]. The influence of water molecules on the bamboo fiber nanostructure and physical properties such as density and elastic modulus are different.

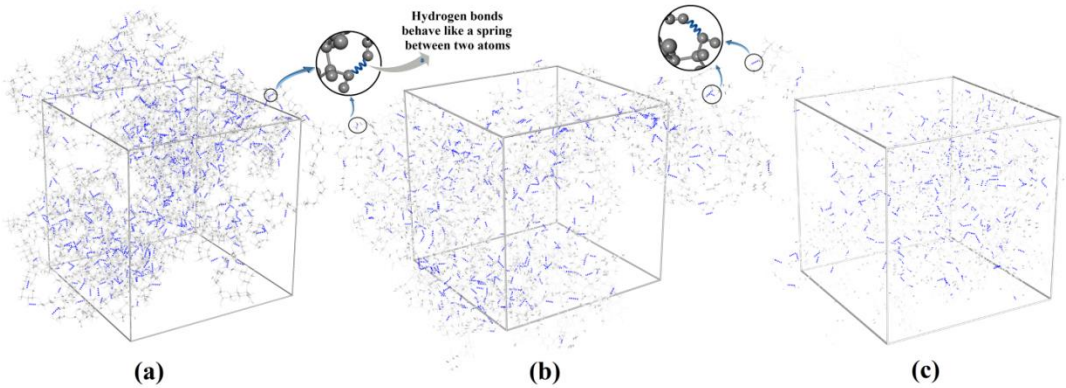

Figure 31. Hydrogen bond distribution in a) hemicellulose b) LCC c) lignin.

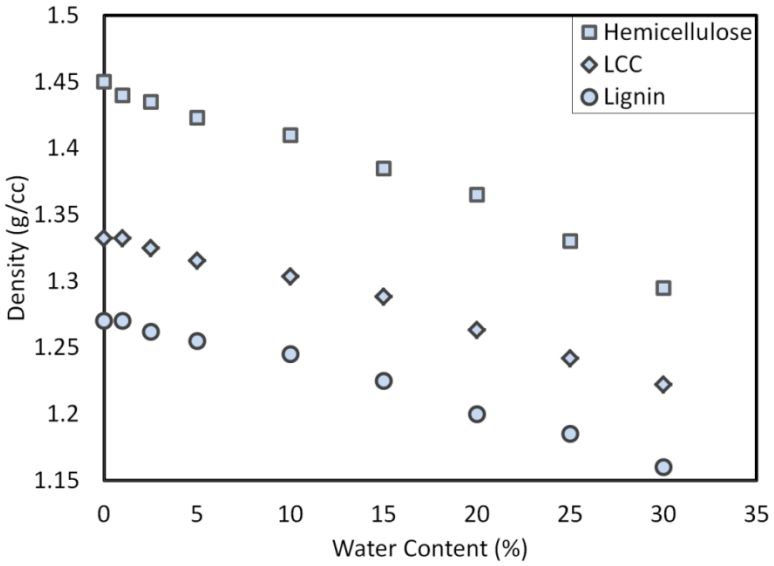

Figure 32. The variation of density with water content.

Figure 32 elucidates the different density responses of hemicellulose, lignin and LCC to the variation of water content. Hemicellulose with higher density than lignin and LCC exhibits more sensitivity to water molecules. Introducing a small amount of water into dry LCC and lignin does not change their densities significantly whereas hemicellulose density varies notably. As the water molecules continue permeating into these carbohydrates, their densities decrease almost linearly. Hemicellulose with larger number of hydroxyl groups has more reaction sites for water molecules. Therefore, the hydrogen bond of hemicellulose constantly decreases as water molecules break the hydrogen bond between them. Lignin, however, has less bonding sites compare with hemicellulose. Hence, after a certain amount of water content, the regressive effect of water on hydrogen bond diminishes.

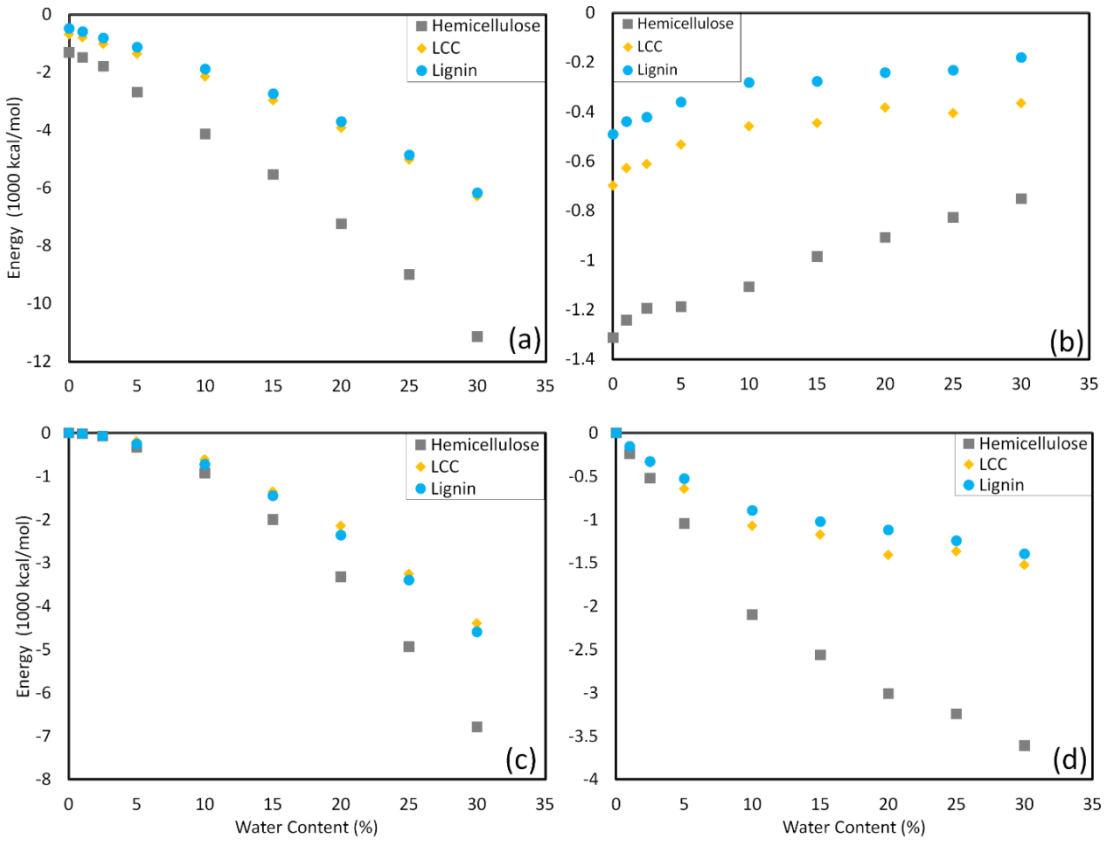

Figure 33. Hydrogen bond energies a) Total b) polymers c) water d) interaction between polymers and water.

The intermolecular energies between particles in a material play an important role in determining its molecular structure which dictates the physical properties such as density and elastic modulus. Since hydrogen bond interactions are both short range and angle-dependent, their impacts on structuring of polymers with Hbonds are significant. In carbohydrates, due to their high number of hydroxyl groups, the consequences of hydrogen bond energies are amplified, especially when interacting with water molecules. The study of variation of hydrogen bonds with water content allows us to capture the important physics of water-polymer interactions with a minimal need for experimental inputs. Hence, we start with investigating the total hydrogen bond energies of hemicellulose, LCC and lignin in different water content (Figure 33a). All three materials

exhibit almost the same progressive trend of total hydrogen bond energies when the water content increases. Nevertheless, hemicellulose shows higher total hydrogen bond energy than LCC and lignin, in the dry and hydrated conditions due to its larger number of hydroxyl groups. The coincidence of LCC and lignin hydrogen bond energies indicates that LCC may adopt lignin physical behavior imposed by hydrogen bonds.

In an effort to investigate the conformational change of the hemicellulose, LCC and lignin with increasing water content, the hydrogen bond energies between merely polymer chains were calculated and shown in Figure 33b. The diminution of hydrogen bond energies on this graph is an indication of hydrogen bond rupture by water molecules. At low water content (less than 10%) reduction of hydrogen bonds of lignin is more pronounced. At high water content, however, the graph goes to almost a plateau. We found out that these two distinct stages occur due to the formation of hydrogen bonds with new water molecules at low water content and the gap between polymer chains caused by water molecule aggregation. To explain these two stages accurately, the hydrogen bond energy between only water molecules were calculated and presented in Figure 33c. This graph shows that after 10% water content the growth of hydrogen bond energies between water molecules increases significantly. This suggests that water molecules tend to create hydrogen bond with other water molecules and aggregate at high water content. Figure 33d presents the hydrogen bond interactions between polymer chains and water molecules. The salient growing trend of this graph below 10% water content shows that the water molecules tend to form hydrogen bonds with polymer chains at low water content.

Therefore, at lower concentrations of water, the hydrogen bonds between polymer matrices and water molecules seem to be more favorable than water-water hydrogen bonding. At higher water content, however, water molecules tend to make hydrogen bond with other water molecules and thus the formation of nano-droplets of water inside the LCC matrix occurs. This process, however, is not the same for all three materials. Unlike lignin and LCC, hemicellulose with higher number of hydroxyl groups continues the formation of hydrogen bonds with water molecules even at higher water content.

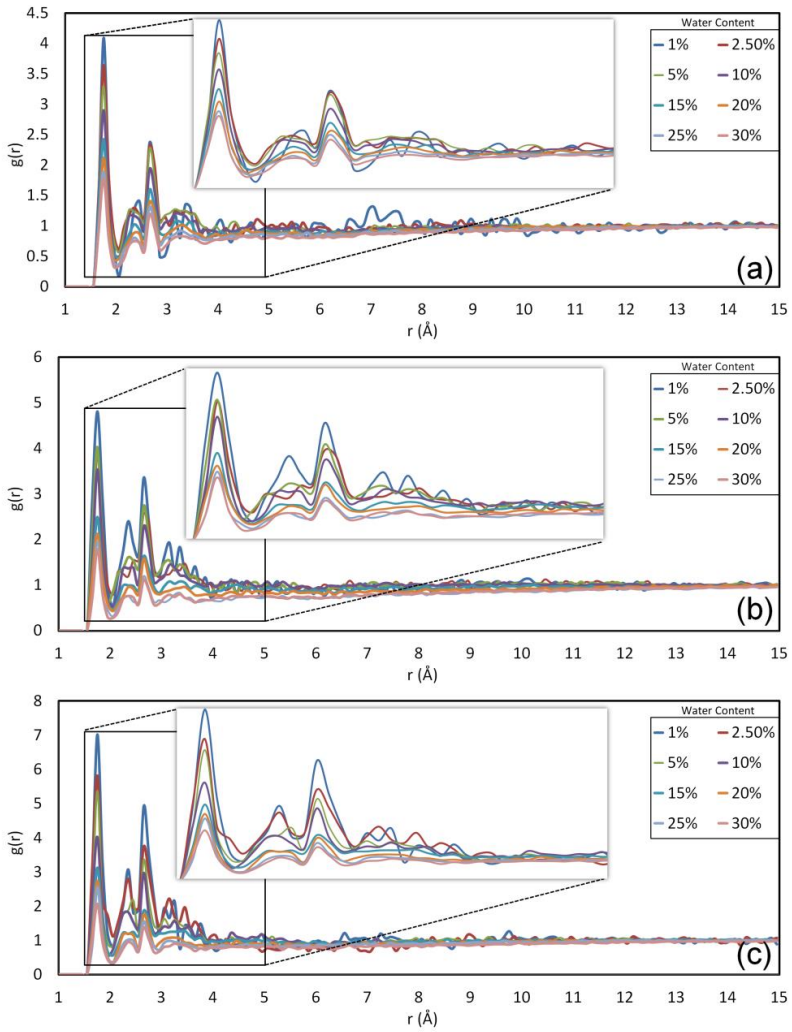

Figure 34. Radial distribution function between water molecules and hydroxyl group of a) Hemicellulose b) LCC c) Lignin

In order to analyze the evolution of hydrogen bond characteristics with increasing water molecules, Radial Distribution Functions (RDFs) between water molecules and hydroxyl groups of hemicellulose, LCC and lignin were calculated (Figure 34). RDF is a structural characterization parameter of amorphous molecules that provides the basic information about short range order and the nature of atomic interactions. RDF gives the possibility of finding a particle at a certain distance from the reference particle. The observed variations in dihedral conformation and internal structural variables are the results of the dynamics of non-bonded interactions like hydrogen bonding, electrostatic and van der Waal interactions. The first three distinct peaks on figure 4 are consequences of hydrogen bonding. The highest peak appearing at 1.75Å is associated with the donor – acceptor distance of hydrogen bonds. This shows a short-range strong Hbond between water molecules and polymer chains. The second peak at 2.45Å appears due to distance between donor and hydrogen on the acceptor side. The third peak at 2.65Å represents the distance between water molecule oxygen and the oxygen on the hydroxyl groups. The next successive peaks are indications of long-range electrostatic interactions between water molecules and hydroxyl groups. The diminution in intensity of the peaks with increasing water content confirms that the fraction of water molecules involved in the hydrogen bonding with all three polymer matrices decreases as the water content increases. Nonetheless, unlike the constant reduction in the intensity of the peaks on hemicellulose RDF diagram, lignin peaks drops suddenly after 10% water content which suggests a saturation situation for lignin. LCC also follows the lignin behavior.

The other difference between lignin and hemicellulose response to water molecules is the height of the peaks. The higher peaks on lignin diagram indicate higher probability of

finding the water molecules around the reaction site on lignin chains than that of hemicellulose. Therefore, lignin tends to interact with a larger fraction of introduced water molecules than hemicellulose. This is due to the position of functional groups adjacent to the hydroxyl groups. The lignin hydroxyl groups are mostly parts of well-spread hydroxymethyl groups that are extended out from the main chains. The hemicellulose hydroxyl groups, however, are parts of xylose groups, where two hydroxyl groups attach directly to the main chains and are localized on pyranose rings. Lignin hydroxyl groups are more exposed to and more accessible by water molecules than those of hemicellulose hydroxyl groups. Hence, although the hemicellulose structure contains more hydroxyl groups, lignin hydroxyl groups are more efficient in making hydrogen bonds.

6 Summary and Conclusion

With the increasing applications of the composite materials in biotechnology, a microscopic understanding of the mechanisms of molecular interactions and adhesion between layers of biomaterials has become of importance. Strong adhesion between layers of biomaterials plays a significant role in providing high toughness and strength in the biomedical devices. Having high strength-to-weight ratio that would warranty the ability of the composite to withstand physiological loadings without exhibiting brittle fractures is an imperative key factor in designing medical devices such as drug delivery and synthetic orthopedic materials.

In our preliminary study on the drug eluting stents, we used molecular dynamics simulations along with the combination of Atomic Force Microscopy (AFM) experiments and contact mechanics theories to predict the adhesion between layers of the drug eluting stent after being implanted inside the body. Simulation of the diffusion of water molecules between drug eluting stent layers at the body temperature suggests that the effects of water and temperature on the adhesion between parylene C and 316L are regressive. We observed the similar effect of water and temperature on the system in the presence of silane. The source of this diminution found to be the van der Waals energies between parylene C and 316L, while no significant change in electrostatic energies are observed. We used the same techniques to study the modified hydrogel-hydroxyapatite bone substitute material. Our results showed that substitution of the hydroxylated side chain of poly (2- hydroxyethyl methacrylate) (pHEMA) with carboxylate side chains to make poly (glycerol methacrylate) (pGLYMA), improves the mechanical properties of the composite material. Both experimental and numerical results showed that pGLYMA has a stronger adhesion forces with hydroxyapatite and may be used for preparing high-

affinity polymer-HA composite. Further studies showed that the higher interaction between pGLYMA and HA is due to higher electrostatic energies between these materials. This is likely derived from the main difference in molecular structures between pHEMA and pGLYMA, which is the uncharged side chain hydroxyl end groups for pHEMA and the negatively charged side chain carboxylate end groups for pGLYMA.

In the main part of this research, in an effort to develop a bio-inspired material-by-design approach for cellulose-based composites with tailored interfaces and programmed microstructures that could provide an outstanding strength-to-weight ratio, we studied the nanostructure and nanomechanics of the bamboo fiber, a cellulose-based biocomposite material designed by nature with remarkable strength-to-weight ratio (higher than steel and concrete). We have utilized atomistic simulations to investigate the mechanical properties and mechanisms of interactions between cellulose nanofibrils and the bamboo fiber matrix which is an intertwined hemicellulose with lignin called lignin-carbohydrate complex (LCC). Our results suggest that the molecular origin of the rigidity of bamboo fibers comes from the crystal structures of cellulose nanofibrils that lead the external loads to covalent bonds in the main chain of cellulose. In the matrix of bamboo fiber, hemicellulose exhibits larger elastic modulus than lignin whereas lignin shows greater tendency to adhere to cellulose nanofibrils. Consequently, the role of hemicellulose found to be enhancing the transverse rigidity of the matrix and lignin found to be providing the strength of bamboo fibers. The abundance of hydrogen bonds in hemicellulose chains is responsible for improving the elastic modulus of LCC. The strong van der Waals forces between lignin molecules and cellulose nanofibrils are responsible for higher adhesion energy between LCC and cellulose nanofibrils. We also found out that the amorphous

regions of cellulose nanofibrils is the weakest interface in bamboo microfibrils. In presence of water, the elastic modulus of lignin increases at low water content (less than 10%) and decreases in higher water content, whereas the hemicellulose elastic modulus constantly decreases. The variations of Radial Distribution Function and water diffusion of these materials with water content suggest that water molecules enhance the mechanical properties of lignin by filling voids in the system and creating hydrogen bond bridges between polymer chains. For hemicellulose, however, the effect is always regressive due to the destructive effect of water molecules on the hydrogen bond in hemicellulose dense structure. Therefore, the porous structure of lignin supports the matrix to have higher rigidity in the presence of water molecules. These results that elucidate the functionalities and interactions of the main constituents of bamboo fibers could be utilized for designing artificial cellulose-based composite materials.

6.1 Implication

Many cellulose-based nanocomposite polymers have the same structure as the bamboo fiber. In these materials, there is a crosslinked structure of two polymers which forms the matrix reinforced by cellulose nanocrystals. For instance, poly (vinyl alcohol) (PVOH) is crosslinked with poly (acrylic acid) (PAA) to form the matrix for cellulose nanocrystals [139]. These types of polymers can benefit from the information obtained from bamboo fiber. We suggest that the polymer and the crosslinker should have the ability to create hydrogen bonds through their hydroxyl groups. The polymer should provide higher number of hydrogen bond than the crosslinker, and enhance the rigidity for the matrix through the strong hydrogen bond network around the cellulose nanocrystals. This functionality can improve the elastic modulus of the system by enhancing the transverse

rigidity around the cellulose nanocrystals. The crosslinker in the matrix should provide larger adhesion forces between the matrix and cellulose nanocrystals than the polymer, by means of strong van der Waals forces. In order to control the rigidity of the whole system in the presence of water molecules, the density of the crosslinker should be controlled. Because the porous structure of the crosslinker allows water molecules to fill in the free spaces between chains and creates a hydrogen bond bridge between them. This process enhances the rigidity of the system up to the point of saturation.

References

[1] Ramos, Marta MD. "Theoretical study of metal–polyimide interfacial properties." Vacuum 64, no. 3 (2002): 255-260.

[2] Zong, Zong, Yifang Cao, Nima Rahbar, and Wole Soboyejo. "Nano-and microscale adhesion energy measurement for Au–Au contacts in microswitch structures." Journal of applied physics 100, no. 10 (2006): 104313.

[3] Kim, Changsoon, Yifang Cao, Winston O. Soboyejo, and Stephen R. Forrest. "Patterning of active organic materials by direct transfer for organic electronic devices." Journal of applied physics 97, no. 11 (2005): 113512.

[4] Ke, Lin, Ramadas Senthil Kumar, Keran Zhang, Soo Jin Chua, and A. T. S. Wee. "Organic light emitting devices performance improvement by inserting thin parylene layer." Synthetic metals 140, no. 2 (2004): 295-299.

[5] Ke, Lin, Ramadas Senthil Kumar, Keran Zhang, Soo-Jin Chua, and A. T. S. Wee. "Effect of parylene layer on the performance of OLED." Microelectronics journal 35, no. 4 (2004): 325-328.

[6] Wolf, Kurt V., Zong Zong, Juan Meng, Argjenta Orana, Nima Rahbar, Karin M. Balss, George Papandreou, Cynthia A. Maryanoff, and Wole Soboyejo. "An investigation of adhesion in drug-eluting stent layers." Journal of Biomedical Materials Research Part A 87, no. 1 (2008): 272-281.

[7] Kajzer, W., A. Krauze, W. Walke, and J. Marciniak. "Corrosion behaviour of AISI 316L steel in artificial body fluids." Journal of Achievements in materials and manufacturing engineering 31, no. 2 (2008): 247-253.

[8] Mai, Fu-Der, Bo-Jung Chen, Li-Chen Wu, Feng-Yin Li, and Wen-Kang Chen. "Imaging of single liver tumor cells intoxicated by heavy metals using ToF-SIMS." Applied surface science 252, no. 19 (2006): 6809-6812.

[9] Sun, H., P. Ren, and J. R. Fried. "The COMPASS force field: parameterization and validation for phosphazenes." Computational and Theoretical Polymer Science 8, no. 1 (1998): 229-246.

[10] Bazooyar, Faranak, Frank A. Momany, and Kim Bolton. "Validating empirical force fields for molecular-level simulation of cellulose dissolution." Computational and Theoretical Chemistry 984 (2012): 119-127.

[11] Tanaka, Fumio, and Tadahisa Iwata. "Estimation of the elastic modulus of cellulose crystal by molecular mechanics simulation." Cellulose 13, no. 5 (2006): 509-517.

[12] Eichhorn, Stephen J., Robert J. Young, and Geoffrey R. Davies. "Modeling crystal and molecular deformation in regenerated cellulose fibers." Biomacromolecules 6, no. 1 (2005): 507-513.

[13] Mazeau, K., and L. Heux. "Molecular dynamics simulations of bulk native crystalline and amorphous structures of cellulose." The Journal of Physical Chemistry B 107, no. 10 (2003): 2394-2403.

[14] Hansen, Jean-Pierre, and Ian R. McDonald. Theory of simple liquids. Elsevier, 1990.

[15] Hossain, D., M. A. Tschopp, D. K. Ward, J. L. Bouvard, P. Wang, and M. F. Horstemeyer. "Molecular dynamics simulations of deformation mechanisms of amorphous polyethylene." Polymer 51, no. 25 (2010): 6071-6083.

[16] Capaldi, Franco M., Mary C. Boyce, and Gregory C. Rutledge. "Molecular response of a glassy polymer to active deformation." Polymer 45, no. 4 (2004): 1391-1399.

[17] Packham, D. E. "Work of adhesion: contact angles and contact mechanics." International journal of adhesion and adhesives 16, no. 2 (1996): 121-128.

[18] Packham, David E. "Surface energy, surface topography and adhesion." International Journal of Adhesion and Adhesives 23, no. 6 (2003): 437-448.

[19] Rahbar, Nima, Kurt Wolf, Argjenta Orana, Roy Fennimore, Zong Zong, Juan Meng, George Papandreou, Cynthia Maryanoff, and Wole Soboyejo. "Adhesion and interfacial fracture toughness between hard and soft materials." Journal of Applied Physics 104, no. 10 (2008): 103533.

[20] Hertz, Heinrich. "Über die Berührung fester elastischer Körper." (1882): 156-171.

[21] Johnson, K. L., K. Kendall, and A. D. Roberts. "Surface energy and the contact of elastic solids." In Proceedings of the Royal Society of London A: Mathematical, Physical and Engineering Sciences, vol. 324, no. 1558, pp. 301-313. The Royal Society, 1971.

[22] Derjaguin, Boris V., Vladimir M. Muller, and Yu P. Toporov. "Effect of contact deformations on the adhesion of particles." Journal of Colloid and interface science 53, no. 2 (1975): 314-326.

[23] Tabor, D. "Surface forces and surface interactions." Journal of colloid and interface science 58, no. 1 (1977): 2-13.

[24] Carpick, Robert W., D. Frank Ogletree, and Miquel Salmeron. "A general equation for fitting contact area and friction vs load measurements." Journal of Colloid and Interface Science 211, no. 2 (1999): 395-400.

[25] Maugis, Daniel. "Adhesion of spheres: the JKR-DMT transition using a Dugdale model." Journal of colloid and interface science 150, no. 1 (1992): 243-269.

[26] Pietrement, O., and M. Troyon. "General equations describing elastic indentation depth and normal contact stiffness versus load." Journal of colloid and interface science 226, no. 1 (2000): 166-171.

[27] Muller, V. M., V. S. Yushchenko, and B. V. Derjaguin. "On the influence of molecular forces on the deformation of an elastic sphere and its sticking to a rigid plane." Journal of Colloid and Interface Science 77, no. 1 (1980): 91-101.

[28] Mittal, Kashmiri Lal, ed. Adhesion measurement of films and coatings. Vol. 640. VSP, 1995.

[29] Scurlock, J. M. O., D. C. Dayton, and B. Hames. "Bamboo: an overlooked biomass resource?." Biomass and bioenergy 19, no. 4 (2000): 229-244.

[30] Chung, K. F., W. K. Yu, and S. L. Chan. "Mechanical properties and engineering data of structural bamboo." In Proceedings of International Seminar 'Bamboo Scaffolds in Building Construction'. 2002.

[31] Amada, Shigeyasu, and Sun Untao. "Fracture properties of bamboo." Composites Part B: Engineering 32, no. 5 (2001): 451-459.

[32] Habibi, Meisam K., and Yang Lu. "Crack Propagation in Bamboo's Hierarchical Cellular Structure." Scientific reports 4 (2014).

[33] Chang, Shang-Tzen, Sheng-Yang Wang, and Jyh-Horng Wu. "Rapid extraction of epidermis chlorophyll of moso bamboo (Phyllostachys pubescens) culm using ultrasonics." Journal of wood science 44, no. 1 (1998): 78-80.

[34] Chung, Min-Jay, Sen-Sung Cheng, Chia-Ju Lee, and Shang-Tzen Chang. "Novel methods for dyeing the epidermis of bamboo culms and their colour fastness." Coloration Technology 130, no. 2 (2014): 112-119.

[35] He, Xin-Qiang, Kiyoshi Suzuki, Shinichi Kitamura, Jin-Xing Lin, Ke-Ming Cui, and Takao Itoh. "Toward understanding the different function of two types of parenchyma cells in bamboo culms." Plant and cell physiology 43, no. 2 (2002): 186-195.

[36] Amada, Shigeyasu, Yoshinobu Ichikawa, Tamotsu Munekata, Yukito Nagase, and Hiroyuki Shimizu. "Fiber texture and mechanical graded structure of bamboo." Composites Part B: Engineering 28, no. 1 (1997): 13-20.

[37] Wang, Xiaoqing, Haiqing Ren, Bo Zhang, Benhua Fei, and Ingo Burgert. "Cell wall structure and formation of maturing fibres of moso bamboo (Phyllostachys pubescens) increase buckling resistance." Journal of The Royal Society Interface (2011): rsif20110462.

[38] Wang, Shu-Guang, Shu-Yan Lin, Xiao-Lan Pu, Yu-Long Ding, and Xian-Chong Wan. "Developmental changes in cell wall of bundle sheath fibers close to phloem of Fargesia yunnanensis." Botanical Studies 53, no. 3 (2012): 353-362.

[39] Gritsch, Cristina Sanchis, and Richard J. Murphy. "Ultrastructure of fibre and parenchyma cell walls during early stages of culm development in Dendrocalamus asper." Annals of botany 95, no. 4 (2005): 619-629.

[40] Ma, Jian-feng, Wu-yi Chen, Ling Zhao, and Da-hai Zhao. "Elastic buckling of bionic cylindrical shells based on bamboo." Journal of Bionic Engineering 5, no. 3 (2008): 231-238.

[41] Amada, Shigeyasu, Yoshinobu Ichikawa, Tamotsu Munekata, Yukito Nagase, and Hiroyuki Shimizu. "Fiber texture and mechanical graded structure of bamboo." Composites Part B: Engineering 28, no. 1 (1997): 13-20.

[42] Amada, Shigeyasu, Yoshinobu Ichikawa, Tamotsu Munekata, Yukito Nagase, and Hiroyuki Shimizu. "Fiber texture and mechanical graded structure of bamboo." Composites Part B: Engineering 28, no. 1 (1997): 13-20.

[43] Dixon, Patrick G., and Lorna J. Gibson. "The structure and mechanics of Moso bamboo material." Journal of The Royal Society Interface 11, no. 99 (2014): 20140321.

[44] Tan, T., N. Rahbar, S. M. Allameh, S. Kwofie, D. Dissmore, K. Ghavami, and W. O. Soboyejo. "Mechanical properties of functionally graded hierarchical bamboo structures." Acta biomaterialia 7, no. 10 (2011): 3796-3803.

[45] Habibi, Meisam K., Arash T. Samaei, Behnam Gheshlaghi, Jian Lu, and Yang Lu. "Asymmetric flexural behavior from bamboo's functionally graded hierarchical structure: Underlying mechanisms." Acta biomaterialia 16 (2015): 178-186.

[46] Keogh, Lauren, Patrick O'Hanlon, Peter O'Reilly, and David Taylor. "Fatigue in bamboo." International Journal of Fatigue 75 (2015): 51-56.

[47] Amada, Shigeyasu, and Sun Untao. "Fracture properties of bamboo." Composites Part B: Engineering 32, no. 5 (2001): 451-459.

[48] Habibi, Meisam K., and Yang Lu. "Crack Propagation in Bamboo's Hierarchical Cellular Structure." Scientific reports 4 (2014).

[49] Osorio, Lina, E. Trujillo, A. W. Van Vuure, and I. Verpoest. "Morphological aspects and mechanical properties of single bamboo fibres and flexural characterization of bamboo/epoxy composites." Journal of reinforced plastics and composites (2011): 0731684410397683.

[50] Rao, K. Murali Mohan, and K. Mohana Rao. "Extraction and tensile properties of natural fibers: Vakka, date and bamboo." Composite structures 77, no. 3 (2007): 288-295.

[51] Phong, Nguyen Tien, Toru Fujii, Bui Chuong, and Kazuya Okubo. "Study on how to effectively extract bamboo fibers from raw bamboo and wastewater treatment." Journal of Materials Science Research 1, no. 1 (2011): p144.

[52] Khalil, HPS Abdul, I. U. H. Bhat, M. Jawaid, A. Zaidon, D. Hermawan, and Y. S. Hadi. "Bamboo fibre reinforced biocomposites: A review." Materials & Design 42 (2012): 353-368.

[53] Li, Long-Jiao, Yue-Ping Wang, Ge Wang, Hai-Tao Cheng, and Xiao-Jun Han. "Evaluation of properties of natural bamboo fiber for application in summer textiles." Journal of Fiber Bioengineering and Informatics 3, no. 2 (2010): 94-99.

[54] Yueping, Wang, Wang Ge, Cheng Haitao, Tian Genlin, Liu Zheng, Xiao QunFeng, Zhou Xiangqi, Han Xiaojun, and Gao Xushan. "Structures of natural bamboo fiber for textiles." Textile research journal (2009).

[55] Wegst, Ulrike GK, Hao Bai, Eduardo Saiz, Antoni P. Tomsia, and Robert O. Ritchie. "Bioinspired structural materials." Nature materials (2014).

[56] Jain, Seema, Rakesh Kumar, and U. C. Jindal. "Mechanical behaviour of bamboo and bamboo composite." Journal of Materials Science 27, no. 17 (1992): 4598-4604.

[57] Li, Long-Jiao, Yue-Ping Wang, Ge Wang, Hai-Tao Cheng, and Xiao-Jun Han. "Evaluation of properties of natural bamboo fiber for application in summer textiles." Journal of Fiber Bioengineering and Informatics 3, no. 2 (2010): 94-99.

[58] Wang, Xiaoqing, Haiqing Ren, Bo Zhang, Benhua Fei, and Ingo Burgert. "Cell wall structure and formation of maturing fibres of moso bamboo (Phyllostachys pubescens) increase buckling resistance." Journal of The Royal Society Interface (2011): rsif20110462.

[59] Lybeer, Bieke, and Gerald Koch. "A Topocuemical and Semiquantitative Study of The Lignification During Ageing of Bamboo Culms (Phyllostachys Viridiglaucescens)." IAWA Journal 26, no. 1 (2005): 99-110.

[60] Donaldson, Lloyd A. "Lignification and lignin topochemistry—an ultrastructural view." Phytochemistry 57, no. 6 (2001): 859-873.

[61] Gindl, W., H. S. Gupta, T. Schöberl, H. C. Lichtenegger, and P. Fratzl. "Mechanical properties of spruce wood cell walls by nanoindentation." Applied Physics A 79, no. 8 (2004): 2069-2073.

[62] Gindl, W., H. S. Gupta, and C. Grünwald. "Lignification of spruce tracheid secondary cell walls related to longitudinal hardness and modulus of elasticity using nano-indentation." Canadian Journal of Botany 80, no. 10 (2002): 1029-1033.

[63] Yu, Yan, Zehui Jiang, Benhua Fei, Ge Wang, and Hankun Wang. "An improved microtensile technique for mechanical characterization of short plant fibers: a case study on bamboo fibers." Journal of Materials Science 46, no. 3 (2011): 739-746.

[64] Okubo, Kazuya, Toru Fujii, and Yuzo Yamamoto. "Development of bamboo-based polymer composites and their mechanical properties." Composites Part A: Applied science and manufacturing 35, no. 3 (2004): 377-383.

[65] Khalil, HPS Abdul, I. U. H. Bhat, M. Jawaid, A. Zaidon, D. Hermawan, and Y. S. Hadi. "Bamboo fibre reinforced biocomposites: A review." Materials & Design 42 (2012): 353-368.

[66] Lybeer, Bieke, and Gerald Koch. "Lignin distribution in the tropical bamboo species Gigantochloa levis." IAWA Journal 26, no. 4 (2005): 443-456.

[67] Gibson, Lorna J. "The hierarchical structure and mechanics of plant materials." Journal of the Royal Society Interface (2012): rsif20120341.

[68] Ciesielski, Peter N., James F. Matthews, Melvin P. Tucker, Gregg T. Beckham, Michael F. Crowley, Michael E. Himmel, and Bryon S. Donohoe. "3D electron tomography of pretreated biomass informs atomic modeling of cellulose microfibrils." ACS nano 7, no. 9 (2013): 8011-8019.

[69] Fernandes, Anwesha N., Lynne H. Thomas, Clemens M. Altaner, Philip Callow, V. Trevor Forsyth, David C. Apperley, Craig J. Kennedy, and Michael C. Jarvis. "Nanostructure of cellulose microfibrils in spruce wood." Proceedings of the National Academy of Sciences 108, no. 47 (2011): E1195-E1203.

[70] Kulasinski, Karol, Sinan Keten, Sergey V. Churakov, Robert Guyer, Jan Carmeliet, and Dominique Derome. "Molecular Mechanism of Moisture-Induced Transition in Amorphous Cellulose." ACS Macro Letters 3, no. 10 (2014): 1037-1040.

[71] Acharya, Ghanashyam, and Kinam Park. "Mechanisms of controlled drug release from drug-eluting stents." Advanced drug delivery reviews 58, no. 3 (2006): 387-401.

[72] Lewis, Gladius. "Materials, fluid dynamics, and solid mechanics aspects of coronary artery stents: A state-of-the-art review." Journal of Biomedical Materials Research Part B: Applied Biomaterials 86, no. 2 (2008): 569-590.

[73] Cieślik, Monika, Klas Engvall, Jinshan Pan, and Andrzej Kotarba. "Silane–parylene coating for improving corrosion resistance of stainless steel 316L implant material." Corrosion Science 53, no. 1 (2011): 296-301.

[74] Mani, Gopinath, Marc D. Feldman, Devang Patel, and C. Mauli Agrawal. "Coronary stents: a materials perspective." Biomaterials 28, no. 9 (2007): 1689-1710.

[75] Kajzer, W., A. Krauze, W. Walke, and J. Marciniak. "Corrosion behaviour of AISI 316L steel in artificial body fluids." Journal of Achievements in materials and manufacturing engineering 31, no. 2 (2008): 247-253.

[76] Kamińska, M., Okrój, W., Szymański, W., Jakubowski, Piotr Komorowski, A., Nosal, Hieronim Szymanowski et al. "Interaction of parylene C with biological objects." Acta of Bioengineering and Biomechanics 11, no. 3 (2009): 19-25.

[77] Udipi, Kishore, Mingfei Chen, Peiwen Cheng, Kevin Jiang, Diane Judd, Alejandra Caceres, Robert J. Melder, and Josiah N. Wilcox. "Development of a novel biocompatible polymer system for extended drug release in a next-generation drug-eluting stent." Journal of biomedical materials research Part A 85, no. 4 (2008): 1064-1071.

[78] Meng, Juan, Argjenta Orana, Ting Tan, Kurt Wolf, Nima Rahbar, Hannah Li, George Papandreou, Cynthia Maryanoff, and Wole Soboyejo. "Adhesion and interfacial fracture in drug-eluting stents." Journal of Materials Research 25, no. 04 (2010): 641-647.

[79] Fortin, Jeffrey B., and Toh-Ming Lu. Chemical vapor deposition polymerization: the growth and properties of parylene thin films. Springer Science & Business Media, 2003.

[80] Cieślik, Monika, Marcin Kot, Witold Reczyński, Klas Engvall, Wiesław Rakowski, and Andrzej Kotarba. "Parylene coatings on stainless steel 316L surface for medical applications—Mechanical and protective properties." Materials Science and Engineering: C 32, no. 1 (2012): 31-35.

[81] Tan, T., J. Meng, N. Rahbar, H. Li, G. Papandreou, C. A. Maryanoff, and W. O. Soboyejo. "Effects of silane on the interfacial fracture of a parylene film over a stainless steel substrate." Materials Science and Engineering: C 32, no. 3 (2012): 550-557.

[82] Kisin, Srdjan, Jelena Bozovic Vukic, Paul G. Th van der Varst, Gijsbertus de With, and Cor E. Koning. "Estimating the polymer-metal work of adhesion from molecular dynamics simulations." Chemistry of materials 19, no. 4 (2007): 903-907.

[83] Virtanen, S., P. Schmuki, and G. S. Frankel. "Critical Factors in Localized Corrosion IV." The Electrochemical Society, New Jersey (2003).

[84] Hendy, S. C. "Molecular dynamics simulations of oxide surfaces in water." Current Applied Physics 4, no. 2 (2004): 144-147.

[85] Sun, H., P. Ren, and J. R. Fried. "The COMPASS force field: parameterization and validation for phosphazenes." Computational and Theoretical Polymer Science 8, no. 1 (1998): 229-246.

[86] Rappe, A. K., K. S. Colwell, and C. J. Casewit. "Application of a universal force field to metal complexes." Inorganic Chemistry 32, no. 16 (1993): 3438-3450.

[87] Tan, Christine P., and Harold G. Craighead. "Surface engineering and patterning using parylene for biological applications." Materials 3, no. 3 (2010): 1803-1832.

[88] Hossain, D., M. A. Tschopp, D. K. Ward, J. L. Bouvard, P. Wang, and M. F. Horstemeyer. "Molecular dynamics simulations of deformation mechanisms of amorphous polyethylene." Polymer 51, no. 25 (2010): 6071-6083.

[89] Söderholm, K-JM, and S-W. Shang. "Molecular orientation of silane at the surface of colloidal silica." Journal of dental research 72, no. 6 (1993): 1050-1054.

[90] Kisin, Srdjan, Jelena Bozovic Vukic, Paul G. Th van der Varst, Gijsbertus de With, and Cor E. Koning. "Estimating the polymer-metal work of adhesion from molecular dynamics simulations." Chemistry of materials 19, no. 4 (2007): 903-907.

[91] Giovambattista, Nicolas, Pablo G. Debenedetti, and Peter J. Rossky. "Effect of surface polarity on water contact angle and interfacial hydration structure." The Journal of Physical Chemistry B 111, no. 32 (2007): 9581-9587.

[92] Selvarasah, S., S. H. Chao, C-L. Chen, S. Sridhar, A. Busnaina, A. Khademhosseini, and M. R. Dokmeci. "A reusable high aspect ratio parylene-C shadow mask technology for diverse micropatterning applications." Sensors and Actuators A: Physical 145 (2008): 306-315.

[93] Chang, Tracy Y., Vikramaditya G. Yadav, Sarah De Leo, Agustin Mohedas, Bimal Rajalingam, Chia-Ling Chen, Selvapraba Selvarasah, Mehmet R. Dokmeci, and Ali Khademhosseini. "Cell and protein compatibility of parylene-C surfaces." Langmuir 23, no. 23 (2007): 11718-11725.

[94] Song, Jie, Eduardo Saiz, and Carolyn R. Bertozzi. "A new approach to mineralization of biocompatible hydrogel scaffolds: an efficient process toward 3-dimensional bonelike composites." Journal of the American Chemical Society 125, no. 5 (2003): 1236-1243.

[95] Song, Jie, Eduardo Saiz, and Carolyn R. Bertozzi. "Preparation of pHEMA–CP composites with high interfacial adhesion via template-driven mineralization." Journal of the European Ceramic Society 23, no. 15 (2003): 2905-2919.

[96] Kaufman, Jessica D., Jie Song, and Catherine M. Klapperich. "Nanomechanical analysis of bone tissue engineering scaffolds." Journal of Biomedical Materials Research Part A 81, no. 3 (2007): 611-623.

[97] Song, Jie, Jianwen Xu, Tera Filion, Eduardo Saiz, Antoni P. Tomsia, Jane B. Lian, Gary S. Stein, David C. Ayers, and Carolyn R. Bertozzi. "Elastomeric high-mineral content hydrogel-hydroxyapatite composites for orthopedic applications." Journal of Biomedical Materials Research Part A 89, no. 4 (2009): 1098-1107.

[98] Chung, Woo-Jae, Ki-Young Kwon, Jie Song, and Seung-Wuk Lee. "Evolutionary screening of collagen-like peptides that nucleate hydroxyapatite crystals." Langmuir 27, no. 12 (2011): 7620-7628.

[99] Chung, Woo-Jae, Ki-Young Kwon, Jie Song, and Seung-Wuk Lee. "Evolutionary screening of collagen-like peptides that nucleate hydroxyapatite crystals." Langmuir 27, no. 12 (2011): 7620-7628.

[100] Skelly, Jordan D., Jeffrey Lange, Tera M. Filion, Xinning Li, David C. Ayers, and Jie Song. "Vancomycin-bearing Synthetic Bone Graft Delivers rhBMP-2 and Promotes Healing of Critical Rat Femoral Segmental Defects." Clinical Orthopaedics and Related Research® 472, no. 12 (2014): 4015-4023.

[101] Song, Jie, Viengkham Malathong, and Carolyn R. Bertozzi. "Mineralization of synthetic polymer scaffolds: a bottom-up approach for the development of artificial bone." Journal of the American Chemical Society 127, no. 10 (2005): 3366-3372.

[102] Hunter, Graeme K., and Harvey A. Goldberg. "Modulation of crystal formation by bone phosphoproteins: role of glutamic acid-rich sequences in the nucleation of hydroxyapatite by bone sialoprotein." Biochem. j 302 (1994): 175-179.

[103] George, Anne, Leslie Bannon, Boris Sabsay, Jerry W. Dillon, James Malone, Arthur Veis, Nancy A. Jenkins, Debra J. Gilbert, and Neal G. Copeland. "The carboxyl-terminal domain of phosphophoryn contains unique extended triplet amino acid repeat sequences forming ordered carboxyl-phosphate interaction ridges that may be essential in the biomineralization process." Journal of Biological Chemistry 271, no. 51 (1996): 32869-32873.

[104] Goldberg, Harvey A., Kevin J. Warner, Martin J. Stillman, and Graeme K. Hunter. "Determination of the hydroxyapatite-nucleating region of bone sialoprotein." Connective tissue research 35, no. 1-4 (1996): 385-392.

[105] Taş, A. Cüneyt. "Molten salt synthesis of calcium hydroxyapatite whiskers." Journal of the American Ceramic Society 84, no. 2 (2001): 295-300.

[106] Rahbar, Nima, Kurt Wolf, Argjenta Orana, Roy Fennimore, Zong Zong, Juan Meng, George Papandreou, Cynthia Maryanoff, and Wole Soboyejo. "Adhesion and interfacial fracture toughness between hard and soft materials." Journal of Applied Physics 104, no. 10 (2008): 103533.

[107] Youssefian, Sina, and Nima Rahbar. "Nano-scale adhesion in multilayered drug eluting stents." Journal of the mechanical behavior of biomedical materials 18 (2013): 1-11.

[108] Friedsam, Claudia, Aránzazu Del Campo Bécares, Ulrich Jonas, Hermann E. Gaub, and Markus Seitz. "Polymer Functionalized AFM tips for Long-Term Measurements in Single-Molecule Force Spectroscopy." ChemPhysChem 5, no. 3 (2004): 388-393.

[109] Kwon, Ki-Young, Eddie Wang, Alice Chung, Neil Chang, and Seung-Wuk Lee. "Effect of salinity on hydroxyapatite dissolution studied by atomic force microscopy." The Journal of Physical Chemistry C 113, no. 9 (2009): 3369-3372.

[110] Sun, H., P. Ren, and J. R. Fried. "The COMPASS force field: parameterization and validation for phosphazenes." Computational and Theoretical Polymer Science 8, no. 1 (1998): 229-246..

[111] Ren, F., E. D. Case, A. Morrison, M. Tafesse, and M. J. Baumann. "Resonant ultrasound spectroscopy measurement of Young's modulus, shear modulus and Poisson's ratio as a function of porosity for alumina and hydroxyapatite." Philosophical Magazine 89, no. 14 (2009): 1163-1182.

[112] Yongsheng, W. "Sol–gel derived hydroxyapatite coatings on metallic implants: characterization, in vitro and in vivo analysis." Biol Biomed Coat 1 (2011): 1-33.

[113] Ou, Keng-Liang, Ren-Jei Chung, Fu-Yi Tsai, Pei-Yu Liang, Shih-Wei Huang, and Shou-Yi Chang. "Effect of collagen on the mechanical properties of hydroxyapatite coatings." Journal of the mechanical behavior of biomedical materials 4, no. 4 (2011): 618-624.

[114] Fan, X., E. D. Case, and M. J. Baumann. "The effect of indentation-induced microcracks on the elastic modulus of hydroxyapatite." Journal of Materials Science 47, no. 17 (2012): 6333-6345.

[115] Qin, Zhao, Alfonso Gautieri, Arun K. Nair, Hadass Inbar, and Markus J. Buehler. "Thickness of hydroxyapatite nanocrystal controls mechanical properties of the collagen–hydroxyapatite interface." Langmuir 28, no. 4 (2012): 1982-1992.

[116] Chilkoti, Ashutosh, Gabriel P. Lopez, Buddy D. Ratner, Martin J. Hearn, and David Briggs. "Analysis of polymer surfaces by SIMS. 16. Investigation of surface crosslinking in polymer gels of 2-hydroxyethyl methacrylate." Macromolecules 26, no. 18 (1993): 4825-4832.

[117] Regis, Shawn, Sina Youssefian, Manisha Jassal, Matthew D. Phaneuf, Nima Rahbar, and Sankha Bhowmick. "Fibronectin adsorption on functionalized electrospun polycaprolactone scaffolds: Experimental and molecular dynamics studies." Journal of Biomedical Materials Research Part A 102, no. 6 (2014): 1697-1706.

[118] Bose, Ranjita K., and Kenneth KS Lau. "Mechanical properties of ultrahigh molecular weight PHEMA hydrogels synthesized using initiated chemical vapor deposition." Biomacromolecules 11, no. 8 (2010): 2116-2122.

[119] Sathitsuksanoh, Noppadon, Zhiguang Zhu, Tsung-Jen Ho, Ming-Der Bai, and Yi-Heng Percival Zhang. "Bamboo saccharification through cellulose solvent-based biomass pretreatment followed by enzymatic hydrolysis at ultra-low cellulase loadings." Bioresource Technology 101, no. 13 (2010): 4926-4929.

[120] Dixon, Patrick G., and Lorna J. Gibson. "The structure and mechanics of Moso bamboo material." Journal of The Royal Society Interface 11, no. 99 (2014): 20140321.

[121] Tan, T., N. Rahbar, S. M. Allameh, S. Kwofie, D. Dissmore, K. Ghavami, and W. O. Soboyejo. "Mechanical properties of functionally graded hierarchical bamboo structures." Acta biomaterialia 7, no. 10 (2011): 3796-3803.

[122] Habibi, Meisam K., and Yang Lu. "Crack Propagation in Bamboo's Hierarchical Cellular Structure." Scientific reports 4 (2014).

[123] Low, I. M., Z. Y. Che, and B. A. Latella. "Mapping the structure, composition and mechanical properties of bamboo." Journal of materials research 21, no. 08 (2006): 1969-1976.

[124] Zou, Linhua, Helena Jin, Wei-Yang Lu, and Xiaodong Li. "Nanoscale structural and mechanical characterization of the cell wall of bamboo fibers." Materials Science and Engineering: C 29, no. 4 (2009): 1375-1379.

[125] Wegst, Ulrike GK, Hao Bai, Eduardo Saiz, Antoni P. Tomsia, and Robert O. Ritchie. "Bioinspired structural materials." Nature materials (2014).

[126] Fernandes, Anwesha N., Lynne H. Thomas, Clemens M. Altaner, Philip Callow, V. Trevor Forsyth, David C. Apperley, Craig J. Kennedy, and Michael C. Jarvis. "Nanostructure of cellulose microfibrils in spruce wood." Proceedings of the National Academy of Sciences 108, no. 47 (2011): E1195-E1203.

[127] Moon, Robert J., Ashlie Martini, John Nairn, John Simonsen, and Jeff Youngblood. "Cellulose nanomaterials review: structure, properties and nanocomposites." Chemical Society Reviews 40, no. 7 (2011): 3941-3994.

[128] Lahiji, Roya R., Xin Xu, Ronald Reifenberger, Arvind Raman, Alan Rudie, and Robert J. Moon. "Atomic force microscopy characterization of cellulose nanocrystals." Langmuir 26, no. 6 (2010): 4480-4488.

[129] Iwamoto, Shinichiro, Weihua Kai, Akira Isogai, and Tadahisa Iwata. "Elastic modulus of single cellulose microfibrils from tunicate measured by atomic force microscopy." Biomacromolecules 10, no. 9 (2009): 2571-2576.

[130] Sinko, Robert, Shawn Mishra, Luis Ruiz, Nick Brandis, and Sinan Keten. "Dimensions of biological cellulose nanocrystals maximize fracture strength." ACS Macro Letters 3, no. 1 (2013): 64-69.

[131] Kulasinski, Karol, Sinan Keten, Sergey V. Churakov, Dominique Derome, and Jan Carmeliet. "A comparative molecular dynamics study of crystalline, paracrystalline and amorphous states of cellulose." Cellulose 21, no. 3 (2014): 1103-1116.

[132] Cousins, W. J. "Elastic modulus of lignin as related to moisture content." Wood science and technology 10, no. 1 (1976): 9-17.

[133] Cousins, W. J. "Young's modulus of hemicellulose as related to moisture content." Wood science and technology 12, no. 3 (1978): 161-167.

[134] Bergander, A., and L. Salmén. "Cell wall properties and their effects on the mechanical properties of fibers." Journal of Materials Science 37, no. 1 (2002): 151-156.

[135] Salmén, Lennart. "Micromechanical understanding of the cell-wall structure." Comptes rendus biologies 327, no. 9 (2004): 873-880.

[136] Dri, Fernando L., Louis G. Hector Jr, Robert J. Moon, and Pablo D. Zavattieri. "Anisotropy of the elastic properties of crystalline cellulose Iβ from first principles density functional theory with Van der Waals interactions." Cellulose 20, no. 6 (2013): 2703-2718.

[137] Chung, K. F., and W. K. Yu. "Mechanical properties of structural bamboo for bamboo scaffoldings." Engineering structures 24, no. 4 (2002): 429-442.

[138] Hatakeyama, Hyoe, and Tatsuko Hatakeyama. "Lignin structure, properties, and applications." In Biopolymers, pp. 1-63. Springer Berlin Heidelberg, 2010.

[139] Pakzad, A., J. Simonsen, and R. S. Yassar. "Elastic properties of thin poly (vinyl alcohol)–cellulose nanocrystal membranes." Nanotechnology 23, no. 8 (2012): 085706.

Appendix

Contact Behavior of Soft Spherical Tactile Sensors

INTRODUCT ION

The need for tactile sensing in robotics has become important because state-of-the-art robots are now capable of coming in contact and interact with the environment gently. This is more evident in the case of robotic manipulation, where tactile feedback provides information that is directly relevant to the task and cannot be easily obtained otherwise. For example, a robot can easily and robustly move its hand around an object, to grasp it, using tactile feedback to control the robot's motion and to learn from the object. This strategy does not requires knowledge of the exact position of object or its shape, which compared to approaches that need this information makes tactile based approaches more reliable and flexible. Nevertheless, the use of tactile feedback has been limited because the required sensing technology has not been available. There has been a large amount of work on designing tactile sensors, some technologies include: optical [1], [2], conductive elastomer [3], piezoresistive MEMS [4], [5], nanoparticle sensors [6] and carbon nanotube [7]–[10], and pillars embedded on polydimethylsiloxane (PDMS) [11]. A more complete survey of the technologies can be found in [12]. However, it is not clear that the data produced is useful because many of these technologies have not been tested in actual robots. Consequently, only did a few cases of robots guide by tactile feedback have been reported [13]–[16].

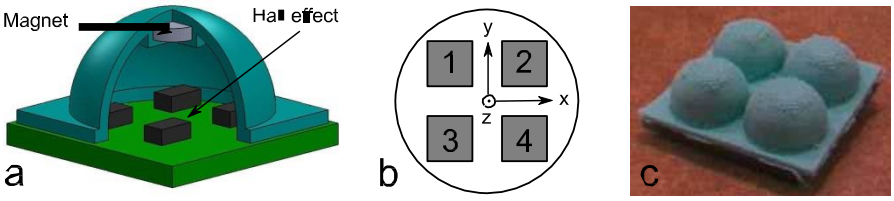

Figure 1. Compliant Tactile sensor. The force applied is estimated detecting the position of the tip of the dome. In this paper, we use magnets to detect the position of the tip [17]–[19]. (a) A magnet on the tip of the dome and a circuit board with 4 hall effect sensors allows the position estimation. (b) The position of the vector are estimated using the voltages from the hall-effect sensors. $x = f(V_1 + V_3 - V_2 - V_4)$, $y = f(V_1 + V_2 - V_3 - V_4)$, and $z = f(V_1 + V_2 + V_3 + V_4)$. The force is a function of the position of the tip [17]–[19]. (c) Array of 4 sensors using magnets.

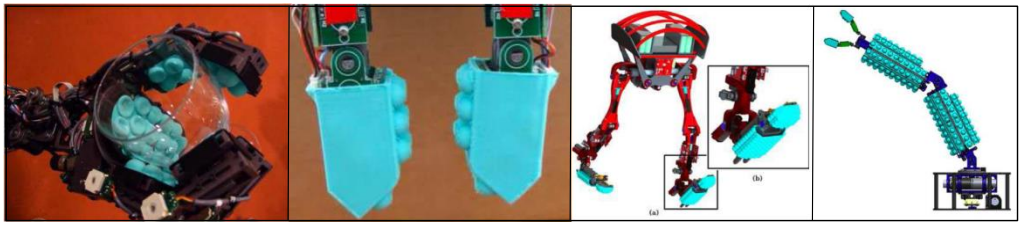

Figure 2. Sensitive Robotics platforms. Obrero, GoBot, Caminante, Tactile. All these robots are covered with the compliant tacitle sensors that enable their control software.

Sensitive manipulation [13] is a successful approach that demonstrates the effectiveness of approaching robotic manipulation using tactile sensing as the primary feedback [13], [14], [20]. This approach was enabled by the development of a compliant tactile sensor [17]–[19] that not only does detect the force applied (three dimensional vector) but also provides an appropriate physical interface to interact with objects; similarly to the skin in humans. These characteristics, that are crucial for robotics applications, were achieved by designing the sensor in the shape of a hollow hemisphere of silicone rubber combined with electronics components to estimate the dome's deformation when a force is applied (Fig. 1). In order to use these sensors in different applications some characteristics need to be modified (Fig. 2). For example, the sensor size to cover a smaller or larger area, or the sensor operational range to work on a robot's foot (sensitive walking [21]). In this paper,

we develop finite element models of the compliant tactile sensor to predict its behavior when its physical parameters are changed. These models, validated with experimental data, allow us to design sensors suited for a given application.

BACKGROUND

Bioinspired design studies biological structures, their func- tions, and their mechanisms in order to stimulate new solu- tions [22]–[24]. The bioinspired solution does not intend to exactly reproduce the original system. That is the case of that tactile sensor that we analyze [17], which was inspired by the functionality of the ridges on the human finger [25]–[27]. The structural functionality and the sensing mechanism of a ridge in the human skin is not fully understood and is still being studied [28]. However, it is accepted that the human skin com- prises of soft layers; namely the epidermis, and the dermis, and the subcutaneous tissue, which function as hyper-viscoelastic nonlinear materials [12], [29], [30] (See Fig. 3). The skin has ridges and a number of receptors. Two of them are the Meissner's corpuscles and Merkel's disks, which are located in and between the papillary ridges respectively. Meissner's corpuscles senses dynamic pressure and Merkel's disk detects static pressure. When forces are applied to the skin these ridges deform and the receptors estimate the applied forces [31]–[33]. From the previous description, two main ideas were taken to design the tactile sensor [17]: the compliant behavior of the skin, and the role of the ridges to detect applied forces.

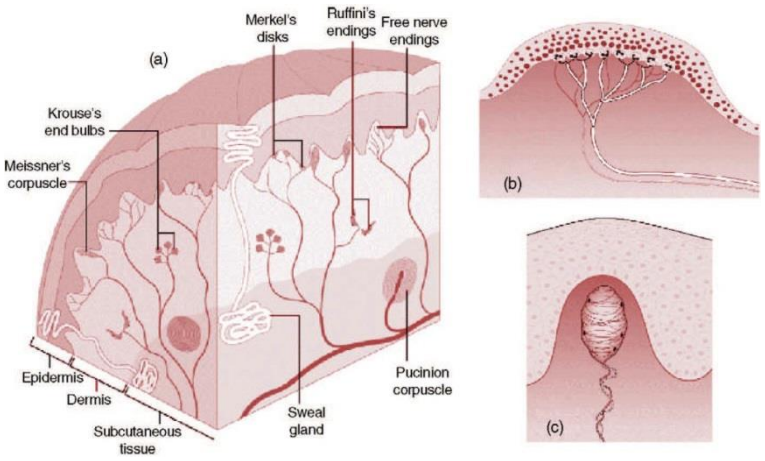

Figure 3. (a) Schematic view of human skin cross-section showing the location of various mechanoreceptors of the skin. (b) View of the Merkel that senses patterns and textures through spatial deformation and sustained pressure stimuli. (c) View of the Meissner that senses low frequency vibrations by temporal change in skin deformation. Both of them are located below epidermis under the papillary ridges where deformation of the ridges changes their conformations [34].

The sensor considered in this work tries to capture some of the characteristics considered necessary for robotics tasks. The sensor does not intend to emulate precisely the mechanisms and structures of the human skin. The characteristics relevant to this paper are the compliant behavior and the force sensitivity enabled by the material and the structure of the sensor.

The compliant behavior of the sensor is essential in providing high sensitivity because flexible materials with low elastic modulus are capable of providing significant and detectable deformations under small amount of forces. Not only does low modulus of elasticity increase the sensitivity but also promotes the contact between the sensor and touched objects, and enhances the ability of maintaining the contact even if the angle of contact changes. Because of the importance of this compliant behavior in human skin; experimental models of the fingertip elasticity have been developed [35].

The main role of the tactile sensor is to estimate the applied force. An effective sensor needs to estimate all the components of the force applied (normal and shear),

and respond independently of the shape of the object that comes in contact. These features are not common in available tactile sensors for robotics. These two requirements can be achieved by the sensor geometry. The geometry of the sensor to analyze is a hollow hemisphere that behaves as a ridge. This geometry is inspired in the human skin ridge but it does not intend to emulate its behavior fully. A basic advantage of ridges respect to flat bulk surfaces is its greater sensitivity to normal and lateral forces as explained in Appendix A. This fact has been exploited by several types of tactile sensors that use flexible, non-hollow, ridges of different geometries [11], [27]. However, hollow structures (shells) can also be used as a ridge whose rigidity is controlled by the ridge's geometry [36]. Among all different kinds of shell geometries, the spherical shell, used in the sensor analyzed in this paper [17]–[19], has a unique property. The initial contact between an object of arbitrary shape and a sphere is at a point. This small area of contact concentrates the stress deforming the shell, which makes the sensor highly sensitive to contact with arbitrary shapes. The relation between the force applied and the behavior of the sensor will be analyzed in Section III.

The behavior of a spherical shell when interacting with an object is not understood completely. Many researchers have studied the elastic contact of different bodies with a spherical object [37]–[39]. Hertz was the first to study the mechanics of contact between a full elastic sphere/ellipsoid with another full sphere of unequal diameter [37]. Using Hertz' solution and dimensional analysis, the elastic response of the contact between a full sphere and a flat plate has been characterized by Equation 1 [38].

$$F \approx \sqrt{R} E e^{\frac{3}{2}} \tag{1}$$

where, E is the modulus of elasticity, R is the radius of the sphere, e is the displacement of the pushing plane and F is the force applied by the plane. This equation shows that the rigidity of the spherical body increases (hardening) as the plane pushes downward. This behavior is valid for a spherical shell if the force applied by the plane is far less than critical force Fc defined in Equation 2.

$$F_c \approx \frac{Et^3}{R} \tag{2}$$

where t is the thickness of the shell. When F < Fc the elastic behavior of the spherical shell is not different from a full elastic sphere. However, for the force larger than Fc , Equation 1 is not valid because buckling occurs and shell forms a dimple (hollow inverted cap) due to increasing elastic energies in the area where the spherical shell touches the flat plate [38], [40]. Pogorelov considered a thin shell sphere subjected to a localized inward point load [39]. He showed that the rigidity of the spherical shell decreases as the point load pushes it downward. The displacement, e, of the point under the force F when the e > t, was calculated by,

$$F \approx \frac{Et^{\frac{5}{2}}}{R} e^{\frac{1}{2}} \tag{3}$$

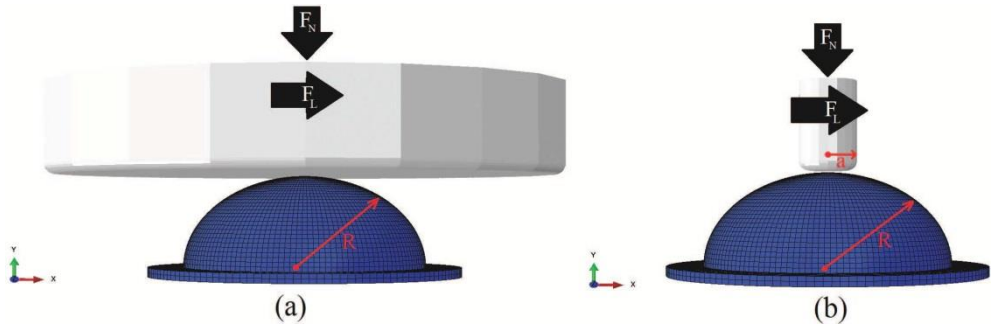

Figure 4. Finite element simulation strategy. Three spherical shells with the radii, *R*, of 4.5 *mm*, 7.0 *mm* and 9.5 *mm* are simulated. (a) Contact of a flat plate. (b) Contact of a cylinder *(a/R = 0.25)*. The normal force, F_N , is exerted by pushing vertically up to 60% of the spherical shell radius. The shear force, F_L , is exerted by moving the spherical shell horizontally up to 50% of its radius, after pushing 3.0 *mm* vertically.

However, the elastic response of a soft spherical shell is not fully understood, and it is not possible to completely analyze the contact with objects of different sizes. In this study we investigate the response of a sensor, made of a soft spherical shell, in scenarios that are to robotics applications. Based on the mechanical response of the shell the normal and shear forces applied are estimated. The assumptions for this study are stated in Section III.

MATERIALS AND METHODS

We develop finite element models of the compliant tactile sensor described in Section III-A. The models are validated with experimental data and used to design sensors with different characteristics. The sensor models and the actual tactile sensor are tested with two types of objects that represent the most common cases in robotics applications. One object has a small area of contact and represents elements such as points and edges. The other object has a large area of contact and represents surfaces with small curvature. The response to normal and shear forces is determined by moving the object with trajectories that are perpendicular and parallel to the base of the sensor.

Compliant Tactile Sensor

The compliant tactile sensor that we are studying consists of a spherical hemisphere shell (dome) made of silicon rubber [Fig. 1(c)]. The position of the top of the dome is tracked by using an embedded magnet and four Hall Effect sensors in the base of dome as shown in Fig. 1(a). The sensors are arranged in a 2 by 2 matrix with orthogonal axis [Fig. 1(b)]. The height of the magnet (axis z) is estimated by summing up the output of all the Hall Effect sensors. The displacements in the direction of the columns (axis y) and the rows (axis x) are measured by subtracting the rows and columns readings respectively. These

measurements are easily mapped to the actual positions of the magnet. The relation between the position of the dome's tip and the force applied is used to study the response of the sensor. Because the position of the magnet can be estimated in three dimensions, the sensor is capable of estimate normal and shear forces. A complete detail of this sensor is presented in [17]–[19].

Sensor Modeling

To study the behavior of the sensor, three-dimensional models of the dome with thickness of 0.5 mm and radii of 4.5 mm, 7 mm and 9.5 mm were implemented were implemented using ABAQUS [41] (Fig. 4). 8-node linear brick, reduced integration elements were used to mesh these models. This element showed better convergence performance for the geometry of the sensor. The bottom surface of the sensor is fixed in all directions as the boundary condition. In each case, the loads on the sensors were applied by two different objects: one was a small cylinder with a radius equal to 25% of the sensor radius, and the other was a flat circular disk with a radius of 10 mm, which is greater than all the radii (Fig. 4). Two types of load were exerted on the sensor; normal and shear. For the normal loads, each object pushes up to 60% of the sensor radius. For shear loads, first the object was pushed 3 mm downwards and then moved horizontally in about 50% of the radius of the sensor. Linear and nonlinear elastic finite element methods were used to model the mechanical behavior of the sensor. In the first model, the material used for the geometry was assumed to be isotropic, linear elastic with the modulus of elasticity, Poisson's ratio and a density of 1.5 MP a, 0.45 and 1100 kg/mm3, respectively. In the second model, the non- linear Ogden model, in which the strain energy density is expressed in terms of the principal stretches, λi , was used.

$$\Psi = \sum_{i=1}^{N} \frac{\mu_i}{\alpha_i} (\lambda_1^{\alpha_1} + \lambda_2^{\alpha_2} + \lambda_3^{\alpha_3}) \quad (4)$$

where, N, μ_i and α_i are material constants. According to [42] and [43] excellent convergence between theoretical and experimental results are achieved when N = 3 with the material parameters showing in Table I.

Experimental Validation

In order to validate the models described in Section III-B we use the experimental setup shown in Fig. 5. We started the experiments by vertically pushing the pole of a hemisphere silicone rubber (4.5*mm* radius and 0.5*mm* thickness) at the constant loading rate of 1*mm/min* to ensure process was under quasi-static conditions [Fig. 5(a)]. The forces were separately exerted by two cylindrical probes with radii of 1.2*mm* (25% of the sphere radius) and 10*mm*. The force-displacement results from the indentation were recorded using the 1 *N* load cell of an Instron machine. In order to measure the shear force, the two probes were glued to the pole of the specimens separately and after pushing 3*mm* vertically, they moved horizontally at the constant speed of 1*mm/min* [Fig. 5(b)].

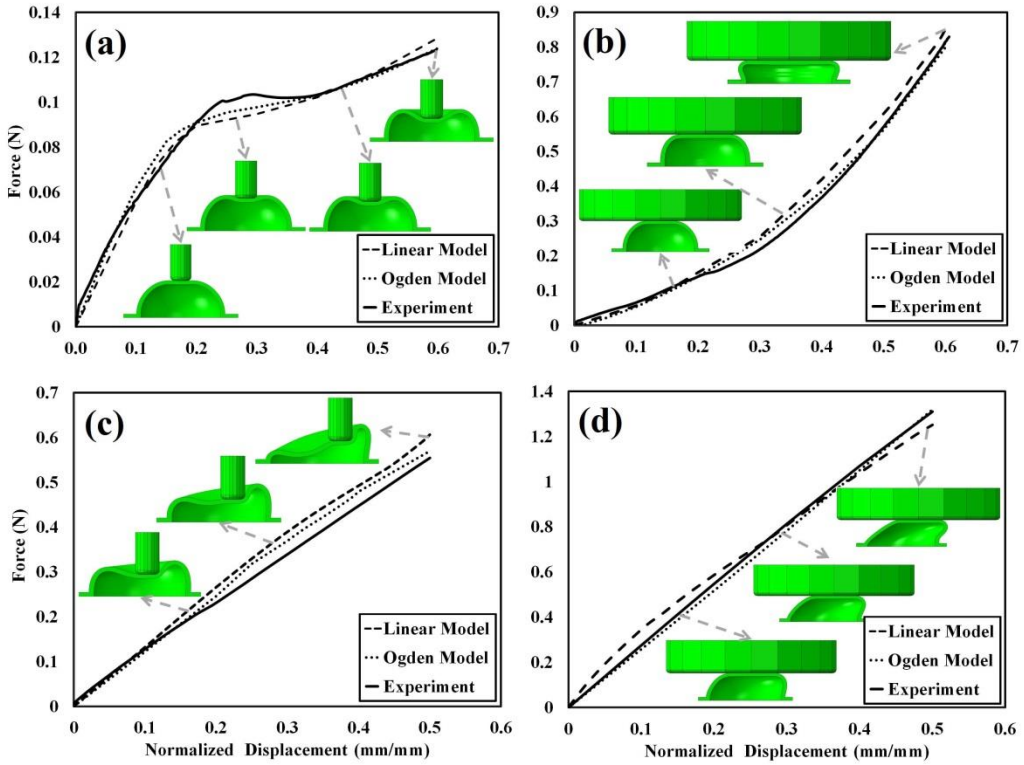

Figure 6. Comparison of the experimental data and simulation results. The horizontal axes are normalized by the radius of the spherical shell. (a) Normal load applied by the small cylinder. (b) Normal load applied by the flat plate. (c) Shear load applied by the small cylinder. (d) Shear load applied by the flat plate.

Predicting Behavior for Sensor Design

The validated models are used to design sensors with specific characteristics for a given application. In this case we have used the models to predict the response of sensors with different radii (4.5 mm, 7.0 mm, and 9.5 mm). Sensors of different radii are needed in different sections of a robot. For instance, sensors with increasing radii are used to covering a robot hand, arm, and chest. In general, the change in radii is a tradeoff between covering larger areas and spatial resolution.

RESULTS AND DISCUSSION

Sensor Response to Objects with Different Geometry

Experimental results have been used to verify the validity of the Ogden and linear elastic models for modeling the sensor. The simulation and experimental results of the loads applied by the small cylinder and flat disk are compared in Fig. 6(a) and (b) for normal loads and in Fig. 6(c) and (d) for shear loads. The horizontal axes are normalized displacements, which are the ratio of the displacement to the sensor radius, and the vertical axes are the forces applied by the indenters. Despite of the nonlinear behavior of the silicone rubber, the linear elastic model can simulate the mechanical behavior of this material satisfactorily. This shows that the geometric nonlinearity which associates with the change of modulus of elasticity due to geometry change dominates and, material non-linearity which comes from the nonlinearity of the constitutive law does not have significant effect on the results. The reason can be found from the fact that when the strain remains small, constitutive laws can be linearized and the material can be considered as linear elastic, and when deformations are small, geometrical nonlinearity is negligible [38]. In this case, the displacements are not small and the geometric nonlinearity appears in the results. However, the strains of the elements mostly are not large and the material almost responses like a linear elastic material. Consequently, in the simulations, we have used a linear elastic model to study the effects of geometric nonlinearity of the system.

Fig. 6(a) indicates that spherical shell elastic response to the normal loads has three regimes. The first regime starts from the moment of contact up to the moment that the base of the cylinder entirely touches the spherical shell. In this region the elastic response is almost linear and the transition from this stage to the next stage occurs at a deformation

close to 1.2 times of the thickness. The second regime is a transition between the first and third regime, in which the cap of the sphere is transmitted from a cap to a dimple (inverted cap). In this stage, the spherical shell shows maximum resistance against the deformation until the compression stress reaches a level that provides enough energy for changing the con- formation of the cap to a dimple. In the third regime, the sensor forms a dimple. This new conformation has less rigidity than the first one and shows almost linear response to the normal loads. The overall behavior of spherical shell under these forces is similar to that of point contact, which follows Equation 3 (Elastic modulus reduction). Fig. 6(b) shows that in the process of applying normal forces by a flat disk, unlike what we have discussed in the background, the top part of the sensor stays in contact with the flat plate and the configuration does not turn into the inverted cap. This is due to the large thickness to radius ratio (around 10%) and the low elastic modulus of the silicone rubber that cannot provide enough stresses for buckling of the cap. Therefore, the results do not show significant changes in the geometry of the sensor during loading process and the elastic response to such a large force still follows Equation 1 (Elastic modulus growth).

Fig. 6(c) shows that during the shear loading applied by a small cylinder, one side of the sensor undergoes tension and increases the probability of buckling and instable response, while the other side bends [Fig. 8(c)]. In spite of changes in the geometry of the hemisphere in this type of loading, the elastic response is almost linear.

Fig. 6(d) shows that applying shear loads with a flat plate on the hemispherical shell, also, results in an almost linear response. Due to pre-compression caused by the pushing flat plate, the probability of getting an instable response decreases.

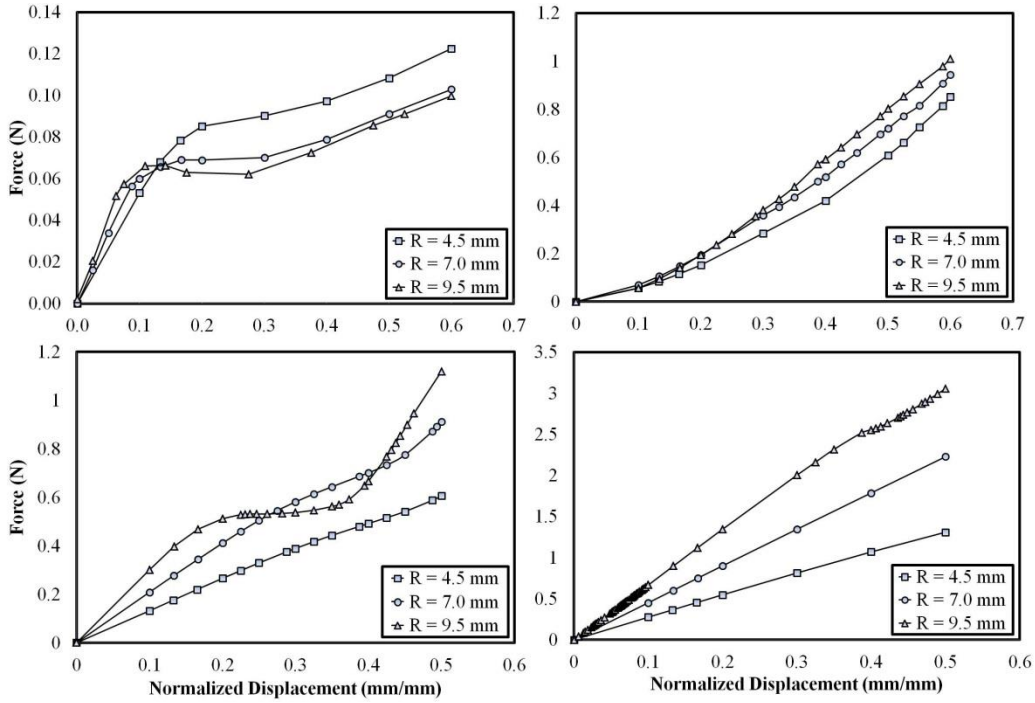

Figure 7. Simulation results for sensors with different radii. (a) Normal load applied by the small cylinder. (b) Normal load applied by the flat plate. (c) Shear load applied by the small cylinder. (d) Shear load applied by the flat plate.

Effect of the Sensor Radius

Fig. 7(a) shows the force-displacement curve for normal loads applied by the small cylinder on the sensors with different radii. The spherical shells with the greater radii show more relative rigidity in the first region of the loading process. It should be noted that higher rigidity results in less sensitivity of the sensor because greater force is needed to deform the sensor. The spherical shells with greater radii have greater ratio of the radius to thickness (slenderness ratio) and buckle, in the second regime. Hence the response is less stable due to sudden change in the shape and stiffness of the system. In the third region, all the spherical shells show almost linear response with the same rigidity. Considering all the factors we have discussed regarding the normal load applied by the small cylinder [Fig. 8(a)], the mechanical response of a spherical shell to this kind

of forces is nonlinear and the sensors with smaller radii show more sensitivity and stable behavior, and are able to detect higher force.

Fig. 7(b) indicates almost linear response of the spherical shell to the normal force exerted by the flat disk. This type of contact is stable even for the conditions with great ratio of the radius to thickness. Sensors with greater radii show less sensitivity and are able to detect higher forces [Fig. 8(b)].

The results of shear loads on the sensors applied by the small cylinder and flat disk are presented in Fig 7(c) and (d), respectively. The elastic response of the sensor applied by the small cylinder shows that in the early stage of loading, the sensor with greater radius shows less sensitivity. As the forces increase the sensor with the radius of 4.5 mm shows almost a linear and stable response because the configuration of the sensor doesn't change drastically. However, for the sensors with greater radii the elastic response becomes more nonlinear due to significant change in the shape of the sensors. In the loading process, one side of the sensor undergoes great tension and the other side bends dramatically. The part in tension of sensors with greater ratio of radius to thickness buckles and leads to instable response. These results indicate that the spherical shell with smaller radius shows overall linear and stable responses with smaller maximum loads. The shear loads applied by the flat disk shows almost linear response [Fig. 7(d)]. These results imply that the sensitivity of the sensor decreases for the sensor with greater radius. The elastic response of the sensor to this type of load is stable even for the sensor with high ratio of radius to thickness.

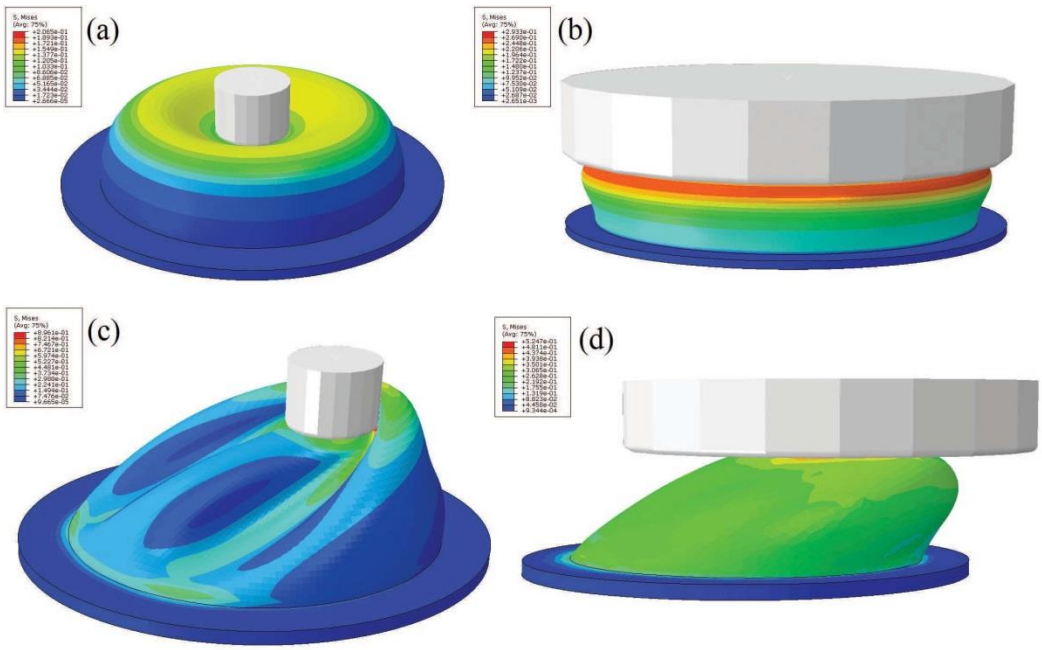

Figure 8. Contours of Mises stress in the spherical sensor with a radius of 9.5 mm (a) the normal load applied by the small cylinder (b) the normal force applied by a flat disk (c) the shear force applied by small cylinder (d) the shear force applied by flat disk.

CONCLUSION

In this project we studied, experimentally and numerically, a compliant tactile sensor made of silicon rubber with spherical shell geometry. This bioinspired sensor has crucial character- istics for robotics applications and has been tested in actual robots that perform sensitive manipulation. The characteristic studied in this work is the capability of estimating normal and shear contact forces independently of the object's geometry. The geometries used to test the sensor were a flat disk and a small diameter cylinder. These geometries represent small curvature surfaces and sharp edges that are typically found by a robot when performing manipulation. A model of the sensor was developed and compared with experimental results. The comparison shows that a linear elastic model of the spherical silicone rubber shell can simulate the mechanical response of the system reasonably well, because geometrical nonlinearity dominates the overall behavior. This

model was used to predict the effect of changing the sensor radius, which is needed to design sensors for different applications. These applications include smaller sensors for fingertips, and larger sensors for a robot's forearm. The results of the simulations indicate that an increase in radius of the sensor increases the relative stiffness of the system and results in less sensitivity [Figs. 6–8]. Since the sensors with greater radii (same thickness) have more slen- derness ratio, they are less stable and buckling occurs during the loading process. The force response caused by penetration of the small cylinder is found to be highly nonlinear because of the changes in the geometry [Figs. 6(a) and 8(a)] whereas the results for the flat disk are almost linear [Figs. 6(b) and 8(b)]. This implies that the sensor with smaller radius has more sensitivity and higher probability of showing linear behavior in contact with objects. The results of shear loads indicate that the elastic response to such forces is almost linear. The response of the sensor is appropriated for robotic applications such as sensitive robotics where force detection is more important than force fidelity and a monotonic response is enough in most practical cases. Finally, the model developed enables the design of compliant tactile sensors whose characteristics can be modified for a given application.

REFERENCES

[1] S. Begej, "Planar and finger-shaped optical tactile sensors for robotic applications," IEEE J. Robot. Autom., vol. 4, no. 5, pp. 472–484, Oct. 1988.

[2] B. Ali, M. A. Ayub, and H. Yussof, "Characteristics of a new optical tactile sensor for interactive robot fingers," Int. J. Soc. Robot., vol. 4, pp. 85–91, 2012.

[3] T. Someya, Y. Kato, T. Sekitani, S. Iba, Y. Noguchi, Y. Murase, et al., "Conformable, flexible, large-area networks of pressure and thermal sensors with organic transistor active matrixes," Proc. Nat. Acad. Sci. USA, vol. 102, no. 35, pp. 12321–12325, 2005.

[4] A. Wisitsoraat, V. Patthanasetakul, T. Lomas, and A. Tuantranont, "Low cost thin film based piezoresistive MEMS tactile sensor," Sens. Actuators A, Phys., vol. 139, nos. 1–2, pp. 17–22, 2007.

[5] H. Muhammad, C. Recchiuto, C. Oddo, L. Beccai, C. Anthony, M. Adams, et al., "A capacitive tactile sensor array for surface texture discrimination," Microelectron. Eng., vol. 88, pp. 1811–1813, Aug. 2011.

[6] D. Alvares, L. Wieczorek, B. Raguse, F. Ladouceur, and N. H. Lovell, "An evaluation study of nanoparticle films as biomimetic tactile sensors," Sens. Actuators A, Phys., vol. 186, pp. 148–153, Oct. 2012.

[7] C. F. Hu, W. S. Su, and W. Fang, "Development of patterned carbon nanotubes on a 3D polymer substrate for the flexible tac- tile sensor application," J. Micromech. Microeng., vol. 21, no. 11, pp. 115012-1–115012-12, 2011.

[8] O. Yilmazoglu, A. Popp, D. Pavlidis, J. J. Schneider, D. Garth, F. Schuttler, et al., "Vertically aligned multiwalled carbon nanotubes for pressure, tactile and vibration sensing," Nanotechnology, vol. 23, no. 8, pp. 85501–85508, 2012.

[9] H. Yokoi, A. H. Arieta, R. Katoh, W. Yu, I. Watanabe, and M. Maruishi, "Mutual adaptation in a prosthetics application," in Embodied Artificial Intelligence, vol. 3139. New York, NY, USA: Springer-Verlag, 2004, pp. 146–159, 2004.

[10] K. J. Rebello, "Applications of MEMS in surgery," Proc. IEEE, vol. 92, no. 1, pp. 43–55, Jan. 2004.

[11] H. K. Lee, J. Chung, S.-I. Chang, and E. Yoon, "Normal and shear force measurement using a flexible polymer tactile sensor with embedded mul- tiple capacitors," J. Microelectromech. Syst., vol. 17, no. 4, pp. 934–942, Aug. 2008.

[12] R. Dahiya, G. Metta, M. Valle, and G. Sandini, "Tactile sensing—From humans to humanoids," IEEE Trans. Robot., vol. 26, no. 1, pp. 1–20, Feb. 2010.

[13] E. Torres-Jara, "Sensitive manipulation," Ph.D. dissertation, Massa- chusetts Institute of Technology Comput. Sci. Artif. Intell. Lab., Cambridge, MA, USA, 2007.

[14] E. Torres-Jara and G. Gomez, "Fine sensitive manipulation," in Proc. Austral. Conf. Robot. Autom., Canberra, Australia, Dec. 2008, pp. 1–7.

[15] A. Jain, M. D. Killpack, A. Edsinger, and C. C. Kemp, "Reaching in clutter with whole-arm tactile sensing," Int. J. Robot. Res., vol. 32, no. 4, pp. 458–482, 2013.

[16] J. M. Romano, K. Hsiao, G. Niemeyer, S. Chitta, and K. J. Kuchenbecker, "Human-inspired robotic grasp control with tactile sensing," IEEE Trans. Robot., vol. 27, no. 6, pp. 1067–1079, Dec. 2011.

[17] E. Torres-Jara, I. Vasilescu, and R. Coral, "A soft touch: Compliant tactile sensors for sensitive manipulation," MIT-CSAIL, Cambridge, MA, USA, Tech. Rep. MIT-CSAIL-TR-2006-014, Mar. 2006.

[18] E. Torres-Jara, "Compliant tactile sensor that delivers a force vector," U.S. Patent 7 701 202, Apr. 20, 2010.

[19] E. Torres-Jara, "Compliant tactile sensor for generating signal related to an applied force," U.S. Patent, 8 101 904, Jan. 24, 2012.

[20] L. Natale and E. Torres-Jara, "A sensitive approach to grasping," in Proc. 6th Int. Workshop Epigenetic Robot., Paris, France, Sep. 2006, pp. 87–94.

[21] V. Chernyak, E. Claretti, S. Nestinger, and E. Torres-Jara, "Caminante: A platform for sensitive walking," in Proc. 16th Int. Conf. Climb. Walk. Robots Support Technol. Mobile Mach., Jul. 2013, pp. 351–358.

[22] N. Rahbar and W. Soboyejo, “Design of functionally graded dental multilayers,” Fatigue Fracture Eng. Mater. Struct., vol. 34, no. 11, pp. 887–897, 2011.

[23] T. Tan, N. Rahbar, S. Allameh, S. Kwofie, D. Dissmore, K. Ghavami, et al., “Mechanical properties of functionally graded hierarchical bam- boo structures,” Acta Biomater., vol. 7, no. 10, pp. 3796–3803, 2011.

[24] A. Agrawal, N. Rahbar, and P. Calvert, “Strong fiber reinforced hydrogel composites,” Acta Biomater., vol. 9, no. 2, pp. 5313–5318, 2013.

[25] R. S. Fearing and J. M. Hollerbach, “Basic solid mechanics for tactile sensing,” Int. J. Robot. Res., vol. 4, no. 3, pp. 40–54, 1985.

[26] G. Gerling and G. Thomas, “The effect of fingertip microstructures on tactile edge perception,” in Proc. 1st Joint Eurohapt. Conf., Symp. Hapt. Inter. Virtual Environ. Teleoperator Syst. World Hapt., Mar. 2005, pp. 63–72.

[27] J. Scheibert, S. Leurent, A. Prevost, and G. Debregeas, “The role of fingerprints in the coding of tactile information probed with a biomimetic sensor,” Science, vol. 323, no. 5920, pp. 1503–1506, 2009.

[28] R. S. Dahiya and M. Gori, “Probing with and into fingerprints,” J. Neurophysiol., vol. 104, no. 1, pp. 1–3, 2010.

[29] F. Hendriks, D. Brokken, C. Oomens, D. Bader, and F. Baaijens, “The relative contributions of different skin layers to the mechanical behavior of human skin in vivo using suction experiments,” Med. Eng. Phys., vol. 28, no. 3, pp. 259–266, 2006.

[30] N. F. A. Manan, M. H. M. Ramli, M. N. Azmi, A. Patar, C. Holt, M. Chizari, et al., “Determining hyperelastic parameters of human skin using 2D finite element modeling and simulation,” in Proc. IEEE Symp. Humanit., Jun. 2012, pp. 805–809.

[31] J. Nishiyama, C. D. Tsai, A. Shibata, M. Higashimori, and M. Kaneko, “An experimental study of biologically inspired artificial skin sensor under static loading and dynamic stimuli,” in Proc. IEEE Int. Conf. Robot. Autom., Shanghai, China, May 2011, pp. 1778–1783.

[32] D. Yamada, T. Maeno, and Y. Yamada, “Artificial finger skin having ridges and distributed tactile sensors used for grasp force control,” in Proc. IEEE/RSJ Int. Conf. Intell. Robot. Syst., vol. 2. 2001, pp. 686–691.

[33] G. Vásárhelyi, M. Ádám, É. Vázsonyi, I. Bársony, and C. Dücso″ , “Effects of the elastic cover on tactile sensor arrays,” Sens. Actuators A, Phys., vol. 132, no. 1, pp. 245–251, 2006.

[34] R. S. Johansson and J. R. Flanagan, “Coding and use of tactile signals from the fingertips in object manipulation tasks,” Nature Rev. Neurosci., vol. 10, no. 5, pp. 345- 359, 2009.

[35] T. Maeno, K. Kobayashi, and N. Yamazaki, “Relationship between the structure of human finger tissue and the location of tactile receptors,” JSME Int. J. Ser. C, vol. 41, no. 1, pp. 94–100, 1998.

[36] A. Lazarus, H. C. B. Florijn, and P. M. Reis, “Geometry-induced rigidity in nonspherical pressurized elastic shells,” Phys. Rev. Lett., vol. 109, no. 14, pp. 144301-1–144301-5, 2012.

[37] H. J. Hertz, “Ueber die berührung fester elastischer körper,” J. Für Reine Angew. Math., vol. 1882, no. 92, pp. 156–171, Jan. 1882.

[38] B. Audoly and Y. Pomeau, Elasticity and Geometry: From Hair Curls to the Non-Linear Response of Shells. Oxford, U.K.: Oxford Univ. Press, Aug. 2010.

[39] A. V. Pogorelov, Bendings of Surfaces and Stability of Shells. Providence, RI, USA: AMS, 1988.

[40] L. Pauchard and S. Rica, “Contact and compression of elastic spherical shells: The physics of a ping-pong ball,” Phil. Mag. B, vol. 78, no. 2, pp. 225–233, 1998.

[41] D. Hibbitt, B. Karlsson, and P. Sorensen, ABAQUS/Standard User’s Manual. Providence, RI, USA: Dassault Systèmes Simulia Corp, 2010.

[42] G. A. Holzapfel, Nonlinear Solid Mechanics: A Continuum Approach for Engineering. Chichester, U.K.: Wiley, 2000.

[43] P. A. L. S. Martins, R. M. Natal Jorge, and A. J. M. Ferreira, “A comparative study of several material models for prediction of hyperelastic properties: Application to silicone-rubber and soft tissues,” Strain, vol. 42, no. 3, pp. 135–147, 2006.

[44] L. Meunier, G. Chagnon, D. Favier, L. Orgéas, and P. Vacher, “Mechani- cal experimental characterisation and numerical modelling of an unfilled silicone rubber,” Polymer Test., vol. 27, no. 6, pp. 765–777, 2008.